2017

Protection Challenges of Distributed Energy Resources Integration In Power Systems

Pooria Mohammadi
Louisiana State University and Agricultural and Mechanical College

PROTECTION CHALLENGES OF DISTRIBUTED ENERGY RESOURCES INTEGRATION IN POWER SYSTEMS

A Dissertation

Submitted to the Graduate Faculty of the
Louisiana State University and
Agricultural and Mechanical College
in partial fulfillment of the
requirements for the degree of
Doctor of Philosophy

in

The School of Electrical Engineering and Computer Science

by
Pooria Mohammadi
B.S., Iran University of science and Technology, 2005
M.S., University of Texas at Tyler, 2013
August 2017

تقدیم به

پدر و مادر عزیزم

که بیان احساسم به آنها

در کلام نمی گنجد.

Dedicated to my parents.

Acknowledgements

First I would like to acknowledge my advisor Dr. Shahab Mehraeen for his support, excellent guidance, and ultimate mentorship over the years. Without his insightful and innovative ideas, this thesis could not have been accomplished.

Special thanks goes to my family of whom I received invaluable support and constant dedication. I want to thank to all my friends and also colleagues at Louisiana State University *Smart Grid and Renewable Power Laboratory: Control and Protection* for their helps and supports.

I would like to thank LSU faculty members Leszek S Czarnecki, Hsiao-Chun Wu, Mehdi Zeidouni, Mehdi Farasat, and Amin Kargarian Marvasti for being members of my general and oral examination committees and providing me with their thoughtful comments and suggestions.

I also express my appreciation to the Entergy Services and specifically to Tom Field and Mark Bruckner from Transmission Design Basis group for their support and encouragement throughout this work.

I also thank the administrative team at the Division of Electrical and Computer Engineering, Louisiana State University. I wish to express my appreciation to Beth R. Cochran for her constant support.

TABLE OF CONTENTS

Abstract

It is a century that electrical power system are the main source of energy for the societies and industries. Most parts of these infrastructures are built long time ago. There are plenty of high rating high voltage equipment which are designed and manufactured in mid-20th and are currently operating in United States' power network. These assets are capable to do what they are doing now. However, the issue rises with the recent trend, i.e. DERs integration, causing fundamental changes in electrical power systems and violating traditional network design basis in various ways.

Recently, there have been a steep rise in demands for Distributed Energy Resources (DERs) integration. There are various incentives for demand in such integrations and employment of distributed and renewable energy resources. However, it violates the most fundamental assumption in power system traditional designs. That is the power flows from the generation (upstream) toward the load locations (downstream). Currently operating power systems are designed based on this assumption and consequently their equipment ratings, operational details, protection schemes, and protections settings. Violating these designs and operational settings leads toward reducing the power reliability and increasing outages, which are opposite of the DERs integration goals.

The DERs integration and its consequences happen in both transmission and distribution levels. Both of these networks effects of DERs integration are discussed in this dissertation. The transmission level issues are explained in brief and more analytical approach while the transmission network challenges are provided in details using both field data and simulation results. It is worth mentioning that DERs integration is aligned with the goal to lead toward a smart grid. This can be considered the most fundamental network reconfiguration that has ever experienced and requires various preparations. Both long term and short term solutions are

proposed for the explained challenges and corresponding results are provided to illustrate the effectiveness of the proposed solutions. The author believes that developing and considering short term solutions can make the transition period toward reaching the smart grid possible. Meanwhile, long term approaches should also be planned for the final smart grid development and operation details.

Chapter 1
Introduction

1.1. Background and Motivation

The integration of Distributed Energy Resources (DERs) into the power grids has brought many new challenges to the currently operating power system and networks. There are various incentives for this integration convincing governments to promote it by various means as well as attracting the customers. The DERs integration, where mostly renewable energy resources are used as the base energy sources for them, can bring benefits such as reducing fossil fuels consumption and dependability, reducing Carbone dioxide, increasing system reliability, increasing profitability and customer owned generation, decreasing generation unit's capital investment, islanding operation, etc. It is obvious that the electric network safe operation and power reliability is the most important aspect which shouldn't have an adverse effect by this integration. However, the DERs integration makes significant change in the network fundamentals in a way that can be considered as a reconfiguration aligned toward establishing a smart grid.

Currently operating power systems are designed and operating based on a fundamental assumption which is unidirectional power flow. Integrating DERs and allowing loads (customers) to generate power and possibly even export at some period of times causes important changes in the network operation. When all DERs power generation are less than their local assumption, i.e. no power is being exported, the network operating point is significantly different than what it is designed for. This can critically affect the protection schemes, protective devices, and equipment ratings. Various DER generating units can easily have different fault current contribution comparing to what the system is designed for. On the other hand, the unidirectional power flow

assumption is violated if the DERs export power and this is the most extreme case. Figure 1.1 depicts a typical radial power system where various types of Distributed Generation (DG) units are integrated into it. The original design of this network is to flow the power from the utility grid point of connection toward the loads located in downstream. However, this fundamental and basic rule is violated by placing the DGs across the network, as explained earlier. The matter in such radial network is simpler to discuss and analyze while a similar situation exists in networks with mesh structure, e.g. downtown networks, which are explained more in details in this dissertation. In general, the issue of DERs integration challenges and possible solutions for it can be observed from two main perspectives based on the network characteristics:

1. Transmission level
2. Distribution level
    - Radial distribution networks
    - Mesh distribution networks.

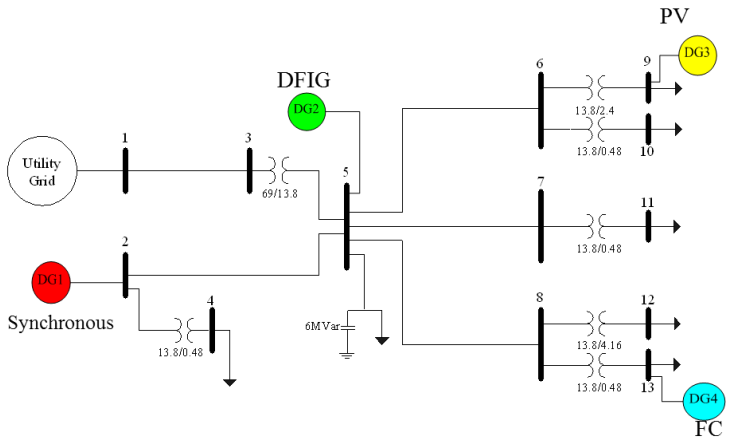

Figure 1.1: A radial power network with integrated DERs

Transmission and distribution level of power system have same fundamentals but very different details in design and operation. This is why the DERs integration analyses in this research is performed in both network levels but provided in different chapters. Figure 1.2 and 1.3 illustrate the US transmission level power systems and integrated DERs, respectively. On the other hand,

distribution networks can be in radial and mesh structures. The author has investigated and considered the radial distribution networks impacts from DGs integration during his master degree. Hence, radial distribution network analyses and results here are limited to the field experiences and valuable outcomes. But distribution networks in mesh configuration are paid extra attention in this dissertation. A good example for this networks is low-voltage secondary networks which are also called downtown networks. Because of the high important of the power reliability and quality in such networks and also the customer importance in such regions, the DERs integration is a critical issue to be analyzed there. Figure 1.4 depicts a typical downtown network where DGs can be installed at customer locations.

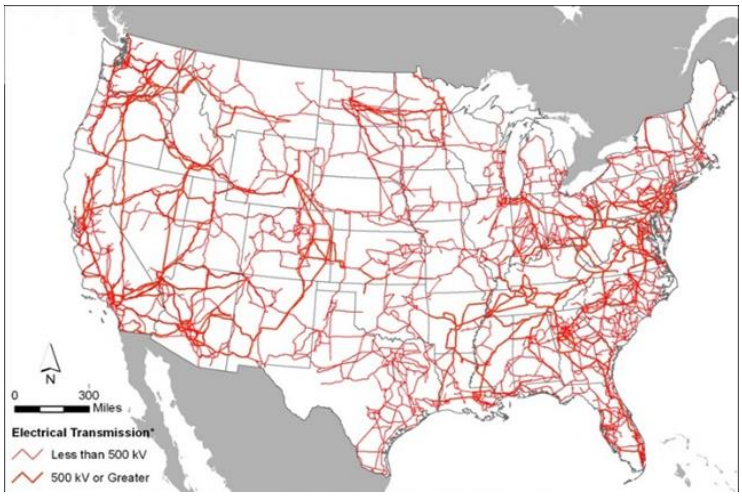

Figure 1.2: US power system transmission lines

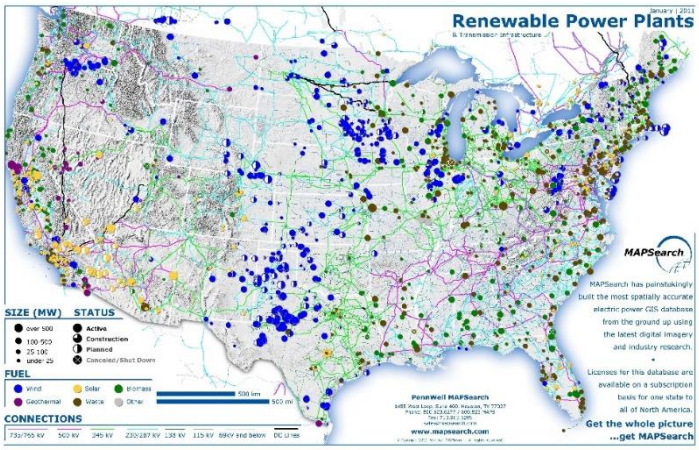

Figure 1.3: US power system SERs

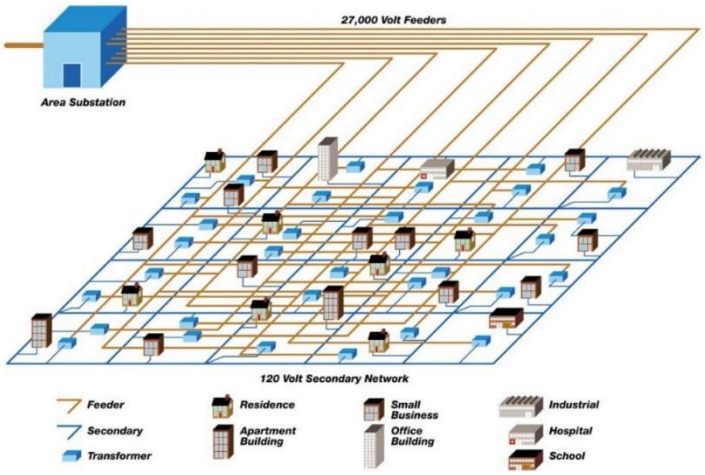

Figure 1.4: A typical downtown network

The power systems reliability and safe operation is of paramount importance. But there are other consequences in DERs integration which should be considered such as power quality, power market, scheduling, and etc. Considering power capacity, DER units can be categorized in two group as 1. Bulk and 2. Small. These categories and the DERs' power capacity is relative to the network in which they are installed on, i.e. DERs penetration. Usually bulk DERs are installed as utility owned generation or by businesses which can afford the investment as well as consume the generated power. On the other hand, small DERs are most likely installed by end customer users such as residential loads in a more distributed manner. The ability to control, regulate, and forced commitment for the bulk DERs are higher than small distributed DGs. However, this ability does not provide any definite assurance for the units' commitment to stay connected and provide power for the network. This is because of the technical details of DGs power connection and DERs usual source of power. Most DG units produce electricity from a sustainable natural resource such as sun, wind, tidal waves, and etc. There is always an uncertainty factor in such units' power production which makes their commitment quite complicated and unreliable. The intermittency of DERs power output has effects in various time scales from short (under second) to long (daily and

more than monthly). For instance, Photovoltaic (PV) cell performance is dependent on the intermittent solar radiation causing power variations and voltage fluctuations. In general, this raises concerns about networks voltage stability and power quality which are addressed in this dissertation. However this power output unpredictability causes uncertainties in long term power generation scheduled commitments. It should be mentioned that the explained issue is also applicable to the DGs which their source of energy is not an intermittent natural resource but rather is sources such as fuel cell, diesel, etc. Fuel availability, customer willingness, market price, and connection details can still affect such units' commitment in an unpredictable way. Basically, DERs unit power production and network commitment depend on three main factors:

1. Energy source availability,
2. Owner will,
3. Operation and connection technical details.

Majority of DG units require an electric power conversion unit at their connection point to the network. This is either because of stabilizing the output ripples due to the energy source changes (wind, solar) or forming the electricity to the operating frequency and form. This is mostly performed by power electronic device where their control algorithm is complicated topic beyond of this context topic. Power electronic converters and inverters are widely used for power conversion and control proposes in most of DGs. A good example for this are PV units. Most PVs are connecting to the grid by an inverter unit converting dc to ac and some are equipped with battery storage systems for better performance and reliability. As integration of PV units are becoming more prevalent in distribution networks, they are more likely to be an important active element of such networks and will have significant impacts on the power reliability and quality. With recent industry progresses, both small residential and larger units' inverters are enabled with

control and strategic functions to improve their functionality. Also, newer inverter units take advantage of communication systems. That is, PV units can comply with the utility regulations either autonomously, via fixed and variable set points, or controlled through communication infrastructures. One of the most well-known equipment with these capabilities are smart inverters. Autonomous control and standalone functionality are sued in the last decade. Where these control methods are useful for islanding scenarios they are not neither completely safe, in terms of operation and cross effects, nor optimized. By making communication infrastructures more available such control strategies are tend to be more optimized and unified in following their goals. These objectives can voltage control, reactive power compensation, active power control, peak shaving, time shifting, and even dynamic variables control such as frequency. There are multiple schemes to collect the data and information from DER units and transfer them to a central operation unit to send out commands on how to react in a specific time or to a specific phenomenon. This way the DERs capabilities and smart inverters functionalities are closer to be fully deployed. Such schemes which can be considered a collection of DERs capability, smart inverter functionality, communication infrastructures, fast system solvers and analyzers, and optimization algorithms can be found in applications such as Energy Management Systems (EMS) and Distribution Management Systems (DMS). However, there are plenty of challenges in fully accomplished a smooth and optimized operation as described. Figure 1.5 depicts a power system transmission level where Phasor Measurement Units (PMUs) are used to gather data for Wide Area Measurement, Protection, and Control (WAMPAC) scheme.

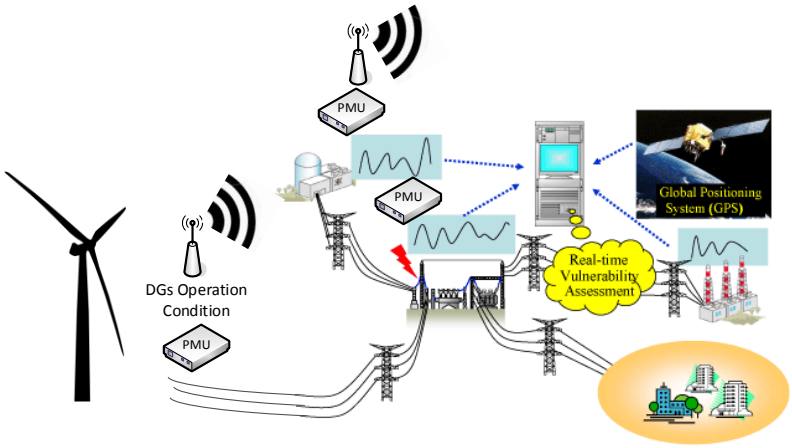

Figure 1.5: PMU equipped transmission power system for wide area protection

1.2. Outline of the Dissertation

The remainder of this dissertation is organized as follows. In Chapter 2, Phasor Measurement Units (PMU) placement in transmission power system is discussed for system fault observability and fault location. Measurements yielded from PMUs are GPS time stamped which makes them capable for phasor estimation as well as frequency detection. This features along with high resolution samples make PMU a key element to assist to solve the rising challenges of DERs integration and system changes. Power system fault observability is achieved along with fault detection when an optimized PMU placement algorithm is proposed. Extensive results and discussions are provided in Chapter 2.

Chapter 3 presents results and studies for the DERs integration in overhead radial distribution networks with extra attention to power quality concerns. DERs integration can cause consequences regarding the voltage flicker, harmonics, etc. These are discussed and various IEEE and ANSI standards are mentioned to compare the modelled network operation details with allowed standard limits. It should be mentioned that PVs are widely used in this research as an extreme case for power intermittency and due to high demand from their applications. PV units are considered a good instance for DGs integration due to their smart inverter possible functions

effects and complexity and also feasibility for constructing a smart grid with required communication infrastructure.

Chapter 4 discussed protection challenges for DERs and specifically PVs integration in low-voltage secondary networks (downtown). Downtowns are one of the networks where there are high demand for DERs integration and they are also vulnerable for such integration consequences. New Orleans downtown network is modelled in this chapter and extensive analyses are performed illustrating the protection scheme and elements malfunctioning leading toward network collapse. It is shown that for a safe and reliable network operation the DERs penetration should be limited to less than 16%. Another viable and economical solution is proposed in this chapter to resolve the network protection issues when higher DERs penetration is allowed. Using the proposed method more than 50% DER penetration can be integrated in the network. Penetrations higher than this are discussed in Chapter 3 where other network specifications and ratings should be considered.

Chapter 5 summarizes the results and discussions in all chapter with concluding remarks. Some discovered topis are also proposed here to be considered as possible future works aligned with this line of research.

Chapter 2
Power System PMU Placement for Fault Observability and Location

1.3. Introduction

The roles of synchronized Phasor Measurement Units (PMU) in power systems monitoring, control, and protection are prominent and constantly developing [1]–[4]. The traditional supervisory control and data acquisition (SCADA) systems collect data from the remote terminal units (RTUs) that are mostly available in substations. With the global positioning system (GPS) and by employing PMUs, accurate and time-synchronized measurement signals are now available. This enables the operator to take advantage of wide area monitoring, protection and control (WAMPAC) [5]. These applications include accurate fault location [6], normal and fault observabilities [2], [7], and post-contingency analysis [8] as well as static analysis, identifying system dynamics, transient stability prediction and control, voltage and frequency stability [8], etc. PMU and WAMPAC should make it possible to safely operate smart grids employing the maximum available capacity of renewable and distributed energy resources.

Pioneering studies on PMU introduction, development and utilization are performed by Phadke et al. [1], [9]. In [1], the possibility of employing PMUs on all system buses is explored. However, PMUs' relatively high costs and their required infrastructure such as communication in substations prevent the use of this solution. Therefore, many techniques and algorithms have been proposed in recent years to find Optimal PMU Placement (OPP) in power systems targeting system's normal observability. This is done using algebraic and topological methods. System

normal observability is guaranteed using algebraic methods if the rank of the measurement matrix is complete, i.e., it is equal to the number of system state variables. In topological methods, graph theory is employed and normal observability is ensured if it is possible to have an observable spanning tree [5]. These two approaches for OPP correspond to numerical observability and topological observability, respectively [2], [10]. A power system is normally observable when all of its bus voltage phasors are known using available measurements under normal operation [7]. The pioneering work in this topic is initially performed by [2] where an optimal set of PMUs are achieved by a dual search algorithm using both modified bisecting search and simulated-annealing-based method. Integer Linear Programming (ILP) is introduced in [3] considering systems with and without zero injection buses (buses with no source or load). It is shown in [3] that ILP is non-linear for cases with zero injection while it is linear in cases without zero injection. ILP is later generalized in [11] addressing redundancy, partial observability and pre-existing measurements. However, this method may result in local minima [12]. Limited PMU channels and their failure is discussed in [5] using Binary Search. Approaches such as exhaustive search, Genetic Algorithm, Tabu search, Greedy Algorithm, etc., are also discussed in the literature [13]. In addition, various cases of measurements such as direct PMU, conventional flow meters, zero injection buses and pseudo-measurements are introduced in multiple literatures [13].

While many approaches are proposed to solve OPP problem for power system normal observability (under normal operating condition), there are a very limited number of studies that target OPP for fault observability. A power system is fault observable if voltage and current phasors at both ends of all lines will be determinable during a fault scenario occurring at any point of the system. It should be mentioned that normal observability does not guarantee fault

observability [7]. Thus, a normal observable power system may not be fully observable during fault condition since fault alters the system structure.

Optimal PMU placement for fault observability is introduced by [14] and [15]. Authors in [14] employ the popular one-bus-spaced strategy to find the OPP by Genetic Algorithm using only PMU voltage measurements. The topic is expanded by [15] by considering zero injection buses (that reduce the system size) using both PMU voltage and current measurements followed by ILP methodology. In [7] weight vectors reflecting cost variables are considered for both PMU and conventional flow measurements resulting in non-linear formulation in fault observability. Optimal PMU placement for fault observability along with a fault location algorithm is utilized in [14] and [16] when one-bus-spaced strategy is employed for simplicity.

Though the available approaches take advantage of various algorithms to impose observability constraints, the important issue of measurement sensitivity (quality) and its impact on OPP set and fault location is considered in very few literatures. Authors of [17] utilize a minimization algorithm to reduce the number of sensors followed by considering the measurement precision in the fault location problem [18] given the sensor locations; however, the precision has not been used in the measurement optimal placement. The effect of the measurement precision in PMU placement is of paramount importance and adds additional constraints to the available methods while this has not been given enough attention in OPP solution methods. In addition, the majority of past literature contemplates that the one-bus-spaced location strategy in PMU placement is a necessary condition to attain fault location [16]; however, this chapter shows that the set of critical measurement points to attain a desired accuracy in fault location, which is typically smaller than that of the one-bus-spaced method, is more appropriate.

This research considers PMU direct measurements with adequate channel availability for voltage and current measurements. A slightly different definition of fault observable system than [7], [14]–[15] is adopted here. If location and impedance of all faults of interest in a power system can be determined with predefined accuracy through a set of voltage and current measurements, the system is considered fault observable. A unique function mapping between measurements and faults is obtained and discussed in a systematic manner for the first time to the authors' best knowledge. The objectives of this research include:

1. Introduce sensitivity analysis in OPP problem for power systems fault observability. The quality of measurements is assessed at PMU locations using the proposed sensitivity indices. Thus, one can judge if a network bus is a good measurement location through which faults can be located. Using the proposed sensitivity analysis, measurement precision or inaccuracy instigated by the current transformers (CTs), potential transformers (PTs), and PMUs can be incorporated in the OPP problem. Measurement quality is also vital for other system analyses such as voltage stability, contingency studies, etc., which are mostly fault related.
2. Formulate minimal PMU placement and find pertinent optimal PMU sets for fault observability and fault location. That is, the proposed algorithm finds the optimal PMU sets such that the faults are located uniquely, i.e. with no multi estimation, with desired accuracy using minimum number of PMUs. Multi estimation is a condition where different faults result in similar measurements in a selected PMU set.
3. Develop a fault locator by utilizing obtained optimal PMU set via artificial neural networks (ANNs). The function approximation property of the ANNs is employed to map between the faults and the measurements of the optimal PMU set.

Contingency as well as missing and additional measurements discussions are omitted due to space limitation and cross-topic confusions. The remainder of this chapter is organized in the following order: Section II presents the proposed sensitivity analysis and introduces the sensitivity indices. In Section III, the sensitivity and multi estimation criteria are presented followed by the proposed algorithm for solving OPP in Section IV. Section V includes simulation results of the proposed method on the IEEE 7-bus, IEEE 14-bus, and IEEE 30-bus test systems followed by artificial neural network fault locator results to test the proposed approach for fault location application. Finally, concluding remarks are provided in Section VI.

1.4. Sensitivity Analysis

The approach presented in this chapter is built upon the classical fault analysis and is considered for three-phase symmetrical systems. However, the approach can be generalized to single-phase and unsymmetrical networks as well [6], [19]. The fault in power systems changes the structure of the system where its location and impedances are unknown. Subsequently, previously known system states, impedance matrix (Z_0), and admittance matrix (Y_0) should be altered to accommodate the fault. A fault is referred to value $F = \left(l_f, D,\ R_f\right)$ where $1 \leq l_f \leq L$ is the line number with L being the total number of lines in the power system, $0 \leq D \leq 1$ is the normalized distance of the fault with respect to one of the line end buses where $D = \frac{length(lp)}{length(lk)}$, and $0 \leq R_f \leq R_{max}$ is the fault line-to-ground resistance in the single-phase equivalent circuit with R_{max} being the maximum fault impedance of interest. The line exposed to the fault is located between network buses l and k that are unknown due to the random nature of the fault. Subsequently, previously known system states, impedance matrix Z_0, and admittance matrix Y_0 should be altered to accommodate the fault analysis (see Figure 2.1) [19].

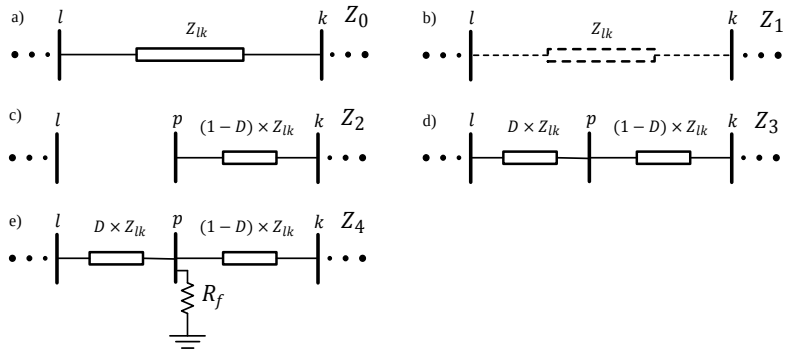

Figure 2.1: Steps for Z_{bus} modification: Z_0 through Z_3 are the steps of change in Z_{bus}

This study considers faults on power system lines (note that faults on grid buses is a special case). That is, an extra bus $p = N + 1$ is designated at the point of fault where N is the network total number of buses. Figure 1 shows the procedure of adding a fault to the system. The unfaulty power system with known impedance matrix Z_0, voltages, and currents are depicted in Figure 2.1a. Also, Figure 2.1d depicts the faulty system with the fault (on one of the network lines) and impedance matrix Z_3 (fault not included). The line exposed to the fault is located between system buses l and k that are unknown due to the random nature of the fault with unknown fault distance D and fault resistance R_f.

Definitions: The following terms are frequently used in this chapter.

- *Normal value*: The value of a bus voltage or a line current in an unfaulty power system is called normal value.
- *Fault*: A fault is referred to by value $F = (l_f, D,\ R_f)$ where $l_f \in \boldsymbol{L_f} = \{1,2,\dots,L\}$ is the line number where fault occurs with L being the total number of lines in the power system, $D \in \mathbf{D} = [0,1]$ is the normalized distance of the fault with respect to one of the line end buses ($D = \frac{length(lp)}{length(lk)}$ from Fig. 1), and $R_f \in \mathbf{R_f} = [0, R_{max}]$ is the fault line-to-ground resistance in the single-phase equivalent circuit with R_{max} being the maximum fault resistance of interest. If

R_{max} is selected very small (short circuit), the loads can be ignored in the proposed method. Otherwise, the load information may be needed to locate the fault accurately.

- *Observant bus*: Bus $h \in \{1,2,\dots,N\}$, with N being the total number of power system buses, where a measurement device capable of measuring the bus voltage and currents (of the lines connected to that bus) is installed, is an observant bus.
- *Observant set*: A set $H \subseteq \{1,2,\dots,N\}$ of observant buses is called an observant set.
- *Adjacent bus*: Bus u is called an adjacent bus to observant bus h if $u \in U_h$ with U_h is the set of all connected buses to observant bus h. Also, U_h is called adjacent set to observant bus h and has h_c many members; i.e., there are h_c many connected buses (lines) to observant bus h.
- *Multi estimation*: Multi estimation is a condition where different faults cause similar measured values in an observant set.

Four steps are required to modify Z_0 and obtain Z_4 (dashed elements in Fig. 1.b imply faulty line removal from Z_{bus}):

Z_1: Remove the transmission line between buses l and k by adding the line's negative impedance $(-Z_{lk})$ between buses;

Z_2: Add $(1-D) \times Z_{lk}$ between bus k and new bus (p);

Z_3: Add $D \times Z_{lk}$ between bus l and existing bus p;

Z_4: Add R_f between bus p and ground reference node;

Each of these steps results in a new system with impedance matrix subscripted by the step number as shown in Figure 2.1 [16]. By using the standard fault analysis, the voltage changes at observant bus h, (when fault F occurs at bus p) can be described as

$$\Delta V_{h,F} = \frac{Z_3(h,p)}{Z_3(p,p)+R_f} \times V_{pref} \qquad (1)$$

where $Z_3(h,p)$ is the (h,p) entree of Z3, $Z_3(p,p)$ is the system Thevenin impedance seen from imaginary bus p , and V_{pref} is the prefault voltage at the point of fault in the system. With the assumption of linear voltage drop along the transmission lines between buses and by ignoring line capacitances to avoid complexity, V_{pref} can be calculated as:

$$V_{pref} = V_l + (1 - D) \times (V_l - V_k). \qquad (2)$$

For more accurate calculation in long transmission lines, hyperbolic voltage drop can be considered [16]. From the previous discussion, voltage and current rates of change in all buses of the system can be calculated by using original impedance matrix Z0 along with D and R_f, as will be explained next.

1.4.1. Voltage Sensitivity Indices

Voltage change in observant bus h due to fault $F = (l_f, D,\ R_f)$ is presented in (1). Using the chain rule on ΔV_h, voltage sensitivity indices are defined as derivatives of D and R_f with respect to ΔV_h as

$$S_{h,F}^{DV} = \left(\frac{\partial \Delta V_h}{\partial D}\right)^{-1} = \frac{\partial D}{\partial \Delta V_h}\ , S_{h,F}^{R_f V} = \left(\frac{\partial \Delta V_h}{\partial R_f}\right)^{-1} = \frac{\partial R_f}{\partial \Delta V_h}\,. \qquad (3)$$

One can use derivatives of $\Delta V_{h,F}$ with respect to D and R_f instead, and use the inverse function to achieve voltage sensitivity indices (3). That is, $S_{h,F}^{DV} = \left(\frac{\partial \Delta V_{h,F}}{\partial D}\right)^{-1}$.. Differentiation of V_{pref} with respect to D and R_f can be performed by considering (2). In the following, the expanded $Z_3(h,p)$ and $Z_3(p,p)$ are the result of the step-by-step parametric impedance matrix manipulations.

$$Z_3(h,p) = Z_2(h,p) - \frac{\big(Z_2(h,p) - Z_2(h,l)\big) \times (Z_2(p,p) - Z_2(l,p)\ )}{Z_2(p,p) + Z_2(l,l) - 2 \times Z_2(p,l) + D \times Z_{lk}}$$

$$Z_3(h,p) = Z_2(p,p) - \frac{\big(Z_2(p,p) - Z_2(p,l)\big) \times (Z_2(p,p) - Z_2(l,p)\ )}{Z_2(p,p) + Z_2(l,l) - 2 \times Z_2(p,l) + D \times Z_{lk}}$$

From transition in matrix impedances Z_1 to Z_3, one can conclude that for any fault $Z_2(p,p)$ is the only D-dependent variable in $Z_3(h,p)$ and $Z_3(p,p)$ as

$$Z_2(p,p) = Z_1(k,k) + (1-D) \times Z_{lk}.$$

Thus, considering $Z_2(p,p)$ derivatives of $Z_3(h,p)$ and $Z_3(p,p)$ with respect to D are

$$\frac{\partial Z_3(h,p)}{\partial D} = \frac{\left(Z_2(h,p) - Z_2(h,l)\right) \times Z_{lk}}{Z_1(k,k) + Z_2(l,l) - 2 \times Z_2(p,l) + Z_{lk}}$$

$$\frac{\partial Z_3(p,p)}{\partial D} = \frac{\left(Z_1(k,k)+(1-2D)Z_{lk}- Z_2(l,l)\right)\times Z_{lk}}{Z_1(k,k)+Z_2(l,l)-2\times Z_2(p,l)+Z_{lk}}.$$

It should be mentioned that these derivatives with respect to R_f are zero, but R_f should be considered in imposing chain rule on (1). Sensitivity index $S_{h,F}^{R_f V}$ can be found in a similar manner. The derivation of indices (3) are given in the appendix.

1.4.2. Current Sensitivity Indices

In a similar manner to voltage sensitivity indices, current sensitivity indices are defined for any fault F in the system as:

$$S_{hu,F}^{DI} = \left(\frac{\partial \Delta I_{hu}}{\partial D}\right)^{-1} = \frac{\partial D}{\partial \Delta I_{hu}}, S_{hu,F}^{R_f I} = \left(\frac{\partial \Delta I_{hu}}{\partial R_f}\right)^{-1} = \frac{\partial R_f}{\partial \Delta I_{hu}} \qquad (4)$$

where h is the observant bus and u is the adjacent bus connected to h by transmission line hu. The maximum number of current sensitivity indices for each bus h is equal to the number of lines connected to that bus. Figure 2.2 illustrates an example of a line current in the state of fault.

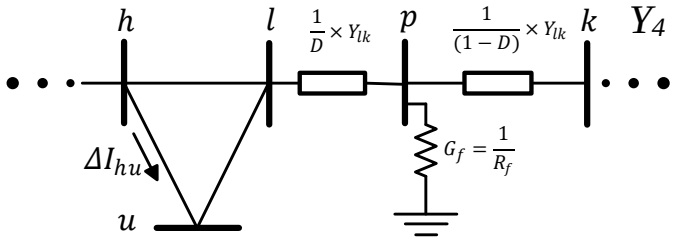

Figure 2.2: Observant and adjacent buses in faulty system

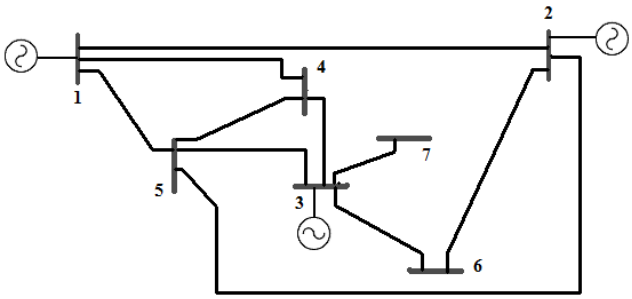

Figure 2.3: IEEE 7-bus system

Since ΔV_h is available for any h within the network, according to the standard power system fault analysis, line current changes can be expressed as

$$\Delta I_{hu} = \frac{\Delta V_h - \Delta V_u}{Z_{hu}} = Y_{hu} \times (\Delta V_h - \Delta V_u) = Y_2(h,u) \times (\Delta V_u - \Delta V_h) \qquad (5)$$

where Z_{hu} is the line impedance and $Y_2(h,u)$ is the admittance matrix (h,u) entree which corresponds to Z_4 according to Figure 2.1. The faulted network admittance matrix can be obtained by matrix manipulations similar to the procedure explained for impedance matrix transition. This process results in a function for Y_2 elements, many of which are not a function of D or R_f. Five elements that are D-dependent and one element that is R_f-dependent are obtained, for which $\frac{\partial Y_2}{\partial D}$ and $\frac{\partial Y_2}{\partial R_f}$ are calculated as

$$\frac{\partial Y_2(l,l)}{\partial D} = -\frac{\partial Y_2(l,p)}{\partial D} = \frac{-Y_{lk}}{D^2}$$

$$\frac{\partial Y_2(k,k)}{\partial D} = -\frac{\partial Y_2(k,p)}{\partial D} = \frac{Y_{lk}}{(1-D)^2}$$

$$\frac{\partial Y_2(p,p)}{\partial D} = \left(\frac{1}{(1-D)^2} - \frac{1}{D^2}\right) \times Y_{lk}$$

$$\frac{\partial Y_2(p,p)}{\partial R_f} = \frac{-1}{{R_f}^2}.$$

Using chain rule on (5), current sensitivity indices in (4) are

$$S_{hu,F}^{DI} = \left(\frac{\partial Y_2(h,u)}{\partial D}(\Delta V_h - \Delta V_u) + \left(\frac{\partial \Delta V_u}{\partial D} - \frac{\partial \Delta V_h}{\partial D}\right) Y_{hu}\right)^{-1}$$

$$S_{hu,F}^{R_f I} = \left(\frac{\partial Y_2(h,u)}{\partial R_f}(\Delta V_h - \Delta V_u) + \left(\frac{\partial \Delta V_u}{\partial R_f} - \frac{\partial \Delta V_h}{\partial R_f}\right) Y_{hu}\right)^{-1}.$$

It should be mentioned that for cases where fault is on the line whose current is measured, $S_{hp,F}^{DI}$ and $S_{hp,F}^{R_f I}$ are calculated with $p = n + 1$ due to an additional bus at the fault location.

Equations (3) and (4) present observant bus h voltage and current sensitivity indices with respect to fault location D and impedance R_f for any fault $F = (l_f, D,\ R_f)$. Let $F(l_f) = (l_f, .,.)$ represent all faults on system line l_f with varying $0 \le D \le 1$ and $0 \le R_f \le R_{max}$. Therefore, $S_{h,F(l_f)}^{DV}$, $S_{h,F(l_f)}^{R_f V}$, $S_{hu,F(l_f)}^{DI}$, and $S_{hu,F(l_f)}^{R_f I}$ are observant bus h sensitivity indices for all possible faults on line l_f. Hence, all observant bus (h) measurement sensitivities can be evaluated for all possible faulty lines (l_f). Subsequently, any observant bus h measurement can be qualified to detect faults on a group of system lines, and the final possible PMU set should be optimized in a way to cover all system lines regarding measurement sensitivity for fault detection. On the other hand, a unique function mapping between the PMU set's measurements and system faults is possible as long as there is no multi-estimation. Multi-estimation is a condition where different faults in the power system cause similar measured values in a set of observant buses with available precisions. Exhaustive search is used in this chapter to guarantee that the selected PMU set's measurements, that satisfy the sensitivity criteria, have distinguishable values for all possible faults throughout the power system.

Definition: Consider an observant set $H \subseteq \{1,2,\dots,N\}$. Measurement set M_{HF} corresponding to fault F is defined as $M_{HF} = \{\Delta V_{h,F}, \Delta I_{hu,F} | h \in H, u \in U_h\}$ where U_h is an adjacent set to observant bus h.

1.5. Sensitivity Analysis Criteria for OPP for Fault Location and Observability

1.5.1. Sensitivity Requirements

Low values of the defined sensitivity indices (3-4) make measurements sensitive to fault location D and impedance R_f and thus are desirable. Let $F(l_f) = (l_f, ., .)$ represent all faults on grid line l_f with varying $D \in \mathbf{D} = [0,1]$ and $R_f \in \mathbf{R_f} = [0, R_{max}]$. Then, sensitivity indices (3) and (4) can be defined for $F(l_f)$ where l_f is the faulty line number ($l_f \in \boldsymbol{L_f}$). The sensitivity indices regarding each observant bus h and each faulty line l_f include one $S^{DV}_{h,F(l_f)}$, one $S^{R_fV}_{h,F(l_f)}$, h_c many $S^{DI}_{hu,F(l_f)}$, and h_c many $S^{R_fI}_{hu,F(l_f)}$where h_c is the number of connected buses (lines) to observant bus h as explained.

Consider line l_f, observant bus h, and adjacent buses $u \in U_h$. Define measurement sensitive range sets as

$$\Theta^{DV}_{h,F(l_f)} = \left\{ (D, R_f) \middle| \begin{matrix} D \in \mathbf{D}, R_f \subseteq \mathbf{R_f}, F = (l_f, D, R_f), \\ S^{DV}_{h,F} \leq \varepsilon_{DV} \end{matrix} \right\},$$

$$\Theta^{R_fV}_{h,F(l_f)} = \left\{ (D, R_f) \middle| \begin{matrix} D \in \mathbf{D}, R_f \subseteq \mathbf{R_f}, F = (l_f, D, R_f), \\ S^{R_fV}_{h,F} \leq \varepsilon_{R_fV} \end{matrix} \right\},$$

$$\Theta^{DI}_{hu,F(l_f)} = \left\{ (D, R_f) \middle| \begin{matrix} D \in \mathbf{D}, R_f \subseteq \mathbf{R_f}, F = (l_f, D, R_f), \\ S^{DI}_{hu,F} \leq \varepsilon_{DI} \end{matrix} \right\}, \text{ and}$$

$$\Theta^{R_fI}_{hu,F(l_f)} = \left\{ (D, R_f) \middle| \begin{matrix} D \in \mathbf{D}, R_f \subseteq \mathbf{R_f}, F = (l_f, D, R_f), \\ S^{R_fI}_{hu,F} \leq \varepsilon_{R_fI} \end{matrix} \right\} \qquad (6)$$

where ε terms indicate desired sensitivity thresholds. That is, for example, set $\Theta^{DV}_{h,F(l_f)}$ contains all faults on line l_f for which voltage at observant bus h is sensitive to the fault distance (D). Similarly, set $\Theta^{R_fI}_{hu,F(l_f)}$ contains all faults on line l_f for which current in line hu (that is measured at observant

bus h) is sensitive to the fault impedance (R_f). Now, define, $\Theta^{D}_{h,F(l_f)} = \Theta^{DV}_{h,F(l_f)} \cup \left(\underset{u \in U_h}{\cup} \Theta^{DI}_{hu,F(l_f)} \right)$, $\Theta^{R_f}_{h,F(l_f)} = \Theta^{R_f V}_{h,F(l_f)} \cup \left(\underset{u \in U_h}{\cup} \Theta^{R_f I}_{hu,F(l_f)} \right)$, and $\Theta_{h,F(l_f)} = \Theta^{D}_{h,F(l_f)} \cap \Theta^{R_f}_{h,F(l_f)}$.

Set $\Theta^{D}_{h,F(l_f)}$ includes all faults on line l_f with fault distances for which voltage or some current measurements at observant bus h are sensitive to. Similarly, set $\Theta^{R_f}_{h,F(l_f)}$ includes all faults on line l_f with fault impedances for which voltage or some current measurements at observant bus h are sensitive to. Set $\Theta_{h,F(l_f)}$ includes all faults on line l_f with distances and impedances for which voltage or some current measurements at observant bus h are sensitive to. Set $\Theta_{h,F(l_f)}$ may include all or some faults of interest on line l_f for $\exists l_f \in \boldsymbol{L_f}$. Thus, in general, additional observant buses must be used to include all faults of interest on all system lines; i.e., for $\forall l_f \in \boldsymbol{L_f}$.

Fault location (for all faults F) is possible if an observant set can find all faults in regions $\mathbf{D} \times \mathbf{R_f}$ for all power system lines. That is, for any faulty line $l_f \in \boldsymbol{L_f}$, there must exist an observant set H such that $\underset{h \in H}{\cup} \Theta_{h,F(l_f)} = \mathbf{D} \times \mathbf{R_f}$.

In practice, realization of such condition may be difficult, especially for high values of fault impedance, and thus, a slightly simpler (and probably more conservative) approach is selected here to simplify calculations. In this research it is an objective to select observant buses that are able to locate at least 90% of all possible faults in region $\mathbf{D} \times \mathbf{R_f}$ on each faulty line $l_f \in \boldsymbol{L_f}$. This criterion is selected based on experience and to add some flexibility in observant bus selection. Consequently, due to piecewise continuity of the sets defined above, an observant bus h is chosen if for $\exists l_f \in \boldsymbol{L_f} = \{1,2, \dots L\}$ condition (7-a) or (7-b) is satisfied:

$$SVID = \left(\iint_{\Theta^{DV}_{h,F(l_f)}} dDdR_f \geq S_{DR} \right) \vee \left(\underset{u \in U_h}{\vee} \left(\iint_{\Theta^{DI}_{hu,F(l_f)}} dDdR_f \geq S_{DR} \right) \right) \qquad \text{(7-a)}$$

$$SVIR_f = \left(\iint_{\Theta_{h,F(l_f)}^{R_f V}} dDdR_f \geq S_{DR} \right) \vee \left(\bigvee_{u \in U_h} \left(\iint_{\Theta_{hu,F(l_f)}^{R_f I}} dDdR_f \geq S_{DR} \right) \right) \quad (7\text{-b})$$

where $S_{DR} = 0.9 \iint_{\mathbf{D} \times \mathbf{R_f}} dDdR_f = 0.9R_{max}$. Condition SVID implies that observant bus h is sensitive to the distance of 90% of the faults, indicated by region $\mathbf{D} \times \mathbf{R_f}$, on line l_f. Similarly, SVIRf implies that observant bus h is sensitive to the impedance of 90% of the faults indicated by region $\mathbf{D} \times \mathbf{R_f}$ on line l_f. Subsequently,

$$SVIDR_f = SVID \wedge SVIR_f \quad (8)$$

with binary value $SVIDR_f$, is used to determine if observant bus h is capable of illustrate (using its measurements) the changes in distance and/or impedance of a vast majority of the faults of interest that occur on line l_f with the desired precisions indicated by (6). Condition (8) will be checked for all the power system lines to find observant bus h's domain of fault coverage. This step will reduce the number of required observant buses in obtaining fault observability in the entire system. In practice, one observant bus may not cover the faults on all the power system lines and thus other observant buses must be exploited so that faulty lines that are not observed by one observant bus are observed by others. Thus, the above process is repeated for all the power system's buses to lay out an initial mapping between the faults of interest and the power system buses as observant buses. A group of observant buses; i.e., an observant set, if one exists, that satisfies condition (8) for all $l_f \in \boldsymbol{L_f}$ provides a solution to the fault location problem and thus renders the power system fault observable. This is equivalent to an observant set whose measurements (measurement set) are sensitive to 90% of distances or impedances of the faults on all power system lines.

1.5.2. Uniqueness and Multi Estimation

After finding sensitive bus locations for measurement allocation, multi estimation is a necessary criterion to check in order to assure that a measurement set is capable of locating all possible faults in the power system uniquely. The ability of precisely locating a fault in the system, depends on distinguishable measurements for any two different faults in the system.

Multi estimation exists if for an observant set $H \subseteq \{1,2,\dots,N\}$ and two faults $F_1 = (l_{f1}, D_1, R_{f1})$ and $F_2 = (l_{f2}, D_2, R_{f2})$ where $F_1 \neq F_2$ all corresponding measurements from the observant set H are the same; i.e., $M_{HF_1} = M_{HF_2}$ (See Section II). Analytically, for any pair of faulty lines $l_{f1}, l_{f2} \in \boldsymbol{L_f}$ and observant bus $h \in H$, this results in the following nonlinear equalities in terms of D_1, R_{f1}, D_2, and R_{f2} for $\forall u \in U_h$:

$$\begin{cases} \Delta V_{h,F_1} - \Delta V_{h,F_2} = 0 \\ \Delta I_{hu,F_1} - \Delta I_{hu,F_2} = 0 \end{cases}. \qquad (9)$$

Total number of faulty line pairs ($l_{f1}, l_{f2} \in \boldsymbol{L_f}$) is $\frac{L(L+1)}{2}$ where L is the number of power lines in the power system. This number includes combinations of any two different lines plus the number of power system lines (L) in order to account for multi estimations on the individual lines. Thus, for each observant bus h in set H, (9) represents $\frac{L(L+1)}{2}(h_c + 1)$ many equations, where h_c is the number of connected buses (lines) to observant bus h as explained in Section II. For unique fault location and fault observability, multi estimation must not occur. That is, for $l_{f1} \neq l_{f2}$, (9) must result in no solutions whereas for $l_{f1} = l_{f2}$, it must yield $D_1 = D_2$ and $R_{f1} = R_{f2}$. Equations (9) can be formed by employing (1) and (5) that lead to nonlinear equations that can be solved numerically.

This approach in the simplest form can represented as an optimization problem in the form of $\min_{(l_f, D, R_f)} W^T X$ under constrains (8) and (9) where X is an $N \times 1$ vector with its elements (0 or 1)

represents selection of an observant bus , and $W = [w_1, w_2, \dots, w_N]^T$ is a weight matrix that reflects practical or operational priorities in selecting observant buses with $0 \leq w_i \leq 1$. The cost function can be developed further to include other constraints such as contingencies, etc., but is not the objective of this chapter and not further discussed here and thus an exhaustive search is used to solve the OPP problem.

1.6. Proposed Algorithm for OPP and Artificial Neural Network Fault Locator

Previous works consider optimal PMU placement with much emphasis on the PMU cost as a weight vector in the optimization problem. However, measurement precision and bus suitability for fault observability are mostly neglected in assigning PMU locations [6]–[16]. PMU fault location capability is a function of its location in the system. Measurement from a PMU installed in an improper location may cause significant inaccuracy in fault location. The proposed formulation and algorithm in this chapter aims to thoroughly consider this. Power system buses have to be checked and conditions (7) and (9) be evaluated to obtain appropriate observant set H. These conditions can be evaluated through solving (7) and (9) for all grid buses so that a set of appropriate observant buses are selected, and can be translated to sensitivity and uniqueness conditions required for fault observability and location. Numerical solutions can be sought to evaluate observant buses which are explained next. Before we proceed, the following discussions are conducted.

Remark (Measurement Precision): IEEE C57.13 standard for instrumentation transformers suggests 0.3% error for current and voltage transformer [20]-[21]. Since PMU measurement precision is usually higher than that of the instrumentation, precisions of 1%, and 0.1% are considered in this study for both current and voltage measurements total vector error (i.e.,

TVE^V and TVE^I), where $TVE^x = \left|\frac{X_{measured} - X_{theoritical}}{X_{theoritical}}\right| \times 100\%$ [22]. It is worth mentioning that accurate phasor estimation can be made during fault transients [22]-[25]. Nevertheless, in this study fault duration is considered to be 0.1 second, which is 6 cycles at 60 Hz and is equal to the operating time of the circuit breakers. Since the transients caused by the faults are generally damped within 2 cycles [26], an installed PMU has enough time to measure the steady-state fault phasors. In case a severe fault occurs at a PMU location, the amplitude of the measured voltage or current phasors can be very inaccurate; however, the proposed method exploits multiple measurements across the grid to assure that enough accurate measurements are taken.

Fault Location Precision: Define TP^D as "*target precision for fault distance D*". Also, define TP^{R_f} as "*target precision for fault resistance* R_f". Note that fault location range is $0 \leq D \leq 1$ on a power line and thus for a given $TP^D \leq 1$, fault can be located on one of $\frac{1}{TP^D} + 1$ equally-spaced points on any power line. Also, if fault resistance range of interest is $0 \leq R_f \leq R_{max}$, for the given TP^{R_f} the fault resistance can be any of $\frac{R_{max}}{TP^{R_f}} + 1$ equally-spaced resistances between 0 and R_{max}.

From the above discussion, the desired upper limits for sensitivity indices (3) and (4) can be calculated as

$$S_{h,F}^{DV} \leq \frac{TP^D}{TVE^V} = \varepsilon_{DV}, \quad S_{h,F}^{R_fV} \leq \frac{TP^{R_f}}{TVE^V} = \varepsilon_{R_fV}, \; S_{hu,F}^{DI} \leq \frac{TP^D}{TVE^I} = \varepsilon_{DI}, \text{ and } \quad S_{hu,F}^{R_fI} \leq \frac{TP^{R_f}}{TVE^I} = \varepsilon_{R_fI} \tag{10}$$

for all $h \in \{1,2,\dots,N\}$ and $u \in U_h$. For example, for $TP^D = 0.01$, $TP^{R_f} = 0.05$, $TVE^V = 0.1\%$, and $TVE^I = 0.1\%$ one has $\varepsilon_{DV} = 10$, $\varepsilon_{R_fV} = 50$, $\varepsilon_{DI} = 10$, and $\varepsilon_{R_fI} = 50$.

So far, the relationship between sensitivity indices (3) and (4) and the fault location and impedance accuracy is explained. Thresholds (10) can be utilized to evaluate the quality of observant bus h. Once the sensitivity measures (3) and (4) are obtained as functions of fault $F = (l_f, D, R_f)$, they can be compared with thresholds (10) across all variations of faulty line l_f, location D, and

impedance R_f to determine if observant bus h is a good choice. In addition, conditions to check the multi estimation are introduced. The algorithm to find optimal PMU sets introduced, which comes next.

Proposed Algorithm

1) Enter the algorithm inputs: TP^D, TP^{R_f}, TVE^V, TVE^I and S_{DR}. Calculate the sensitivity thresholds ε_{DV}, ε_{R_fV}, ε_{DI} and ε_{R_fI} using (10).
2) Select an observant bus h and a faulty line $l_f \in \boldsymbol{L_f}$ and obtain the sensitivity indices (3) and (4) for fault $F = (l_f, D,\ R_f)$ for all $D \in \mathbf{D}$ and $R_f \in \mathbf{R_f}$ with (target precisions) TP^D and TP^{R_f} steps, respectively. That is, sensitivity indices are evaluated on all $\frac{1}{TP^D} + 1$ equally-spaced points on line l_f and all the $\frac{R_{max}}{TP^{R_f}} + 1$ equally-spaced resistances between 0 and R_{max}.
3) Obtain sensitivity ranges (6) by comparing the sensitivity indices of Step 2 with thresholds ε_{DV}, ε_{R_fV}, ε_{DI} and ε_{R_fI} of Step 1.
4) Check sensitivity criteria (ability to find the fault distance and impedance with desired accuracies TP^D and TP^{R_f} of Step 1) of observant bus h for fault location on line l_f through evaluating (7-a), (7-b), and (8).
5) Repeat Steps 2 to 4 for all lines $l_f \in \{1,2, \dots, L\}$ and store the lines for which fault distance and impedance can be determined with desired accuracy using observant bus h . This step also determines how many faulty lines are observable by observant bus h (rank of bus h).
6) Repeat Step 5 for all observant buses $h \in \{1,2, \dots, N\}$.
7) Form all possible observant sets passing sensitivity criteria. An individual observant bus may not satisfy criteria (8) for all faults of interest in the power system. That is, not all faulty lines may be observable by an individual observant bus due to missing some fault locations or

impedances. However, a set of observant buses (that may not be unique) may be capable of observing all faulty lines; that is, there may exist an observant set that satisfy criterion (8) for all grid lines. Such an observant set is capable of finding faulty lines, distances, and impedances of all faults through various voltage and current measurements. In many power systems a trivial set of such observant set is the entirety of the power system buses. However, in the majority of power systems, a smaller number of observant buses forming an observant set can serve and observe all faulty lines (determining fault locations and impedances). In this step, combinations of observant buses forming such observant sets, with minimum number of observant buses obtained and saved. This starts by examining one-observant-bus sets, two-observant-bus sets, three-observant-bus sets, etc. As soon as an observant set that satisfies (8) is found, one optimal observant set is obtained to be checked against multi estimation.

8) Check for multi estimation. Each observant set obtained in Step 7 must be checked against multi estimation. Select an observant set (obtained in Step 7). Select a pair of faulty lines $l_{f1}, l_{f2} \in \boldsymbol{L_f}$. Equations (9) must yield no solutions but the trivial solution$F_1 = F_2$, for selected lines l_{f1}, l_{f2} for the measurement set of the selected observant set. Discard the measurement set if equations (9) yield non-trivial solutions; i.e., two faults yield similar measurement sets in the selected observant set.

9) Repeat Step 8 for all $\frac{L(L+1)}{2}$ power line pairs for each set.

10) Collect all the observant sets that pass Step 9. The observant sets with minimum number of observant buses are chosen as the optimal measurement set(s). This in turn determines the optimal PMU locations. Among the optimal sets the set with the maximum number of measurements outperforms and is chosen.

A flowchart of the proposed algorithm is depicted in Figure 2.4 to clarify these steps.

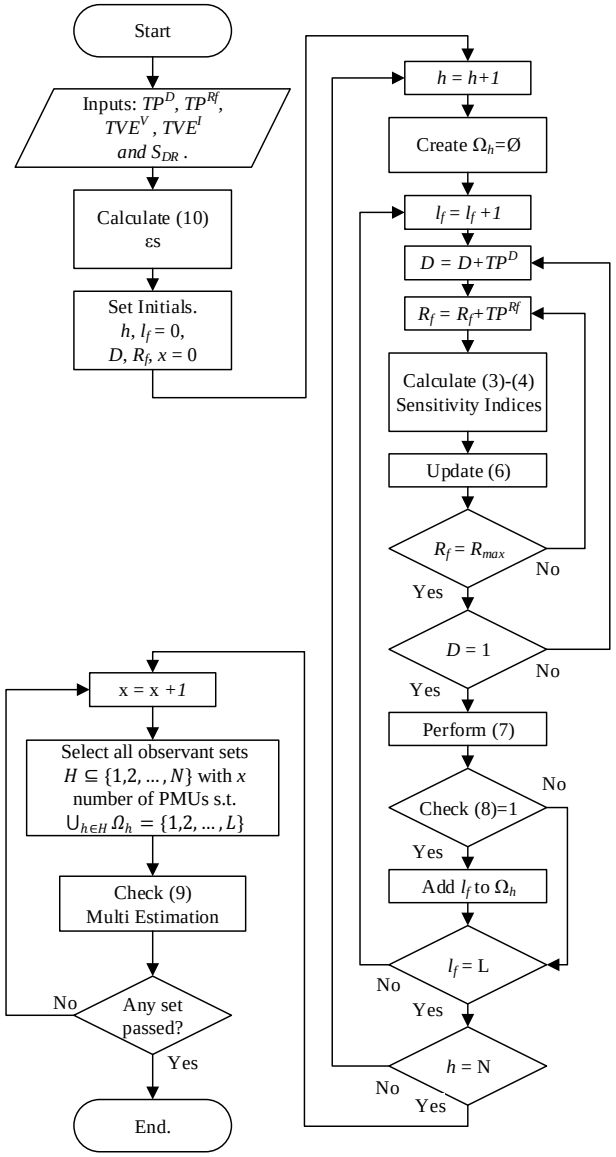

Figure 2.4: Flowchart representation of the proposed algorithm

1.7. An Example using IEEE 7-Bus Case

In this section the proposed methodology and algorithm is explained using numerical examples and IEEE 7-bus test case depicted in Figure 2.3. The derived four sensitivity indices in equations (3) and (4) can be calculated for any power system where IEEE 7-bus here is used as an example. It should be mentioned that these sensitivity indices can be presented as a continuous function using the final derived formulation. Figures 2.5a.1 and 2.5a.2 depict voltage ΔV_4 magnitude and angle for all possible faults on line 7 connecting bus 1 to 4. These figures illustrate

the changes observed in the observant bus 4 in the effect of all possible faults on the aforementioned line.

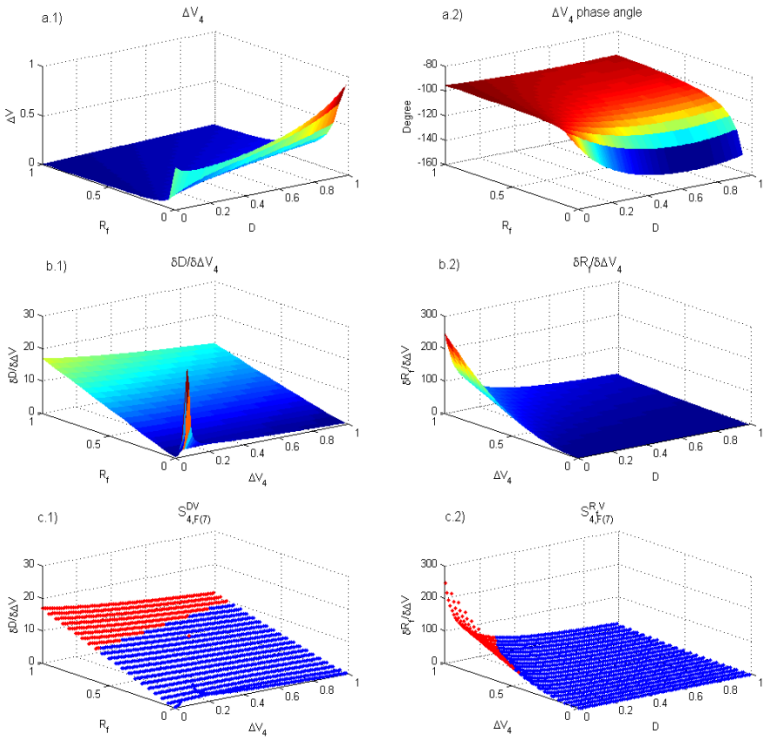

Figure 2.5: Bus 4 voltage sensitivities for F= (7, $0 \leq D \leq 1$,$0 \leq R_f \leq 1$)

Voltage sensitivity indices with respect to D and R_f are calculated (equation 3 $S_{h,F}^{DV} = \left(\frac{\partial \Delta V_h}{\partial D}\right)^{-1} = \frac{\partial D}{\partial \Delta V_h}$) and illustrated in Figure 2.5b.1 and 2.5b.2, respectively. It should be mentioned that these figures present the continuous version of the derived methodology. However, such continuous functions might not be necessary considering the explained target precisions for fault location in subsection 4 but also accompanies with computational burden and expenses. One the other hand, discrete version of $S_{4,F(7)}^{DV}$ and $S_{4,F(7)}^{R_f V}$ are calculated and depicted in Figure 2.5c.1 and 2.5c.2 with their region meeting condition (10), which is also incorporated in (6), depicted in blue. Undesired sensitivities depicted in red are due to faults that cause low impacts on voltage change with changes in D and R_f. The projection of the desired sensitivity on the $D \times R_f$ plane represents values for D and R_f for which sensitivity indices satisfy (6). These regions are where faults on the

line 7 causes measurements at the observant bus 4 with enough resolutions to distinguish faults occurring on the line. The percentage of this projection with respect to total $D \times R_f$ plane is presented in Figure 2.6 for all observant buses and all faulty lines, and a minimum of 90% is considered in this chapter for satisfactory sensitivity indices.

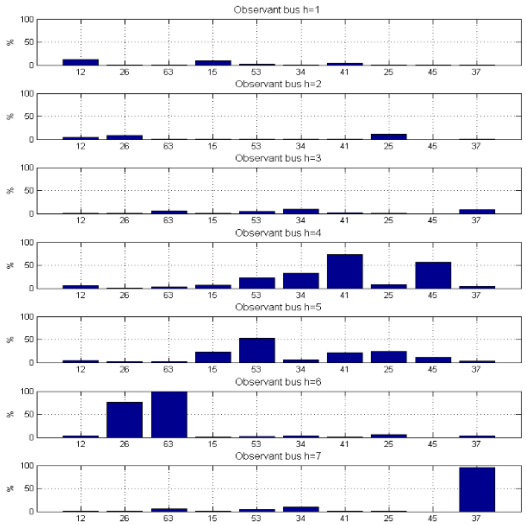

Figure 2.6: Percentages of **satisfactory *D*-voltage** sensitivity indices for all faulty lines per each observing bus regarding $S_{h,F}^{DV} \leq \varepsilon_{DV} = 10$

The 90% minimum observant bus fault coverage can be used to convert Figure 2.6 to a binary matrix form for "sensitivity of D with respect to Voltage (SDV)" as:

$$SDV_{7-bus} = \begin{bmatrix} 0 & 0 & 0 & 0 & 0 & 0 & 0 & 0 & 0 & 0 \\ 0 & 0 & 0 & 0 & 0 & 0 & 0 & 0 & 0 & 0 \\ 0 & 0 & 0 & 0 & 0 & 0 & 0 & 0 & 0 & 0 \\ 0 & 0 & 0 & 0 & 0 & 0 & 0 & 0 & 0 & 0 \\ 0 & 0 & 0 & 0 & 0 & 0 & 0 & 0 & 0 & 0 \\ 0 & 0 & 1 & 0 & 0 & 0 & 0 & 0 & 0 & 0 \\ 0 & 0 & 0 & 0 & 0 & 0 & 0 & 0 & 0 & 1 \end{bmatrix}$$

This binary matrix represents the first part of the equation (7-a) which is mainly for algorithm purposes. Where logic 1 in any (h,l_f) entree shows that bus h is qualified to observe faults on line l_f regarding $S_{h,F(l_f)}^{DV} \leq \varepsilon_{DV}$ criteria with over 90% coverage. Similarly for $S_{h,F}^{R_fV}$, $S_{hu,F}^{DI}$, and $S_{hu,F}^{R_fI}$, corresponding binary matrices can be calculated which are SR_fV, SDI, and SR_fI. It should be mentioned that for sensitivities with respect to line currents, a bus with multiple lines should meet

the condition mentioned in (6) for at least one of its connected lines measurements. In a similar way, the binary matrix for qualified observant buses to detect faults on all system lines (first part of the equation (7-b)) can be calculated as:

$$SRfV_{7-bus} = \begin{bmatrix} 0 & 1 & 1 & 0 & 1 & 1 & 0 & 0 & 0 & 1 \\ 0 & 0 & 0 & 1 & 1 & 1 & 1 & 0 & 1 & 1 \\ 1 & 1 & 0 & 1 & 0 & 0 & 1 & 1 & 0 & 0 \\ 0 & 0 & 0 & 0 & 0 & 0 & 0 & 0 & 0 & 0 \\ 0 & 0 & 0 & 0 & 0 & 0 & 0 & 0 & 0 & 0 \\ 0 & 0 & 0 & 1 & 0 & 0 & 1 & 0 & 0 & 0 \\ 1 & 1 & 0 & 1 & 0 & 0 & 1 & 1 & 0 & 0 \end{bmatrix}.$$

An exact methodology is used for measurement currents with the difference that an installed PMU can measure all line currents connected to that bus. That's why the percentage coverage sensitivity indices illustrated in Figure 2.7 for current has more figures for each bus depending on the lines connected to that specific bus. Also, from all line current measurements one qualified measurement is enough to be sensitive to the faults occurring on a specific line. Figure 2.7 illustrates the percentages of satisfactory D-current sensitivity indices for all faulty lines per each observing bus:

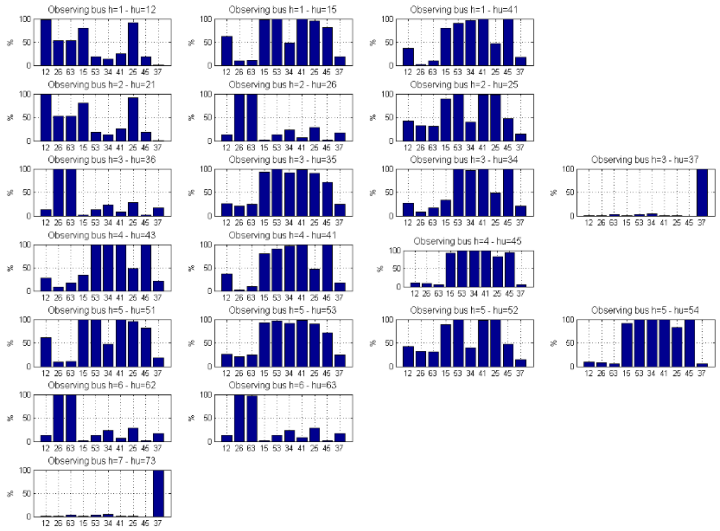

Figure 2.7. Percentage of **satisfactory *D*-current** sensitivity indices for all faulty line per each observing bus line regarding $S_{hu,F}^{DI} \leq 10$

From the above discussion, all sensitivity final binary matrices can be calculated. Figure 2.8 symbolically illustrates the proposed logic after deriving sensitivity binary matrices. An OR logic

is applied on SDV and SDI. An AND logic is used between the resultant $SDVI$ and SR_fVI as an observant bus h should meet both criteria to detect both D and R_f in a fault incident. Finally, the final sensitivity decision-making matrix SDR_f for this example is

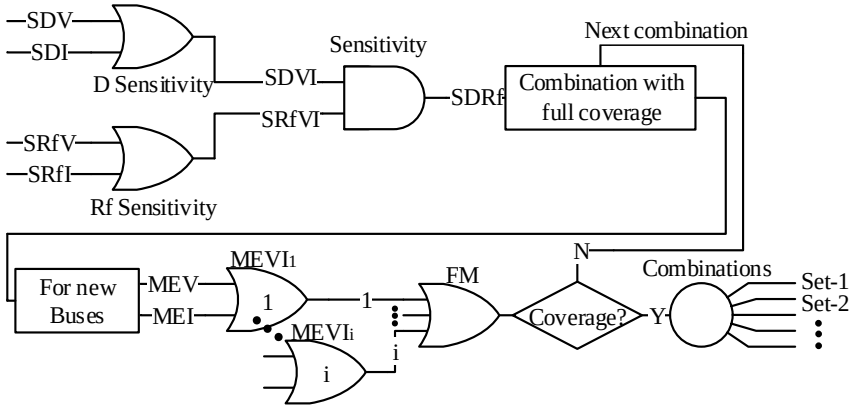

Figure 2.8: Algorithm logic diagram

$$SDR_{f_{7-bus}} = \begin{bmatrix} 1 & 0 & 0 & 1 & 1 & 1 & 1 & 1 & 1 & 0 \\ 1 & 1 & 1 & 0 & 1 & 0 & 1 & 1 & 0 & 0 \\ 0 & 1 & 1 & 1 & 1 & 1 & 1 & 1 & 1 & 1 \\ 0 & 0 & 0 & 1 & 1 & 1 & 1 & 0 & 1 & 0 \\ 0 & 0 & 0 & 1 & 1 & 1 & 1 & 1 & 1 & 0 \\ 0 & 1 & 1 & 0 & 0 & 0 & 0 & 0 & 0 & 0 \\ 0 & 0 & 0 & 0 & 0 & 0 & 0 & 0 & 0 & 1 \end{bmatrix}.$$

Using final sensitivity matrix (SDR_f), PMU sets are generated with the condition that all system lines are covered by available PMUs in each set. Later, each PMU set is checked for multi-estimation for all buses of interest and their related lines in which their sensitivity criteria is maintained. Multi-estimation process results in a symmetrical $L \times L$ matrix ($\mathrm{MEVI_h}$) in which lines that have multi-estimation with each other are assigned 0. Multi-estimation is carried out for both voltage and currents for each bus, and just one voltage or current is adequate to have no multi-estimation, represented by logic 1, in the related entree in final matrix $\mathrm{MEVI_h}$. Again, in buses with multiple lines one line is enough to not have a multi-estimation since it makes the fault distinguishable. Finally, for each set of PMU to cover all system lines for fault observability without multi-estimation, the condition $\bigvee_{i \in set} \mathrm{MEVI_i} = \mathrm{FM} = 1$ should meet. The algorithm

presented in Figure 2.8 halts once first set of PMUs causing full coverage without multi-estimation is found and provides all possible combinations for this set of PMUs passing the criteria. In the results provided in the next sections, this is modified to find all possible combination with the minimum number of PMUs in the sets.

1.8. Artificial Neural Network (ANN) Fault Locator

Once the optimal observant set is obtained, it is assured that the set can locate all faults of interest uniquely without multi estimation. Thus, a one-to-one map exists between the corresponding measurement set and the faults of interest (that includes the faulty line, the fault distance, and impedance). Consequently, artificial neural networks (ANNs) are capable of and used to map the measurement set (from the optimal observant set) to their related faults comprising faulty line l_f, distance D, and resistance R_f. As an example, here we assume that H = {2,3} is an OPP solution for the IEEE 7-bus example case in previous section. Therefore, resulting measurements in such set will be $M_{HF} = \{\Delta V_{h,F}, \Delta I_{hu,F} | h \in H, u \in U_h\}$ = $\{V_2,\ I_{2g}, I_{21}, I_{26}, I_{25}, V_3, I_{3g}, I_{34}, I_{35}, I_{36}, I_{37}\}$. Therefore, the explained one-to-one function mapping between all system faults and OPP set measurements can be illustrated using these two equation which are also visually depicted in Figure 2.9.

- $f_{(l_f, D, R_f)} = M_{HF} = (V_2,\ I_{2g}, I_{21}, I_{26}, I_{25}, V_3, I_{3g}, I_{34}, I_{35}, I_{36}, I_{37})$
- $f^{-1}_{(V_2, I_{2g}, I_{21}, I_{26}, I_{25}, V_3, I_{3g}, I_{34}, I_{35}, I_{36}, I_{37})} = F = (l_f, D,\ R_f)$

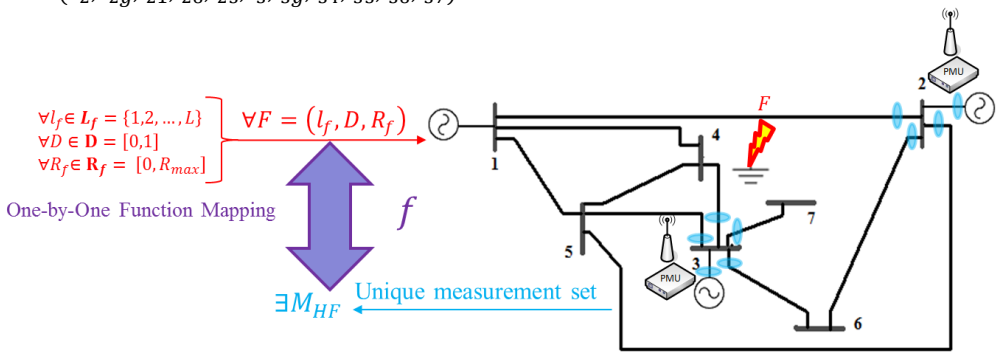

Figure 2.9: IEEE 7-bus test system fault observability using OPP

Artificial neural networks are intelligent mechanisms that can approximate complex nonlinear functions through employing a set of input and output data [27]. The function approximation property of the ANNs is used here to estimate the function that maps the measurement set as input and related fault as output. Offline training is used and corresponding weights and bias values of the ANN are obtained using MATLAB via the Levenberg-Marquardt optimization method [29] which is an efficient method in training feedforward ANNs. The artificial neural networks here have one hidden layer and one output layer with sigmoid and linear activation functions, respectively.

In this study, instead of using one large neural network, a structure of networks is employed in order to have a more precise fault locator. That is, faulty line l_f is found in the first neural network using input data from the measurement set. Then, based on the detected faulty line, a pertinent neural network is activated to determine fault distance D, and resistance R_f, as shown in Figure 2.10. Input vector X of the first ANN is the measurement set's (corresponding to the obtained OPP) voltage and current magnitudes and angles. Output vector Y_1 is the faulty line l_f. That is, $Y_1 = W^T\,\Phi(V^T\,X)$ where W_1 is the output layer weight matrix, Phi is the Sigmoid activation function, and V_1 is the hidden layer weight matrix. Next, a second ANN is selected corresponding to the resultant faulty line from the first ANN. In the second ANN, the input vector is X as explained and output vector $Y_2 = \left[D\ R_f\right]^T$ is the location and resistance of the fault located on faulty line l_f. That is, $Y_2 = W_{lf}^T\,\Phi(V_{lf}^T\,X)$ where W_{lf} is the output layer weight matrix, Phi is the Sigmoid activation function, and V_{lf} is the hidden layer weight matrix corresponding to faulty line l_f.

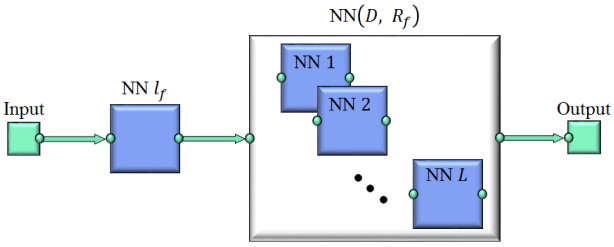

Figure 2.10: Neural networks structure

The individual ANNs are trained separately using relevant generated fault data. All ANNs utilize one hidden layer whose number of neurons vary with the size of the grid (e.g., 20–40 neurons for 7-bus and 35–65 neurons for 30-bus grid) where higher number of neurons are used for higher-precision scenarios (lower TP^D and TP^{R_f}). Approximately 20% of the generated fault data is separated and used to test the trained neural networks. Neural network fault locator results presented (next section) are the percentage of the correct estimations for this portion of data. More ANN design data is provided in the tables in the next section.

1.9. Proposed Algorithm Results and Discussion

The presented algorithm in the last section is performed on the IEEE 7-bus (Figure 2.3), IEEE 14-bus and IEEE 30-bus [28] test systems in order to assess the performance of proposed algorithm and obtained optimal PMU set in fault location. The test systems consist of 3, 2, and 6 generators as well as 10, 21, and 42 transmission lines, respectively [29]. Once the proposed algorithm finds the optimal observant set(s) for each power system, artificial neural networks are utilized to obtain a fault locator using the observant set. The artificial neural networks are trained by known fault data that are measured by the optimal PMU set (observant set) and create a one-to-one map between the measurement set and the fault causing it; i.e., fault line, distance, and impedance. After the training is completed, the ANN fault locator is tested by new fault data and accuracy of fault location is examined.

Fault impedance is considered to be purely resistive in this study [16]. The maximum fault resistance of the interest is considered to be $R_{max} = 17.4$ for all test cases, i.e., 0.1 p.u in 132 kV base voltage. By increasing the required maximum fault resistance of interest to be detected by an observant set the number of PMUs in the found set may increase since the set performance is demanded to cover higher resistance faults. Various voltage and current measurement precisions are used to solve the OPP problem in order to include various PT and CT precisions.

Table 2.1 presents OPP results for the IEEE 7-bus system. Two cases are performed in the simulation: with target precisions of 1% for fault distance D and resistance R_f, and with target precisions of 5% for D and R_f. These precisions are the desired fault location accuracies here and thus they are used in generating faults that are used in training and testing the ANN fault locator.

Table 2.1: IEEE 7-bus OPP and ANN results for various target precisions and different measurements accuracies

IEEE 7-bus OPP ($R_f$max 0.1 pu)				**ANN**		
TVE^V	TVE^I	# PMUs	Optimal observant sets (PMU locations)	Percentage estimation accuracy		
				l_f	D *(ave) (min)*	R_f *(ave) (min)*
$\boldsymbol{TP^D = 0.01, TP^{R_f} = 0.01,}$ Total generated faults: 11000						
10^{-2}	10^{-2}	2	(1,2)-**(2,3)**	99.6	99.9 99.1	99.9 99.5
10^{-3}	10^{-2}	2	(1,2)-**(2,3)**	99.8	100 100	100 100
10^{-3}	10^{-3}	1	(1)-(2)-(3)-**(5)**	99.9	100 100	100 100
$\boldsymbol{TP^D = 0.05, TP^{R_f} = 0.05,}$ Total generated faults: 600						
10^{-2}	10^{-2}	1	(3)-(**5**)	99.1	99.1 91.6	100 100
10^{-3}	10^{-2}	1	(3)-(**5**)	99.1	99.1 91.6	100 100
10^{-3}	10^{-3}	1	(1)-(2)-(3)-(4)-(**5**)-(6)	100	99.1 91.6	100 100

The first two columns of Table 2.1 show voltage and current measurement precisions. These precisions are used in solving the OPP in the proposed algorithm where sensitivity indices are utilized. Columns 3 and 4 represent the minimum number of required PMUs and the optimal observant set(s) that the proposed algorithm suggests. The artificial neural network fault locator is

trained by employing the optimal observant set shown in **bold**. For the case with 1% target precisions for D and R_f, 11,000 fault scenarios are generated throughout the system and used for ANN training and 2,200 fault data are used for test and validation. Similarly, for the case with 5% target precision for D and R_f, 600 fault scenarios are used for training and 120 fault scenarios are used for validation. The remaining columns show the accuracy of fault location using the trained ANN fault locator. The fault locator has dedicated artificial neural networks for each line in its second stage and after the faulty line is found as shown in Fig. 5. The top and bottom percentage values in the last two columns show the average and minimum estimation accuracies, respectively, across all network lines. One can observe that by using current and voltage precision of 10-2 (1%) only two optimal observant sets with 2 PMUs in each set are found by the proposed algorithm. The minimum number of PMUs and the optimal observant sets remain the same by increasing only the voltage precision to 10-3. However, when increasing the current measurement precision to 10-3 (0.1%) only one PMU is enough for the system to be fault observable. On the other hand, by reducing the preferred precision for the fault location (the target precision of 5%), only one PMU is capable of observing all system faults.

Tables 2.2 and 2.3 present the results of the proposed OPP and ANN locators for IEEE 14-bus and 30-bus systems. The bus numbers given in [28] are adopted here for the power systems. It is observed that higher current measurement precision is more effective than that of voltage in reducing the number of required PMUs as shown in the tables. Overall, these results show the impact of measurement precision on OPP solutions which is detailed for the first time here. In addition, provided results illustrate a significant improvement over the conventional one-bus-spaced method where approximately 50% of buses are required for the system fault observability [7], [15]. For example the number of suggested PMUs for one-bus-spaced method is 17 [15] for

the IEEE 30-bus system as opposed to 13 PMUs obtained here using 10-2 measurement precision. Moreover, [15] proposes 14 PMUs for the IEEE 30-bus system when considering 6 zero-injection buses (that reduce grid size) and [7] proposes 8 PMUs using 15 additional flow measurements. By contrast, the proposed algorithm suggests 13 PMUs using 10-2 measurement precision and 2 PMUs using 10-3 measurement precision with the desired fault location accuracy of 1% for both fault distance and impedance. Table 2.4 summarizes the results of references [7] and [15] that employ Integer Linear Programming (ILP) in the context of one-bus-spaced strategy for full system fault observability. Note that the measurement precision is not considered and elaborated in these works whereas the precision plays an important role in the number of required measurement units. That is, higher fault location and/or impedance precision need larger numbers of employed PMUs.

Table 2.2: IEEE 14-bus OPP and ANN results for various target precisions and different measurements accuracies

IEEE 14-bus OPP ($R_f$max 0.1 pu)				**ANN**		
TVE^V	TVE^I	# PMUs	Optimal observant sets (PMU locations)	Percentage estimation accuracy		
				l_f	D *(ave) (min)*	R_f *(ave) (min)*
$\boldsymbol{TP^D = 0.01, TP^{R_f} = 0.01,}$ Total generated faults: 22000						
10^{-2}	10^{-2}	7	**(2,5,7,9,12,13,14)**-(2,5,8,9,12,13,14)-(2,6,7,9,12,13,14)-(2,6,8,9,12,13,14)-(2,7,9,11,12,13,14)-(2,8,9,11,12,13,14)	99.6	99.9 96.1	100 100
10^{-3}	10^{-2}	3	**(2,6,9)**-(2,9,12)-(2,9,13)	99.5	99.9 99.1	99.9 99.1
10^{-3}	10^{-3}	1	**5**	98.2	99.9 99.5	100 100
$\boldsymbol{TP^D = 0.05, TP^{R_f} = 0.05,}$ Total generated faults: 1200						
10^{-2}	10^{-2}	2	**(2,6)**-(2,12)-(2,13) (5,6)-(5,12)-(5,13)	96.7	100 100	100 100
10^{-3}	10^{-2}	2	(1,6)-**(2,6)**-(2,10)-(2,11)-(2,12)-(2,13)-(2,14)-(5,6)-(5,10)-(5,11)-(5,12)-(5,13)-(5,14)	96.3	100 100	100 100
10^{-3}	10^{-3}	1	1-2-3-**4**-5	97.1	100 100	100 100

Table 2.3: IEEE 30-bus OPP and ANN results for various target precisions and different measurements accuracies

IEEE 30-bus OPP ($R_f$max 0.1 pu)				**ANN**		
TVE^V	TVE^I	# PMUs	Optimal observant sets (PMU locations)	Percentage estimation accuracy		
				l_f	D *(ave) (min)*	R_f *(ave) (min)*
$\boldsymbol{TP^D = 0.01, TP^{R_f} = 0.01,}$ Total generated faults: 45000						
10^{-2}	10^{-2}	13	**(2,4,6,10,12,15,19,22,25,26,27,29,30)**-(1,5,6,9,12,15,19,21,25, 26,27,29, 30)-And 52 more.	99.1	99.7 96.8	99.9 99.5
10^{-3}	10^{-2}	8	(1,5,6,12,15,18,22,29)-**(2,4,6,12,15,18,22,29)**-And 302 more.	98.9	99.9 97.7	100 100
10^{-3}	10^{-3}	2	**(6,12)**-(6,15)	96.1	97.7 83.3	100 100
$\boldsymbol{TP^D = 0.05, TP^{R_f} = 0.05,}$ Total generated faults: 2460						
10^{-2}	10^{-2}	4	(4,9,15,27)-**(4,10,12,27)**-(4,10,13,27)-(4,10,14,27)-(4,10,15,27)-(4,15,21,27)-(4,15,22,27)-(4,15,22,29)-(4,15,22,30)	97.0	97.7 83.3	99.8 91.7
10^{-3}	10^{-2}	3	(2,14,24)-(2,14,25)-**(2,15,27)**-And 30 more.	92.7	99.6 91.7	100 100
10^{-3}	10^{-3}	1	4-**6**-12-13	88.2	99.4 83.3	100 100

Table 2.4: Results for solving OPP by Integer Linear Programming (ILP) in similar test systems

	Reference [7]		**Reference [14]**	
Test System	# PMUs	# PMUs	# PMUs	PMU bus locations
IEEE 7-bus	5	5	n/a	n/a
IEEE 14-bus	8	8	8	(1,2,4,6,8,9,10,13)
IEEE 30-bus	17	17	17	(2,3,6,7,8,10,11,12,13,15,17,19,22,24,26,27,29)

1.10. Conclusion

A new algorithm has been introduced for power system optimal PMU location using sensitivity analysis where the fault location accuracy is specifically taken into account. With the proposed sensitivity analysis, appropriate indices are defined that can be used to qualify the measurements' locations in the network in detecting fault location and impedance. Also, multi estimation is introduced and checked in the proposed algorithm to guarantee a unique mapping between a PMU set and all faults of interest throughout the system. The proposed algorithm finds

the minimum number of PMUs required for system fault observability. By using the obtained optimal PMU sets, an artificial neural network fault locator is generated using artificial neural networks that map between the measurements of the optimal measurement set and the system faults.

1.11. References

[1] Phadke, A.G., "Synchronized phasor measurements in power systems," *Comp. App. in Pow., IEEE* , vol.6, no.2, pp.10-15, 1993.

[2] Baldwin, T.L.; Mili, L.; Boisen, M.B., Jr.; Adapa, R., "Power system observability with minimal phasor measurement placement," *Power Systems, IEEE Transactions on* , vol.8, no.2, pp.707-715, May 1993.

[3] Bei Xu; Abur, A., "Observability analysis and measurement placement for systems with PMUs," *Power Systems Conference and Exposition, 2004. IEEE PES* , vol., no., pp.943-946 vol.2, 10-13 Oct. 2004.

[4] Novosel, D.; Madani, V.; Bhargava, B.; Khoi Vu; Cole, J., "Dawn of the grid synchronization," *Power and Energy Magazine, IEEE* , vol.6, no.1, pp.49-60, January-February 2008.

[5] Albuquerque, R.J.; Paucar, V.L., "Evaluation of the PMUs Measurement Channels Availability for Observability Analysis," *Power Systems, IEEE Transactions on* , vol.28, no.3, pp.2536-2544, 2013.

[6] Quanyuan Jiang; Xingpeng Li; Bo Wang; Haijiao Wang, "PMU-Based Fault Location Using Voltage Measurements in Large Transmission Networks," *Power Delivery, IEEE Transactions on* , vol.27, no.3, pp.1644-1652, July 2012.

[7] Kavasseri, R.; Srinivasan, S.K., "Joint placement of phasor and conventional power flow measurements for fault observability of power systems," *Generation, Transmission & Distribution, IET* , vol.5, no.10, pp.1019-1024, October 2011.

[8] Aminifar, F.; Khodaei, A.; Fotuhi-Firuzabad, M.; Shahidehpour, M., "Contingency-Constrained PMU Placement in Power Networks," *Power Systems, IEEE Transactions on* , vol.25, no.1, pp.516-523, Feb. 2010.

[9] Bei Gou; Kavasseri, R. G., "Unified PMU Placement for Observability and Bad Data Detection in State Estimation," *Power Systems, IEEE Transactions on* , vol.29, no.6, pp.2573-2580, Nov. 2014.

[10] N. C. Koutsoukis, N. M. Manousakis, P. S. Georgilakis and G. N. Korres, "Numerical observability method for optimal phasor measurement units placement using recursive Tabu search method," in *IET Generation, Transmission & Distribution*, vol. 7, no. 4, pp. 347-356, April 2013.

[11] Bei Gou, "Generalized Integer Linear Programming Formulation for Optimal PMU Placement," *Power Systems, IEEE Transactions on* , vol.23, no.3, pp.1099-1104, Aug. 2008.

[12] Chakrabarti, S.; Kyriakides, E., "Optimal Placement of Phasor Measurement Units for Power System Observability," *Power Systems, IEEE Transactions on* , vol.23, no.3, pp.1433-1440, Aug. 2008.

[13] Manousakis, N.M.; Korres, G.N.; Georgilakis, P.S., "Taxonomy of PMU Placement Methodologies," *Power Systems, IEEE Transactions on* , vol.27, no.2, pp.1070-1077, May 2012.

[14] Geramian, S.S.; Abyane, H.A.; Mazlumi, K., "Determination of optimal PMU placement for fault location using genetic algorithm," *Harmonics and Quality of Power, 2008. ICHQP 2008. 13th International Conference on* , vol., no., pp.1-5, Sept. 28 2008-Oct. 1 2008.

[15] Pokharel, S.P.; Brahma, S., "Optimal PMU placement for fault location in a power system," *North American Power Symposium (NAPS), 2009* , vol., no., pp.1-5, 4-6 Oct. 2009.

[16] Kai-Ping Lien; Chih-Wen Liu; Chi-Shan Yu; Joe-Air Jiang, "Transmission network fault location observability with minimal PMU placement," *Power Delivery, IEEE Transactions on* , vol.21, no.3, pp.1128-1136, July 2006.

[17] M. Korkali and A. Abur, "Optimal Deployment of Wide-Area Synchronized Measurements for Fault-Location Observability," in *IEEE Transactions on Power Systems*, vol. 28, no. 1, pp. 482-489, Feb. 2013.

[18] M. Korkalı and A. Abur, "Robust Fault Location Using Least-Absolute-Value Estimator," in *IEEE Transactions on Power Systems*, vol. 28, no. 4, pp. 4384-4392, Nov. 2013.

[19] J. J. Grainger, W. D. Stevenson, Power System Analysis, New York: McGraw-Hill, Inc., International Editions 1994, pp. 283-467.

[20] IEEE Standard Requirements for Instrument Transformers," *IEEE Std C57.13-2008 (Revision of IEEE Std C57.13-1993)* , vol., no., pp.c1,82, July 2008.

[21] "Instrument Transformer Technical Information and Application Guide", ABB brochure, Doc No. 1VAP420003-TG, Jan. 2005. [Online]. Available: http://www.abb.com/abblibrary/downloadcenter/?View=Result.

[22] Mai, R.K.; He, Z.Y.; Ling Fu; Kirby, B.; Zhiq Qian Bo, "A Dynamic Synchrophasor Estimation Algorithm for Online Application," *Power Delivery, IEEE Transactions on* , vol.25, no.2, pp.570-578, April 2010.

[23] Rabe, S.; Komarnicki, P.; Styczynski, Z.A.; Gurbiel, M.; Blumschein, J.; Kereit, M.; Voropai, N., "Automated test procedures for accuracy verification of Phasor Measurement Units," *Power and Energy Society General Meeting, 2012 IEEE* , vol., no., pp.1-6, 22-26 July 2012.

[24] Rao, J.G.; Pradhan, A.K., "Accurate Phasor Estimation During Power Swing," in *Power Delivery, IEEE Transactions on* , vol.PP, no.99, pp.1-1.

[25] Barchi, G.; Macii, D.; Petri, D., "Synchrophasor Estimators Accuracy: A Comparative Analysis," *Inst.and Meas., IEEE Trans. on* , vol.62, no.5, pp.963-973, May 2013.

[26] Watson, N.; Arrillaga, J.; "Power Systems Electromagnetic Transient Simulation", IET Power and Energy Series 39.

[27] Salim, R.H.; de Oliveira, K.; Filomena, A.D.; Resener, M.; Bretas, A.S., "Hybrid Fault Diagnosis Scheme Implementation for Power Distribution Systems Automation," in *Power Delivery, IEEE Transactions on* , vol.23, no.4, pp.1846-1856, Oct. 2008.

[28] Nazaripouya, H.; Mehraeen, S., "Optimal PMU placement for fault observability in distributed power system by using simultaneous voltage and current measurements," *Power and Energy Society General Meeting (PES), 2013 IEEE* , vol., no., pp.1-6, 21-25 July 2013.

[29] R. Christie *Power* System *Test Archive,,* 1999. [online] Available: http://www.ee.washington.edu/research/pstca.

Chapter 3
Overhead Radial Distribution Networks

1.12. Introduction

Distribution networks are parts of the power systems where there is significant demand for DERs integration in both bulk and small sizes. Distribution networks can be in radial and mesh structures. An overhead radial distribution network is modelled in this chapter to investigate DERs integration effects from various aspects and results are also provided. Various standards are considered to evaluate the effects and their severity. In the studies conducted here PVs are placed in the modelled networks. This is due to the high demand for PV integration in distribution networks to match with industry needs. Also, a PV unit is a good example for modelling proposes to simulate energy source intermittency and investigate its impact on network operation. However, similar results can be deduced by considering other forms of DGs integrated in such networks with considering some modifications.

1.13. 13-Bus network

In order to investigate the impacts of DG integration into the power networks, an accurate test system is necessary. This study uses a 13-bus overhead distribution model. Integrating renewable energy based DGs are popular for distribution network customers as a method to reduce their electric expenses. Figure 3.1 depicts the modelled network with 13 buses.

This network is connected to the utility grid through bus 1 by a substation feeder. Solid lines represent three phase feeders and dashed lines are used for single phase branches. The total amount of the network load is 37,429 kW active power and 17,012 kVar reactive power that is located at the grid buses. Base voltage and power are chosen to be 24 kV and 5 MVA, respectively, resulting

in 7.4858 p.u active power and 3.4024 p.u reactive power. As shown in Figure 1, a reactive power compensator is installed at bus 2 with 1,800 kVar rating that can be connected to the network in the case of low voltage. The network consists of 12 lines.

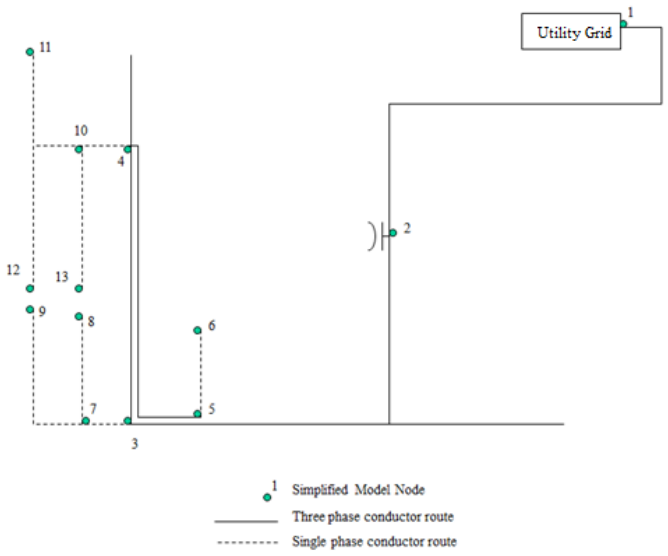

Figure 3.1: The modelled overhead distribution network

The network has a 23 kV voltage level in the 3-phase feeders and a 13.2 kV level in the single-phase braches. Three simulation environments are considered to reach an accurate model for the network. These environments are:

- Newton Raphson load flow using MATLAB Code
- Time domain simulations using MATLAB/Simulink Toolbox
- ETAP

These models are used to investigate various aspects of PV DG integration into the network as will be presented in the next sections in more detail. The studies include radiation change effect, voltage level, voltage flicker, utility grid connection power-flow, harmonic analysis, and fault analysis. Different scenarios have been considered for each study in order to reach a reliable conclusion about the integration effects, their severity and compatibility with related standards. Some of these scenarios include the capacitor bank's effect, min and max load impact, daily load

change, daily sun radiation change and cloud impacts. For all of the cases, a recommended maximum PV DG penetration level is determined in order to satisfy the standards.

1.14. Network's Voltages

One of the goals in operation of the power grids is to maintain the voltages at acceptable levels. Capacitor bank installation is the most popular compensation method for this purpose. Here, a capacitor bank is installed on bus 2 as a means of compensation for voltage level and reactive power support. DGs integration in the network can improve the network voltage profile. However, any interruption in the DGs contribution, particularly when it affects a large number of them, results in voltage fluctuations, sag, and possible flickers.

PV DGs utilized in the grid depend on solar radiation. Solar radiation changes over the 24-hour periods. IEEE 1453, which also covers IEC 61000, and IEEE 519 definitions and limitations for voltage quality are considered and discussed in this section. In addition, the varying solar radiation due to passing a scattered cloud over the network area is investigated here. The solar radiation scenarios studied are listed below:

1. Daily change in solar radiation
2. Small cloud effect
3. Large cloud effect

1.15. Solar Radiation Change

Figure 3.2 depicts the change in solar radiation during 24 hours. This solar radiation shows the PV power generation changing from zero during the night time to 100% of the grid's full load at 11:00am and to the maximum power generation (150% of the full load) at 1:00pm. PV's maximum penetration capacity at each bus is equal to 150% of the full load installed at that bus.

Thus, the maximum PV DG penetration is 150% of the network's total load. This assumption is adopted in this chapter unless otherwise mentioned.

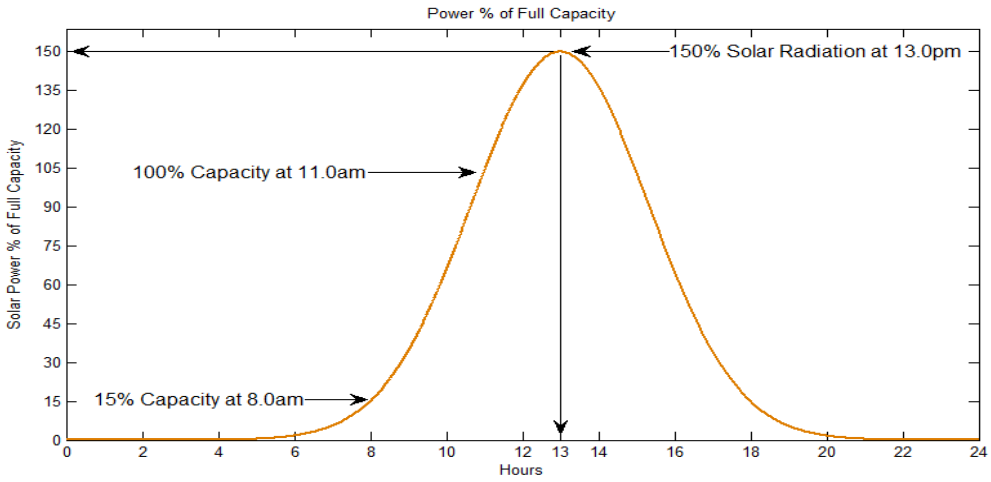

Figure 3.2: Daily solar radiation intensity

Figures 3.3 and 3.4 depict the bus voltage changes in a 24-hour period for the case without the capacitor bank. Figure 3.4 plots the voltage profile for the case with full load in the network and it shows a 4.73% voltage change in the downstream buses over a 24 hour period. Similarly, Figure 3.4 illustrates an overall change equal to 4.36% in the voltage profiles when the grid's load is 16% of the full load. In this case, the voltage overshoots at 1:00pm when the PV generation is at maximum due to high solar radiation. This undesirable voltage change results from variations in the solar radiation from night to noon. Here, V1 remains at 1.0 p.u as it is connected to the substation feeder whereas other bus voltages are susceptible to to change as solar radiation changes throughout the day.

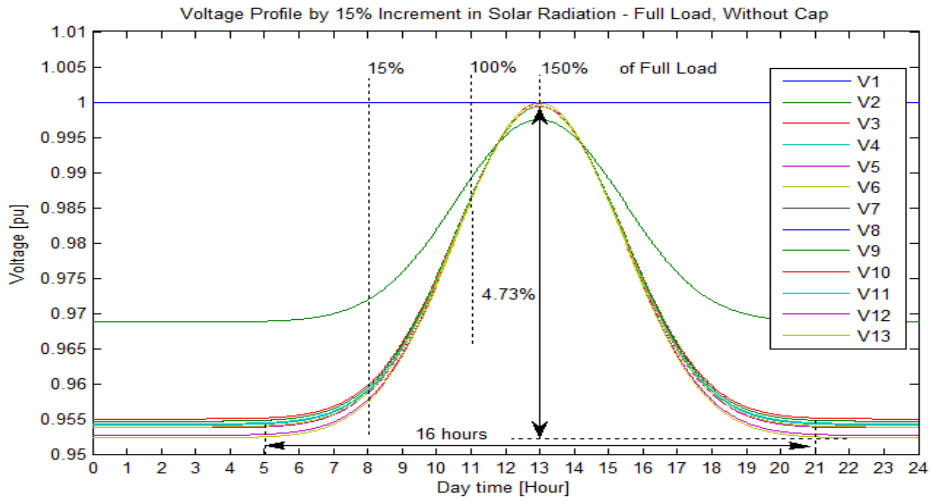

Figure 3.3: Daily voltage variations at full load without CAP

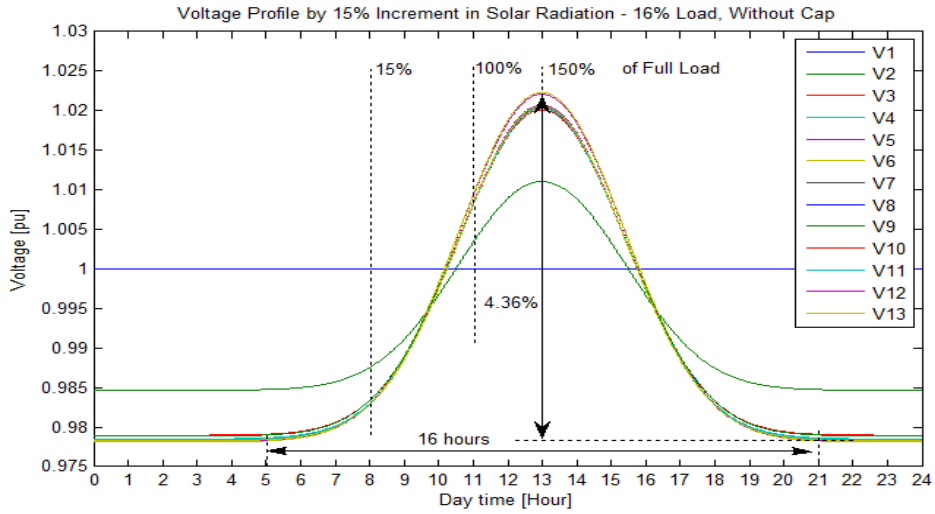

Figure 3.4: Daily voltage variations at 16% load without CAP

1.16. Cloud Effects

Another contributing factor to the voltage variations in grid with PV DGs is the clouds that affect the PV's performance resulting in voltage fluctuations and flicker. Various types of moving clouds are investigated here. The difference between a small cloud and a large cloud is that a small moving cloud affects one small section (zone) at a time while a large moving cloud gradually covers the entire network before it leaves the network. Here the cloud speed is considered as 0.1 mile/min from zone A toward zone C as shown in Figure 8 and the drop in the solar radiation due

to the cloud is 80%. In this study it is assumed that solar output power is proportional to the solar radiation. Also, the cloud effect is considered in the following 4 times of the day:

- 8.00 am (normal solar radiation is 15% of full load)
- 9:30 am (normal solar radiation is 48.54% of full load)
- 1:00 pm (normal solar radiation is 150% of full load)
- 3:00 pm (normal solar radiation is 103.77% of full load)

The network is investigated in various cases for both small, scattered, and large cloud scenarios. These cases are combinations of minimum and full loads (16% and 100% of the full load) without the capacitor bank (worst case). The network is split into 4 zones in order to investigate the clouds' effects. These zones are depicted in Figure 3.5. It should be mentioned that zone 1 has a negligible effect on the voltage variations since it is connected to the substation with a fixed voltage.

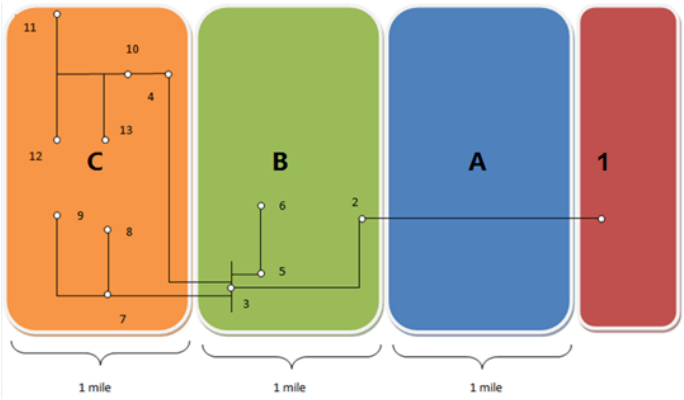

Figure 3.5: Overhead 13-Bus network zones for cloud analysis

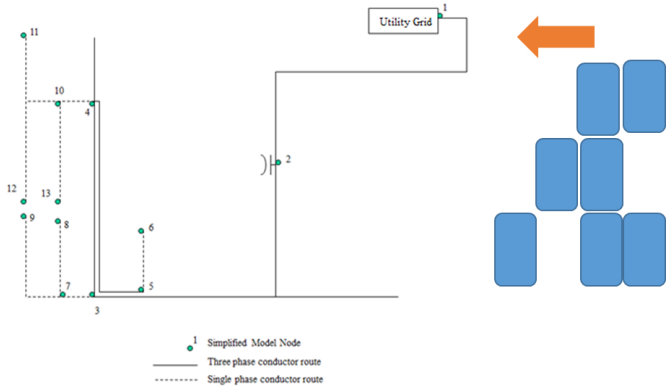

Figure 3.6: Overhead 13-Bus network and random scattered cloud example

In order to investigate the cloud effects, particularly the voltage flicker, relevant standards are considered. In general, the voltage changes fall into two categories; short term and long term voltage variations. IEEE 1453 and IEC 61000 standards have different definitions for voltage flicker severity evaluation based on the disturbance duration and period.

IEEE 519 has an empirical study curve made by the General Electric Company for evaluating voltage flicker severity. It should be mentioned that companies such as Kansas City Power & Light Company, West Pennsylvania Power Company, Detroit Edison Company, and some others have their own empirical curves, but the GE curve is more popular and well-known. The GE curve adopted by IEEE 519 is presented in Figure 9 and evaluates the flicker based on the frequency of voltage change in certain periods as shown on the horizontal axis. The curve classifies flicker into visible and irritative categories.

Note that there are three effective zones when cloud effects are studied. The small cloud is assumed to last for 30 minutes (based on cloud speed and zone length) over each zone. Thus, voltage fluctuation occurs three times per hour. By taking the curve of Figure 3.7 into account, flicker limits can be considered as:

- Voltage Flicker Visibility Limit: $\Delta V < 1\%$
- Voltage Flicker Irritation Limit: $\Delta V < 3.5\%$

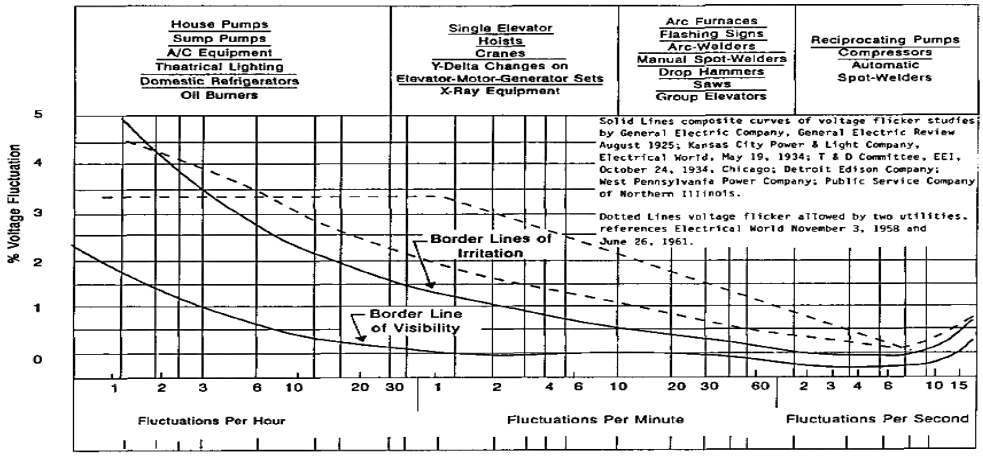

Figure 3.7: Voltage Flicker tolerance curve from IEEE 519 based on GE data

1.16.1.Small Cloud

Figure 3.8 presents the voltage flicker caused by small clouds passing over the network in four different hours when minimum load (16% of the full load) is considered in the system. Although all the bus voltages are affected by the cloud simultaneously, their variations are slightly different. According to the figure, the most severe voltage flicker happens during the maximum solar radiation at 1:00pm that is around 2.8%. In the case with the full load, the voltage flicker has a greater magnitude (3%) as depicted in Figure 3.9 at the same hours of day. Both of the presented cases are without the capacitor bank connected to the network. From the GE curve of Figure 3.8, these flicker levels are within the visible boundaries, but do not reach the irritative flicker limits.

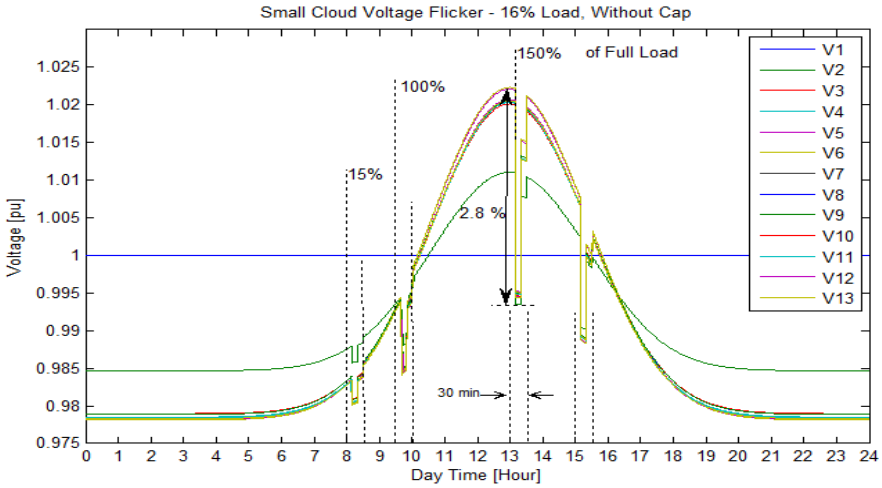

Figure 3.8: Voltage Flicker resulted by small cloud at16% load without Cap

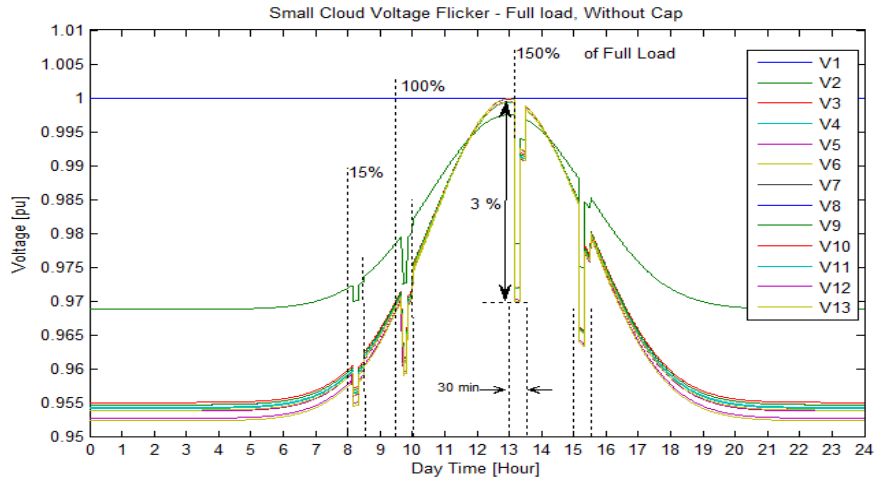

Figure 3.9: Voltage Flicker resulted by small cloud at Full load without Cap

Figure 3.10 depicts the effect of a small moving cloud with full load and the capacitor bank available in the network. By comparing Figures 3.9 and 3.10, the permanently connected capacitor does not impact the voltage flicker significantly. That is, voltage maximum voltage drop remains at 3%. However, with a smart automatic connecting capacitor bank, the minimum voltage during the night time can be raised with the capacitor's reactive power injection. Also, the capacitors should be disconnected during the high solar radiation close to the noon time to avoid boosting the voltage flicker. However, as mentioned before, this approach may not be cost-effective.

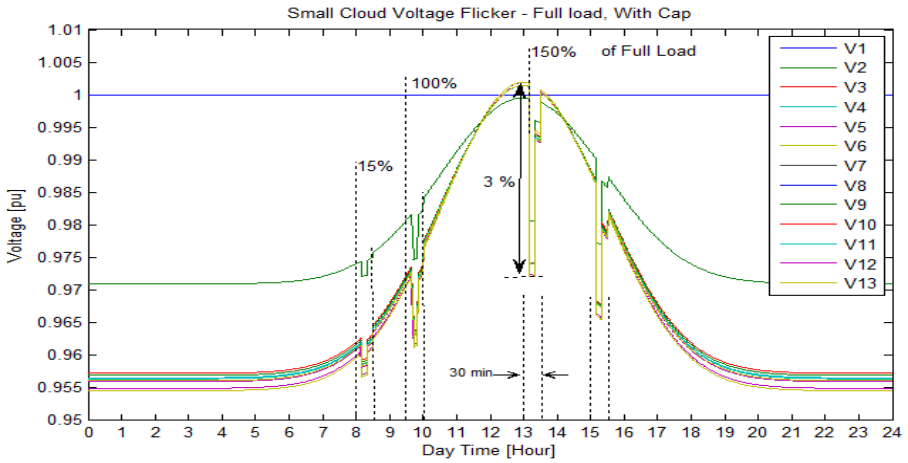

Figure 3.10: Voltage Flicker resulted by small cloud at Full load with Cap connected

1.16.2.Scattered Cloud

Figure 3.11 presents the voltage flicker caused by the scattered clouds passing over the network in the mentioned four different hours when minimum load (16% of the full load) is considered in the grid. According to the figure, the most severe voltage flicker happens during the maximum solar radiation at 1:00pm that is around 4%. In the case with the full load, the voltage flicker has the same magnitude (4.3%) as depicted in Figure 3.12 during the same hours of day. Both of the presented cases are without the capacitor bank connected to the network. From the GE curve of Figure 3.7, these flicker levels are within the visible boundaries, and reach the irritative flicker limits.

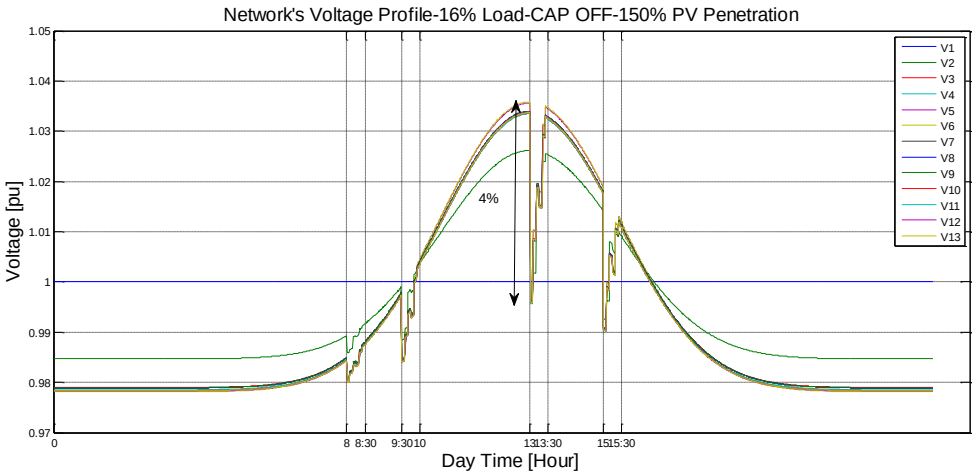

Figure 3.11: Voltage Flicker resulted by scattered cloud at 16% load without Cap

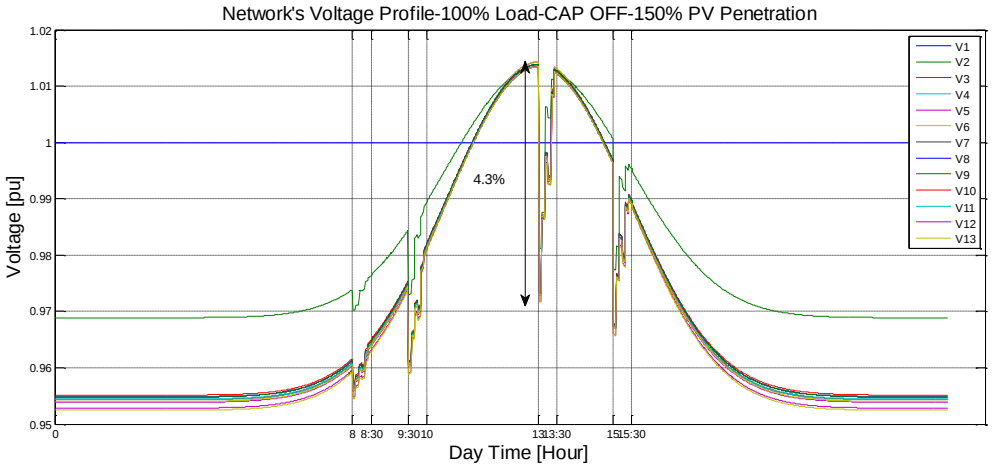

Figure 3.12: Voltage Flicker resulted by scattered cloud at full load without Cap

Figures 3.13 and 3.14 depict the effect of the scattered moving cloud with 16% load and full load in the presence of the capacitor bank available in the network. By comparing the figures, it can be concluded that the permanently connected capacitor does not improve the voltage flicker; that is, the maximum voltage drop remains the same. However, with a smart automatic connecting capacitor bank, the minimum voltage during low solar radiation times can be raised with the capacitor reactive power injection. Also, the capacitors should be disconnected during the high solar radiation times (close to the noon time) to avoid excessive increase in the voltage flicker.

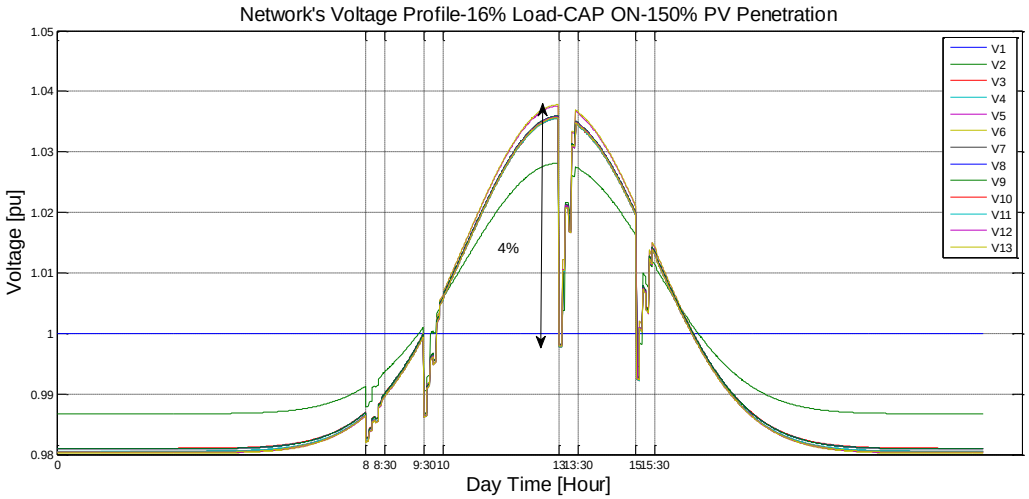

Figure 3.13: Voltage Flicker resulted by scattered cloud at 16% load with Cap connected

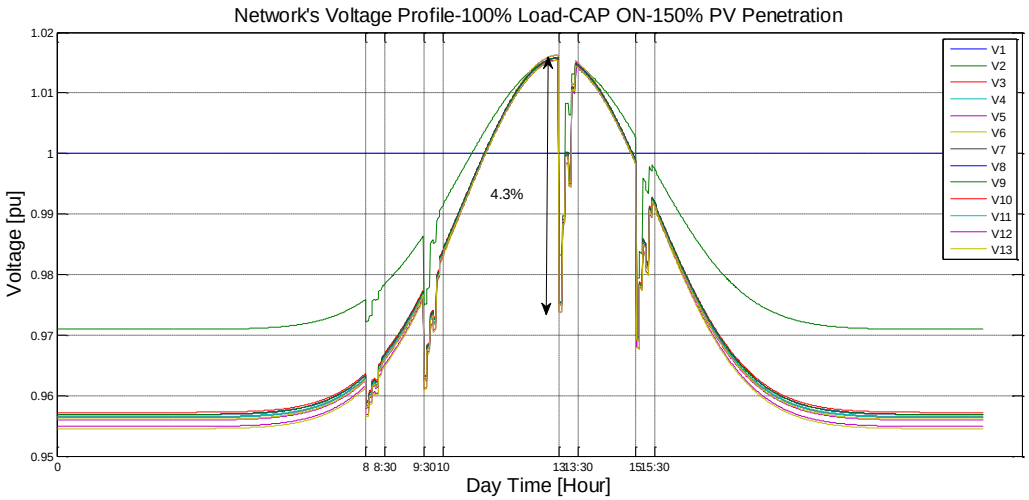

Figure 3.14: Voltage Flicker resulted by scattered cloud at full load with Cap connected

1.16.3.Large Cloud

As mentioned before, when studying large cloud effects, similar assumptions to the small cloud scenarios are considered with the exception that the area that the large cloud covers is the entire network. The large cloud starts covering the network with the same speed and manages to cover network zones one-by-one until it finally covers the entire network. Therefore, it is expected that a large moving cloud will result in a higher voltage flicker. Figures 3.15 and 3.16 illustrate the voltage flicker with 16% and 100% of full load available in the network, respectively, without the capacitor bank. According to the figures, the voltage flicker is increased to 3.5% and 3.7% for 16%

and full loads respectively at 1:00pm. Voltage flicker at minimum and full loads are within the range of irritative flicker according to IEEE 519. Here, it is considered that the cloud causes a drop in each zone as it starts to cover it; thus, one observes a frequency of 3 in the voltage variation while different bus voltages experience different variations. Similarly, Figure 3.17 depicts the case with full load and a capacitor bank connected to the network. Thus, a constantly connected capacitor bank does not improve voltage flicker in the presence of PV sources and an automatic capacitor bank with a relatively larger MVAR rating is required. However, the new equipment cost effectiveness must be taken into account.

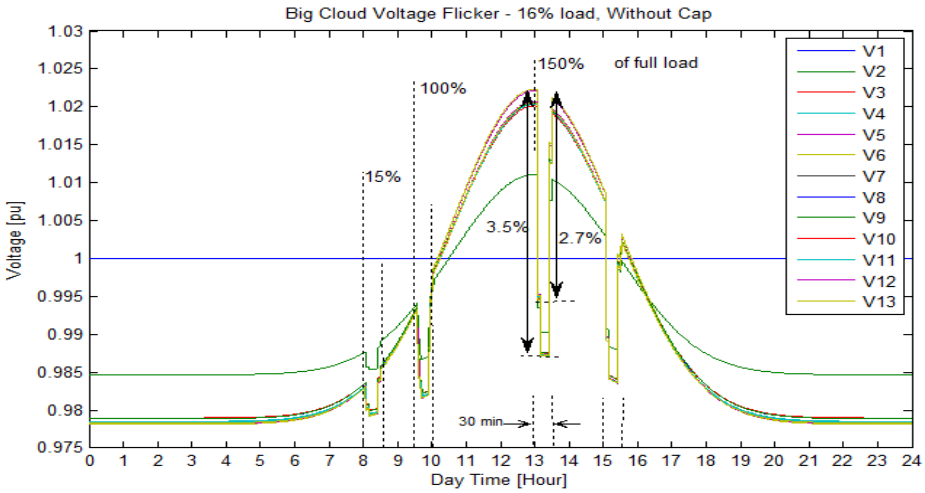

Figure 3.15: Voltage Flicker caused by a large cloud at 16% load without Cap

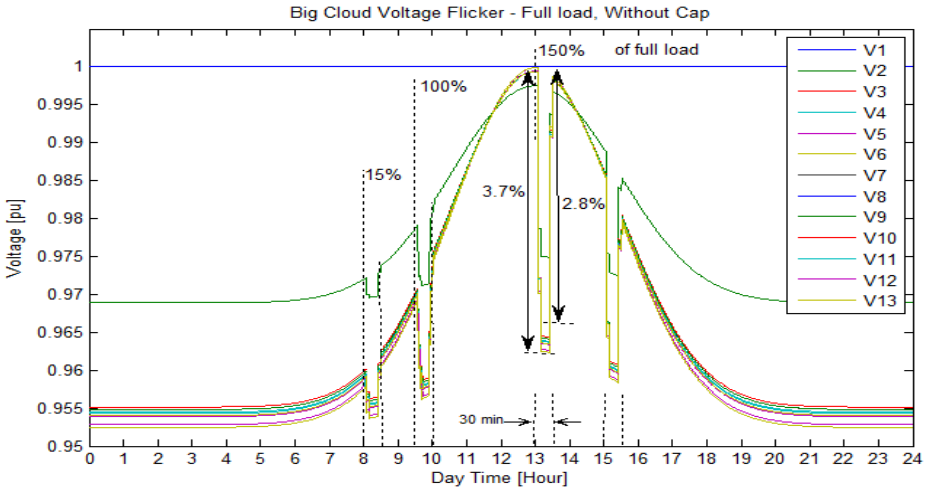

Figure 3.16: Voltage Flicker caused by a large cloud at Full load without Cap

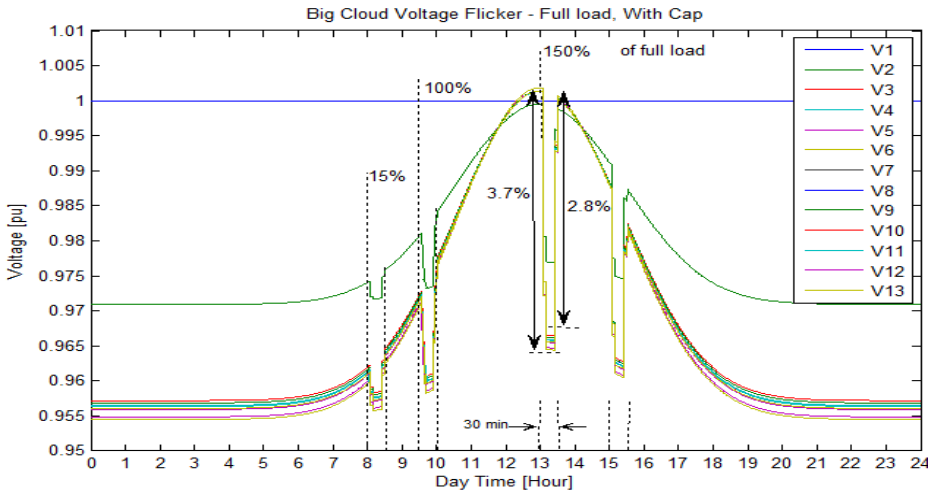

Figure 3.17: Voltage Flicker caused by a large cloud at Full load with Cap

Comparing the results from the flicker study reveals that the worst flicker occurs when full load is available and the network is exposed to a large cloud leading to 3.7% voltage flicker. Thus, several PV penetration levels are investigated to find a satisfactory penetration level that meets the standard's limit of 1% for visible flicker. Figure 3.18 depicts the case with full load and a large cloud covering the network with a 30% (of the full load) PV penetration level. The voltage flicker in this case is equal to 1% at 1:00pm. Each grid bus in this case has a maximum PV generation capacity (occurring at 1:00pm) of 30% of the bus full load.

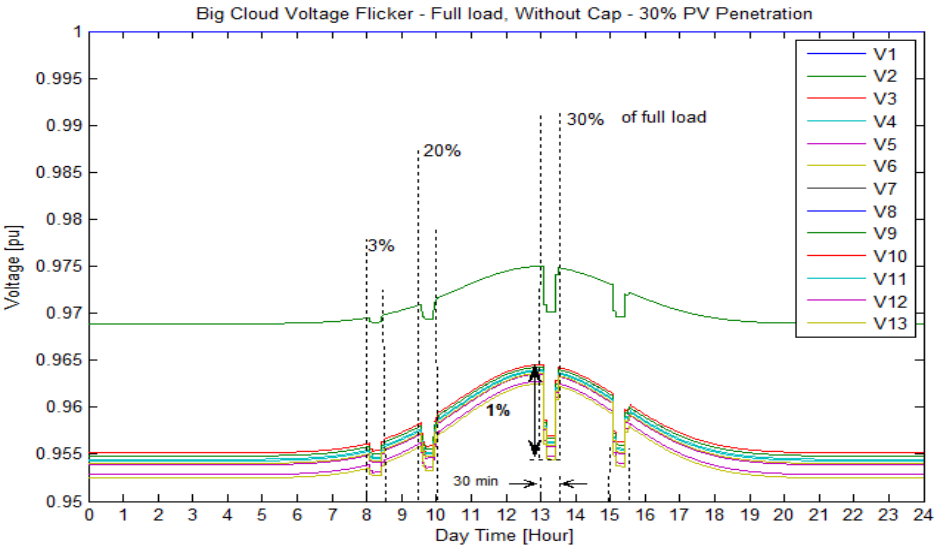

Figure 3.18: Maximum PV penetration to meet the standard's flicker limit

1.17. Reactive Power Compensation

Reactive power compensation is an important and usually necessary approach for power networks especially those with PV integration. Both connected and islanded modes are simulated here. Two scenarios are considered for islanded mode operation:

1. PV active power > Full load + Losses : Abundant PV active Power

The PV total active power generation is more than the network's demand (i.e., the loads consumptions and power losses)

2. PV active power < Full load + Losses : Shortage in PV active Power

The PV total active power generation is less than the network consumption. These situations are summarized below:

1.17.1.Scenario 1: Connected Mode

For proper compensation, a capacitor bank has been installed on bus 3 with size roughly 4 times bigger than original system CAP, i.e. 1.4 p.u. The capacitor compensation results in a voltage shift in all buses which may lead into excessive voltage at noon time due to PV power. An automatically tapped capacitor compensation has been evaluated which results in less over voltage during 24 hours. Figures 3.19 and 3.20 represent the voltage profiles for the cases with 100% load in the network without and with the CAP, respectively. Installing a permanently fully connected 1.4 p.u. capacitor on bus 3 results in a noticeable shift in voltage profile.

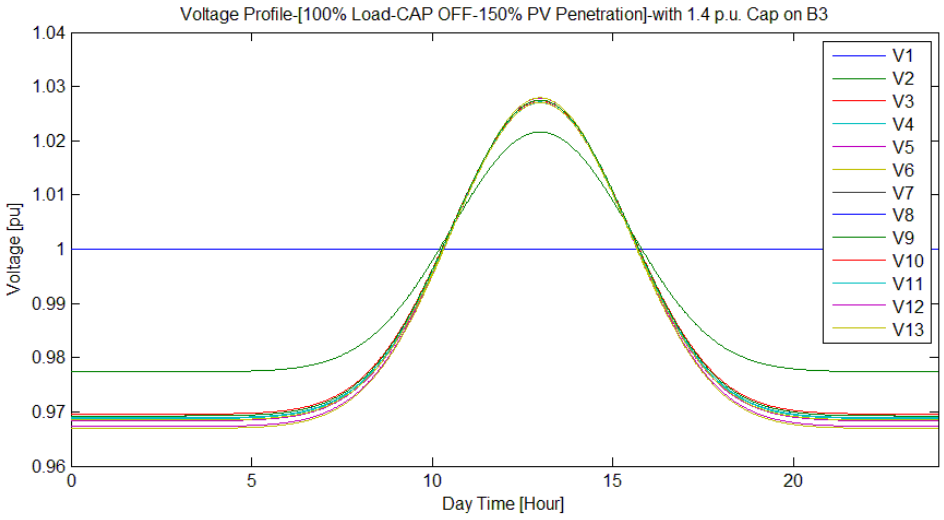

Figure 3.18: Network voltage profile with the capacitor on bus 3 and without the original system CAP

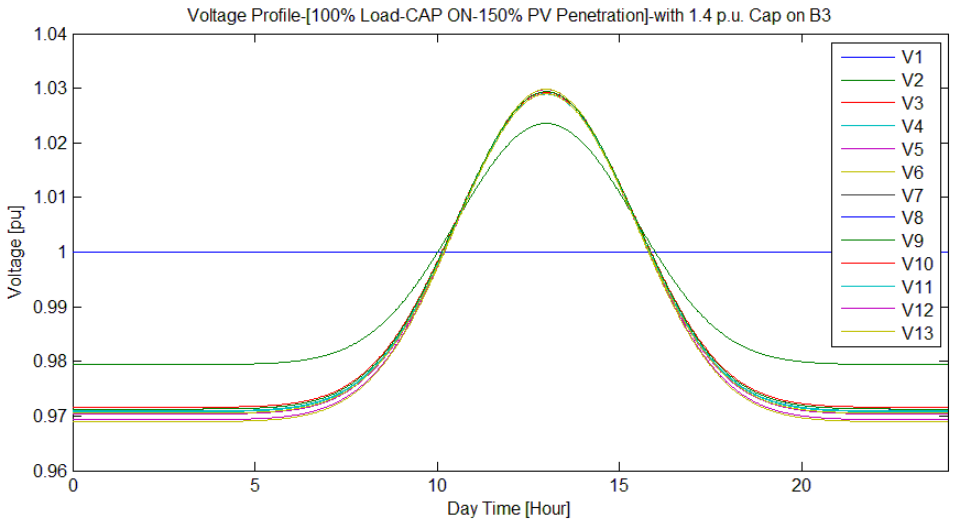

Figure 3.19: Network voltage profile with the capacitor on bus 3 with original system CAP

Next, an automatically tapped capacitor has been used. The capacitor has 6 taps that are spread to accommodate the minimum and maximum voltage conditions (0.956 and 1.014 according to Figures 3.18 and 3.19) Automatic tapped capacitor results in less over voltage around noon time (maximum PV penetration due to sun radiation) and more voltage improvement during dark hours as depicted in Figures 3.20 and 3.21.

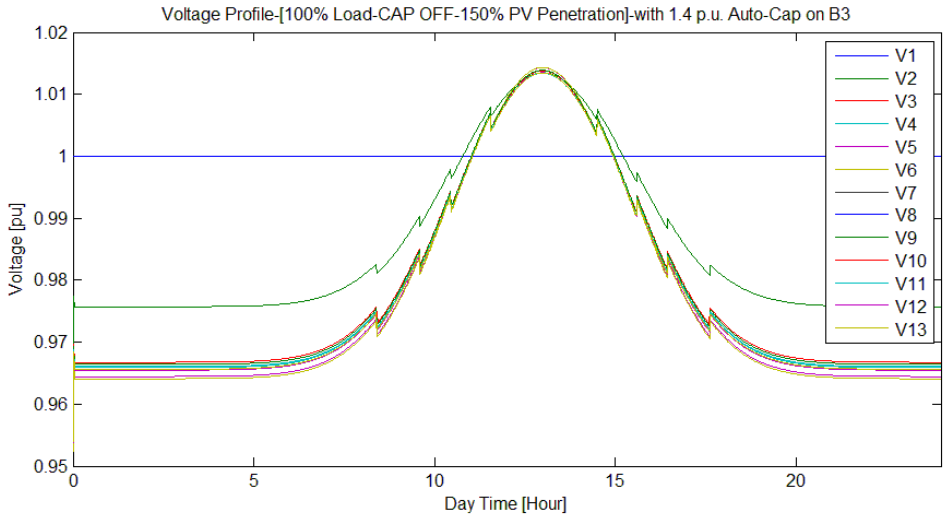

Figure 3.20: Network voltage profile with the tapped capacitor on bus 3 without original system CAP

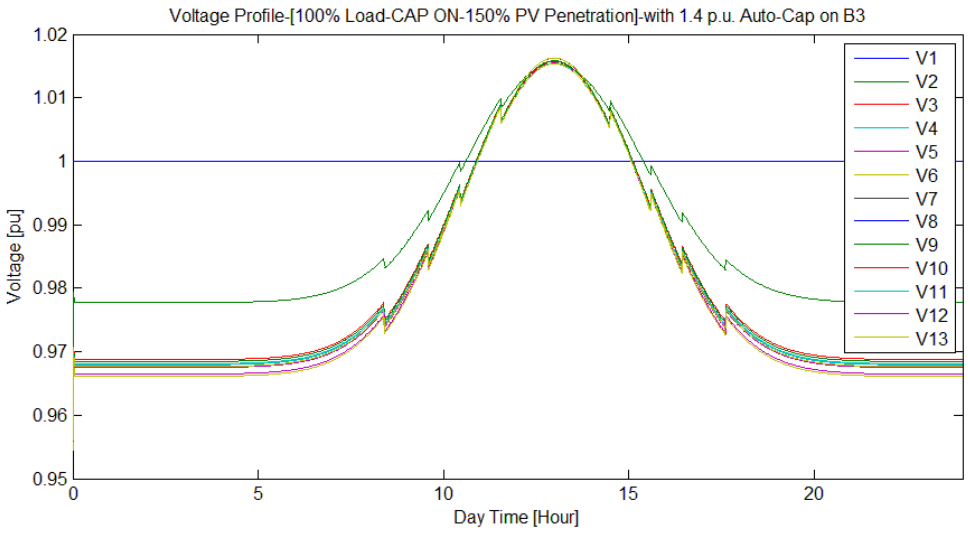

Figure 3.21: Network voltage profile with the tapped capacitor on bus 3 with original system CAP

1.17.2.Scenario 2: Islanded Mode

In this scenario four tapped capacitors are installed with 10 taps each on high load buses with the following specifications:

- Bus 1, Capacity of: 6.1 MVAR (CAP ON), 7.8 MVAR (Cap OFF),
- Bus 2, Capacity of: 4.8 MVAR (Cap ON), 6.6 MVAR (Cap OFF),
- Bus 3, Capacity of: 1.7 MVAR (Cap ON), 1.74 MVAR (Cap OFF),
- Bus 5, Capacity of: 1.7 MVAR (Cap ON), 1.74MVAR (Cap OFF),
- Total capacity 14.3 MVAR (2.6 pu) in with Cap ON, and
- Total capacity 17.2 MVAR (3.4 pu) in with Cap OFF.

When CAP is OFF in Scenario 2, with all the tapped capacitors in place the voltages are shown to be satisfactory as depicted in Figures 3.22 and 3.23 The PV power starts from zero in the beginning of the day and reaches its peak at around 1:00pm followed by a decrease in the afternoon hours. By changing the value of the capacitor on each bus by means of the tap, the voltage profile can be adjusted and the voltage fluctuation be reduced as shown in the figures. However, around noon time during the maximum solar radiation, the tap is set on the minimum level but some increase in the voltage is inevitable. By magnifying the bus 3 voltage waveform in Figure 3.23, it

is shown that approach is effective in maintaining the voltage around nominal values by changing the capacitors taps.

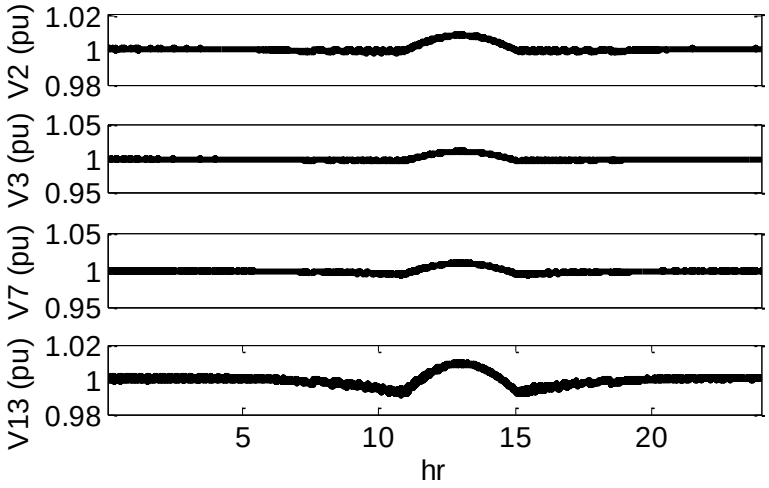

Figure 3.22: Network voltage profile using multiple tapped capacitors with CAP OFF

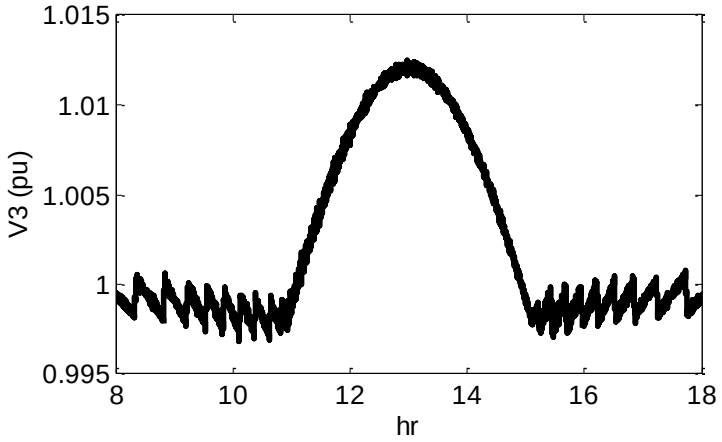

Figure 3.23: Bus 3 zoomed voltage in the second scenario with CAP OFF

When PV < Full load + Losses automatic load shedding is applied at all loads. For PV > Full load + Losses, automatic PV power control on bus 1 is applied to reduce the PV generated power. As shown in the figures, PV power is low, the consumption is limited by the PV generation. Once the PV reaches the demanded load, active and reactive power consumption will be constant values (nominal loads on the buses) as illustrated in Figure3.24 However, there is surplus power produced by the PV units. In order to balance the grid power, generation on bus 1 will be decreased as shown

in Figure 3.25 Load reactive power is proportional to the load active power at all times. The load demanded reactive power is then provided by adjusting the tap level of the capacitors as shown in Figure 3.26.

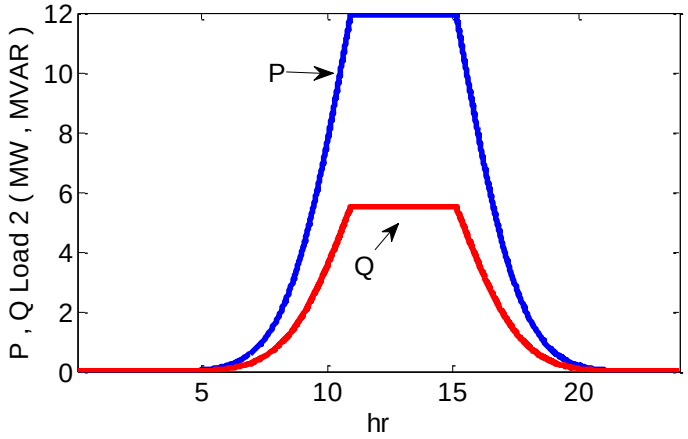

Figure 3.24: Active and reactive power consumption on bus 2 in the second scenario with CAP OFF

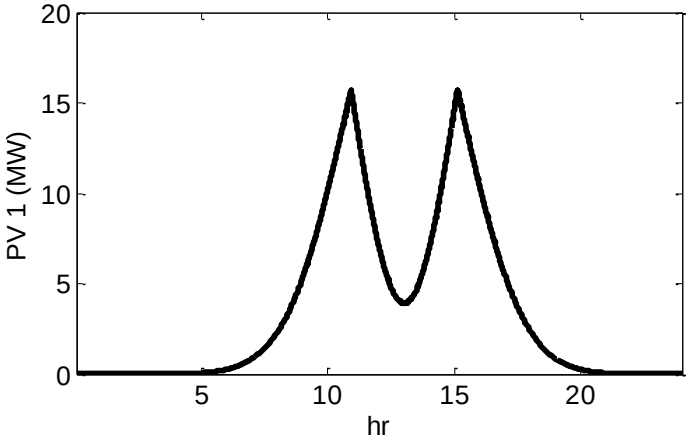

Figure 3.25: Active power generation on bus 1 the second scenario with CAP OFF

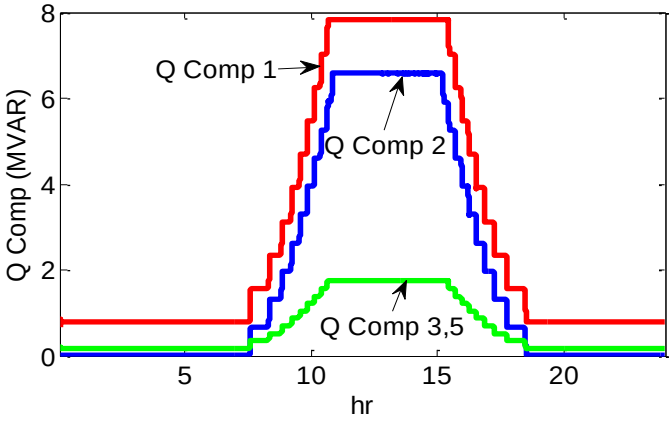

Figure 3.26: Reactive power consumption in the system the second scenario with CAP OFF

1.18. Fault Current Level

DGs integration may have critical influences on fault situations and the protection system. IEEE standards mention that inverter interfaced DGs should have a limited fault current to be no more than twice that of their normal current for limited duration for protecting their switching devices. However, this amount of current can affect the fault current magnitude in the network. This change in fault current characteristics may have significant effects on the protection system such as delayed trip, miscoordination, or blinding.

A fault study has been performed here by simulating a fault in highly loaded buses of the network with a focus on the utility grid protection system. That is, buses 2,3,5,7, and 10 are analyzed for fault scenarios in cases with full load and 16% of the load. It is assumed that the pickup settings for the utility grid relays are twice their normal currents during the full load working condition, (i.e., two times 7.77 p.u or 15.54 p.u.). Faults are simulated as high power loads (high impedance faults.)

Figure 3.27 depicts the utility grid and the sum of the PV DG contribution in a 3-phase fault at bus 2 with full load available in the network. The time axis indicates the hour in which the fault occurs. As shown in Figure 3.27, when the fault happens at night i.e., zero PVs contribution, all the fault current (approximately equal to 24.5 p.u) is injected by the utility grid. This current is more than the utility grid's protection threshold and is easy to detect. However, when the PV penetration exceeds 124% (of the full load, based on sun radiation) the utility grid contribution to the fault current will be less than its protection threshold as shown in the figure. The PV contribution to the fault current significantly reduces the utility grid's contribution. Such a fault, in this case, cannot be diagnosed and tripped by the utility grid's protective system (blinding phenomenon.)

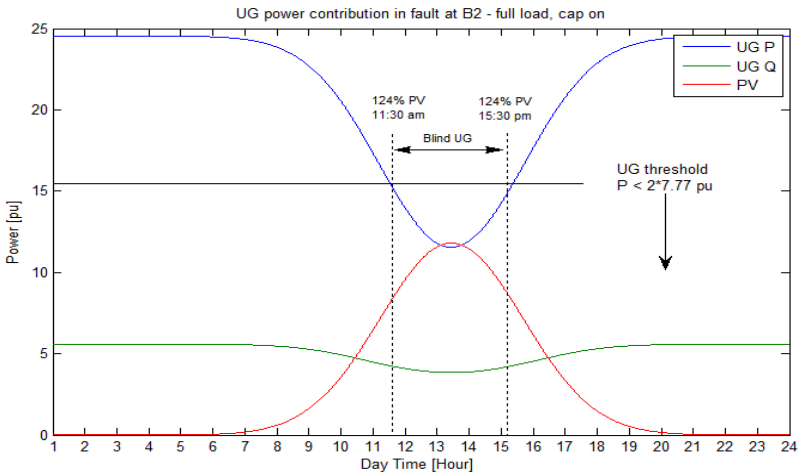

Figure 3.27: Sources contribution in fault at bus 2 with full load

Figure 3.28 presents a fault at bus 5. By increasing the distance from the utility grid connection, i.e., increasing the impedance the utility grid observes during the fault, the fault current level and the utility grid share will be reduced.

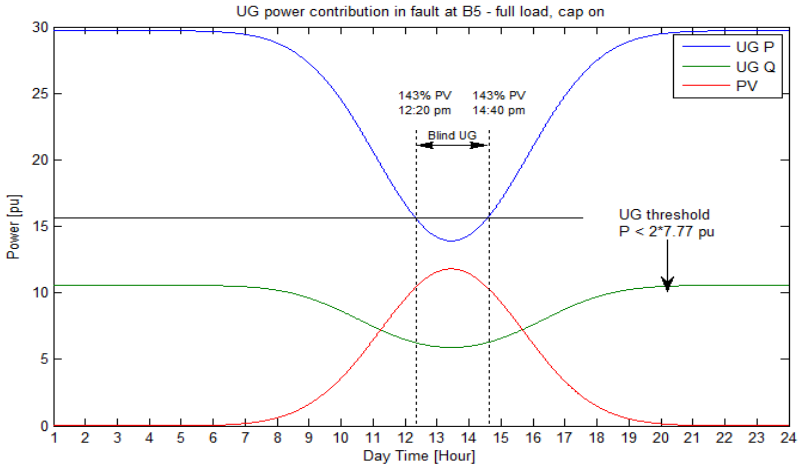

Figure 3.28: Sources contribution in fault at bus 5 with full load

Figure 3.29 presents the case with 16% load available in the network. As discussed in the previous section, this case results in reverse power flow at the utility grid connection. Figure 3.29 shows that just reaching 72% of PV generation capacity is enough to enter the blinding zone in which case the fault at bus 2 cannot be diagnosed and tripped. Figure 3.30 presents the case with

the fault occurring at bus 5 with the same trend. Comparing Figures 3.30 and 3.27 gives a better idea of the blinding phenomenon deterioration caused by a decrease in the network's load.

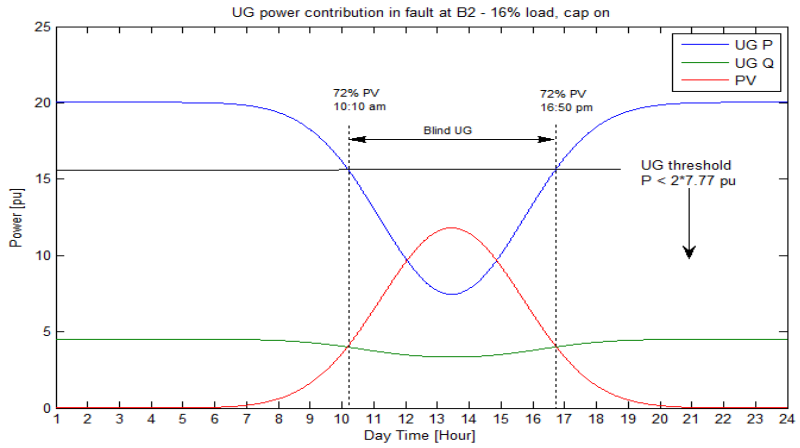

Figure 3.29: Sources contribution in fault at bus 1 with 16% load

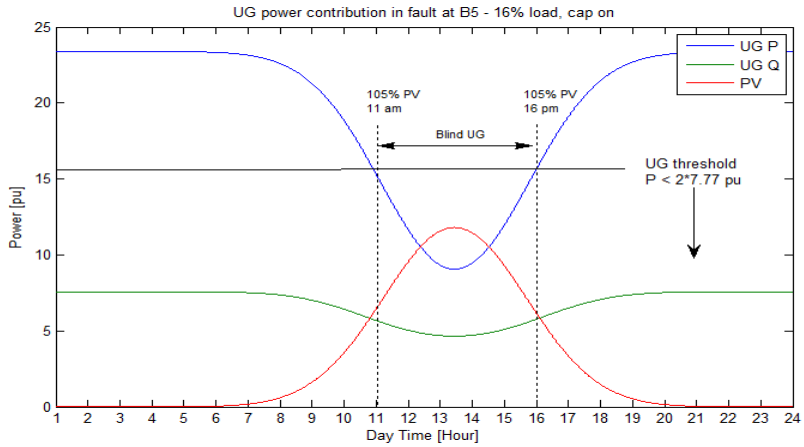

Figure 3.30: Sources contribution in fault at bus 5 with 16% load

By investigating different buses, the highest fault current is identified to occur at bus 2 with 16% load due to its low short-circuit impedance. Figures 3.31 and 3.32 show that by setting the PV penetration to 53% (of full load at 1:00pm), the utility grid's contribution to the fault current is more than the defined threshold resulting in detecting the fault. Trends in other buses' faults such as that of bus 5 shown in Figure 3.32, show that a fault at bus 2 determines the boundary for the PV penetration level (that is 53%) to avoid blinding.

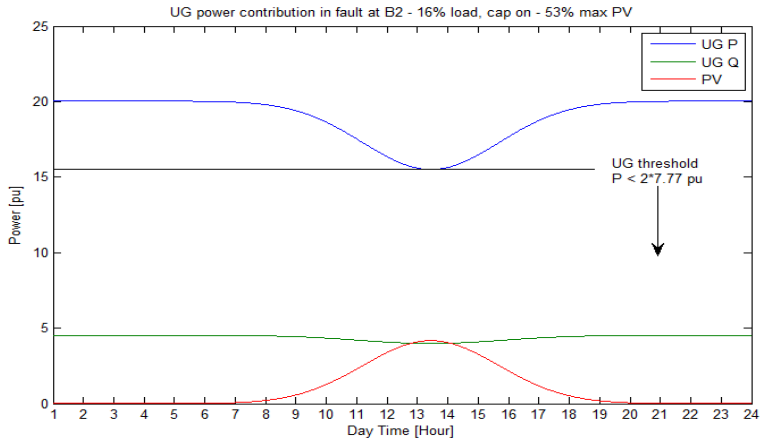

Figure 3.31: No blinding with 53% PV capacity-fault at bus 2 with 16% load

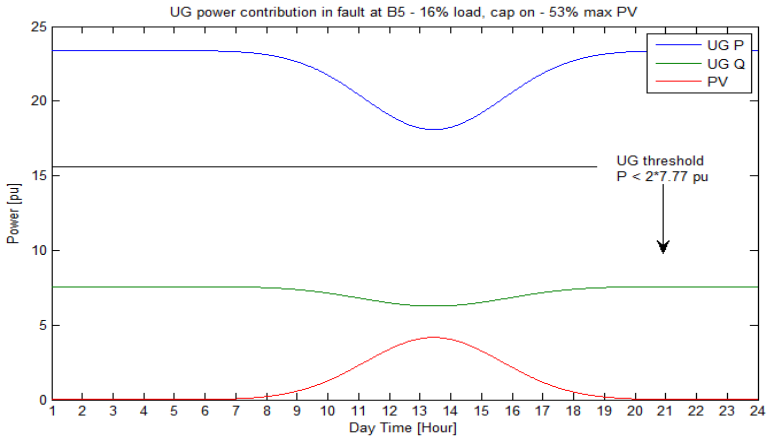

Figure 3.32: No blinding with 53% PV capacity-fault at bus 5 with 16% load

1.19. Harmonic Analysis

The PV source's inverter can be a major source of harmonics in the power grid. Total harmonic distortion and power quality are of primary concern when integrating DG. This section presents the effects of PV sources on the system total harmonic distortion. Industrial standards' regulations (applicable for utility operations) and possible filtering impacts are also studied and presented in this section. Simulated cases are combinations of the following options: Max PV Penetration: 30%, 50%, and 150%. Load: 30% and 100%. Capacitor banks: With and without capacitor banks. Filter: with and without filtering.

The inverters associated with the PV sources are assumed to be PWM inverters with the frequency modulation ratio (m_f) equal to 15. Therefore, their frequency spectrum starts from m_f-2 which is 13 in this case as shown Figure 3.33, for the case with 50% of PV penetration (out of full load), 30% of load connected and without capacitor. In this section, first all the cases without filters are discussed. Then, by referring to the related standards, the need for proper filtering is also considered and discussed.

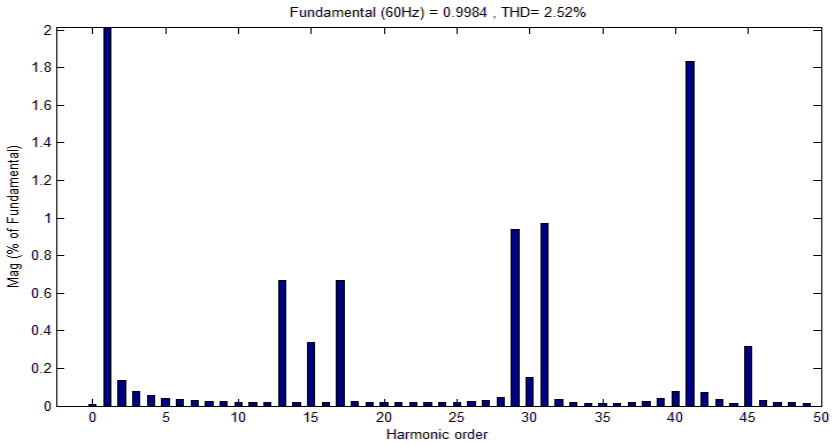

Figure 3.33: PV inverter high order harmonics at Bus 1(in the case with 50% PV, 30% load and disconnected cap)

1.19.1.Effect of PV Penetration Level

Figures 3.34 and 3.35 present Bus 1 harmonics for both the cases with 30% load available in the network and the capacitor connected. Figure 3.34 illustrates 50% (of full load at 1:00pm) PV power penetration, while Figure 30 illustrates the case with 150% PV power. By comparing these figures, it can be concluded that a change in the PV power penetration does not significantly affect the network harmonics. Both cases suffer from 2.52% of Total Harmonic Distortion (THD) with a slight difference in their fundamental frequency magnitude. It is useful to mention that all the harmonic plots in this section are magnified in the higher order parts. That is the fundamental frequency which is close to 99% in the plots, is truncated to focus on the high frequency components.

Changes in PV power penetration are also investigated with 100% load and capacitor on/off. The results indicate that PV power penetration level does not affect buses' THD%, significantly.

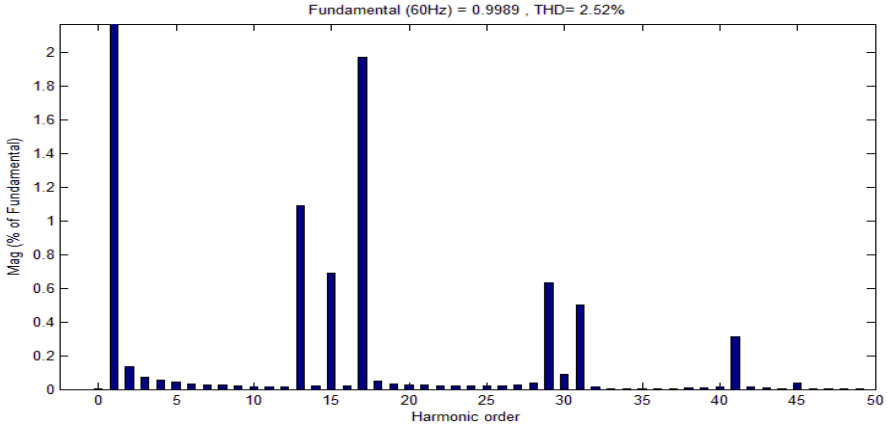

Figure 3.34: Bus 1 harmonics with 50% PV penetration, 30% load and connected cap

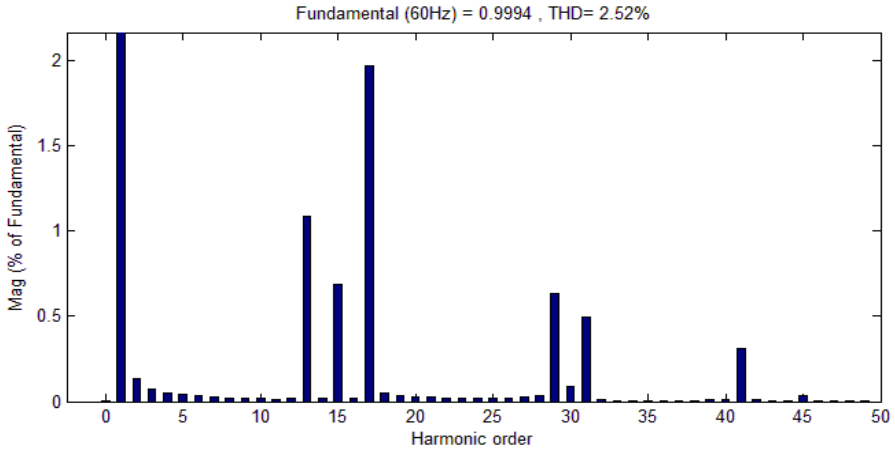

Figure 3.35: Bus 1 harmonics the case with 150% PV, 30% load and connected cap

1.19.2.Effect of Capacitor Bank

The capacitor bank's effects in the network are shown in Figures 3.36 and 3.37. Figure 3.36 presents the case with 50% (of full load at 1:00pm) PV, 30% load and capacitor disconnected which results in 15.15% THD that is significantly above the standards limits (which will be discussed.) Connecting the capacitor bank reduces the THD to 11.87% since cap provides a short circuit path for high order harmonics as shown in Figure 3.37. However, the detailed effect of capacitor bank connection depends on the system impedance, loading and resonant frequency. For instance some of the lower-order harmonic components become larger in this comparison case.

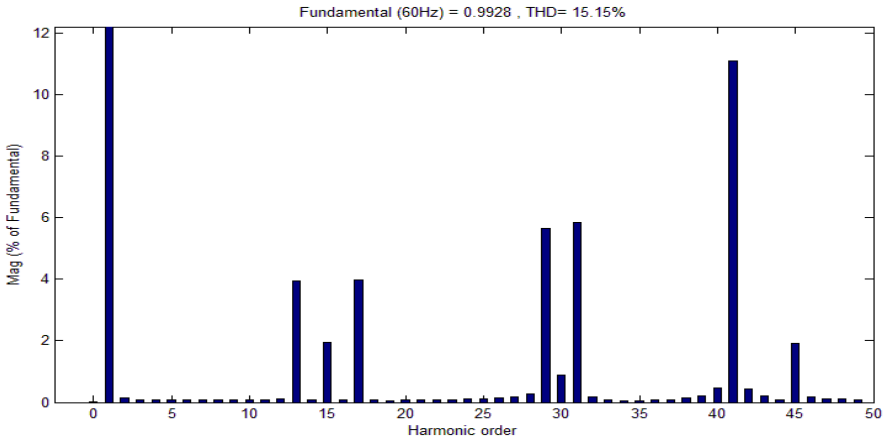

Figure 3.36: Bus 3 harmonics in the case with 50% PV, 30% load and disconnected cap

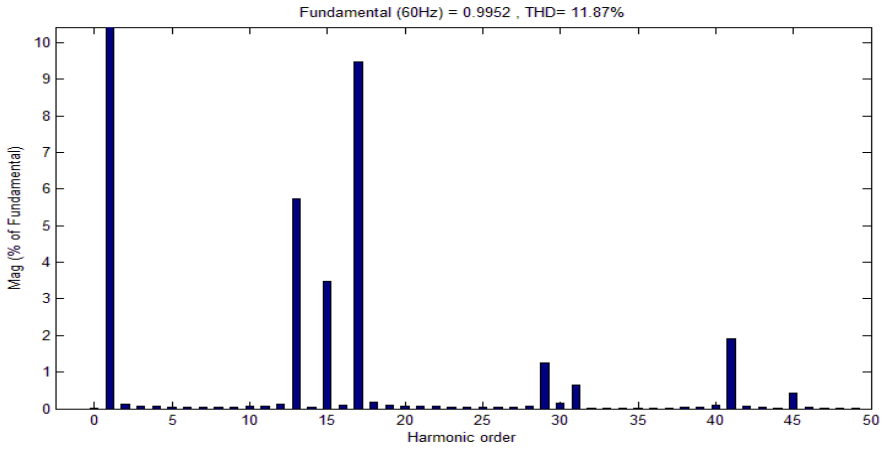

Figure 3.37: Bus 3 harmonics in the case with 50% PV, 30% load and connected cap

1.19.3.Effect of Bus Location

Figures 3.38 and 3.39 depict the case with 150% PV penetration and 100% of load consumption in the network with and without the capacitor bank. Locating a PV in the downstream feeders results in high magnitude harmonics. This happens since the PV sources' inverters harmonics add up and are more observable in the downstream feeders. For instance, Bus 7 harmonics are significantly higher than observed harmonics in upstream feeders' buses. That is comparing figure 3.39 and 3.41, with 150% PV, 100% load and cap connected, (for buses 7 and 3) shows the increase in THD% at bus 7. The same trend is observed in bus 1. This conclusion

should be taken into account in filtering the network harmonics as IEEE 519-1992 suggests that inverters' harmonics should be individually extinguished.

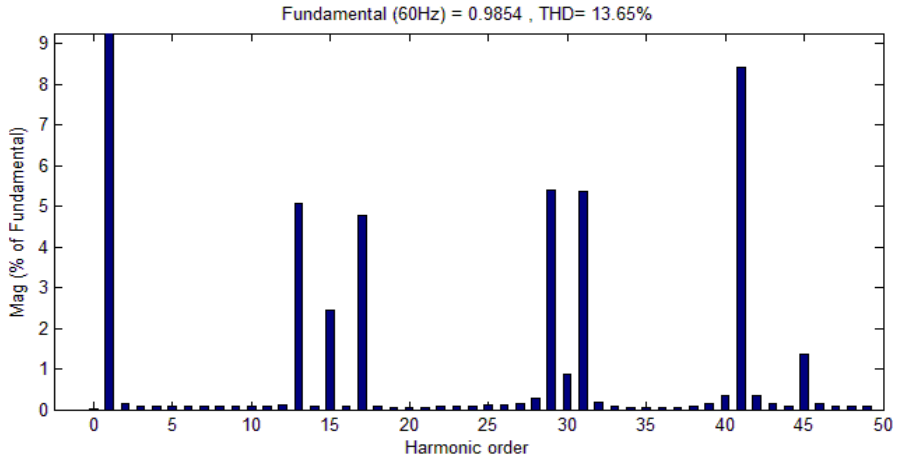

Figure3.38: Bus 7 harmonics in the case with 150% PV, 100% load and disconnected cap

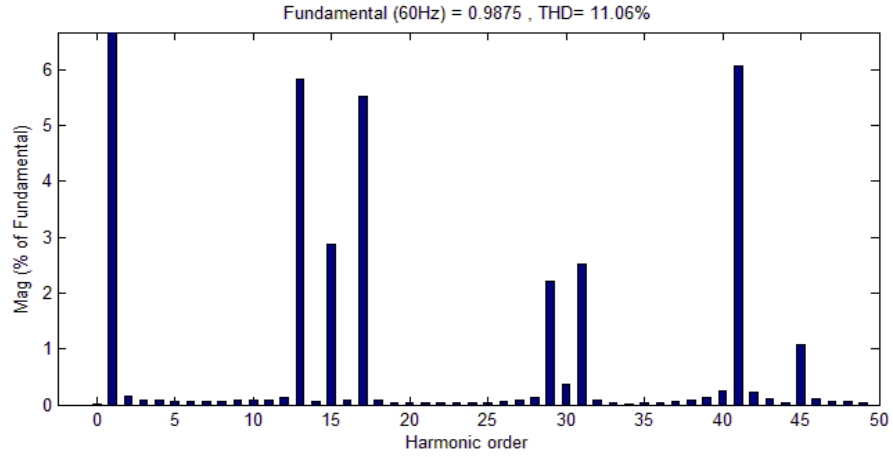

Figure 3.39: Bus 7 harmonics in the case with 150% PV, 100% load and connected cap

1.19.4.Effect of Load Level

Impacts of load levels on the harmonics are studied in this part. Figure 3.40 presents the case with 150% PV penetration level, the capacitor on and 30% of load in the network which results in 11.57% THD. By increasing the load to 100%, the THD is decreased to 7.41% as shown in Figure 3.41. Here the loads are simulated as constant impedances in MATLAB/Simulink.

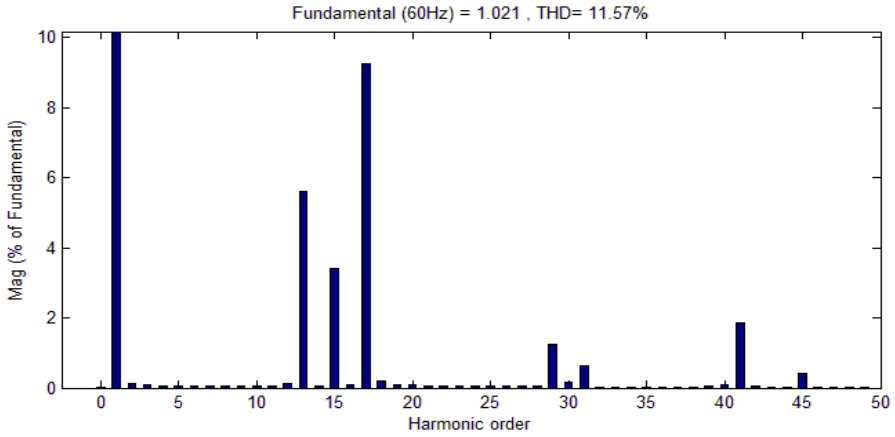

Figure 3.40: Bus 3 harmonics with 150% PV, 30% load and connected cap

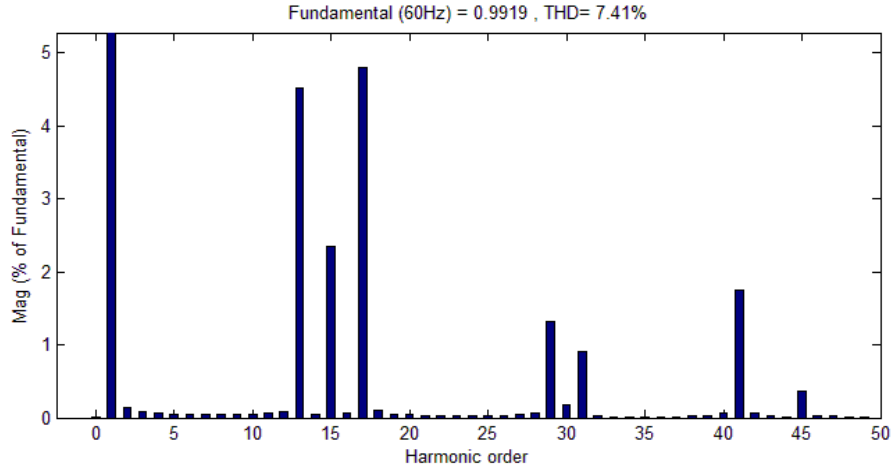

Figure 3.41: Bus 3 harmonics with 150% PV, 100% load and connected cap

1.20. Standards Regulations for Harmonic

The major standards applicable for PV integration in power networks, such IEEE 519, IEEE 1453 and UL 1741, have regulated the harmonic limits. These standards discuss the harmonic individual magnitudes and THD% for islanded mode and connected mode situations in Tables 3.1 and 3.2, as well considering the effect of the PV sources' power ratings (costumer capacity as a matter of I_{sc}/ I_L) as shown in table 3.3. Table 3.1 presents the harmonic limits for the islanded mode working condition by expressing that the THD shall not exceed 30%. Measurements should be

made for an inverter delivering its full capacity. Table 3.2 shows the individual harmonic orders allowed magnitude as well as the THD for a unit connected to the utility grid.

Table 3.1: Islanded mode harmonic limits from UL 1741

RMS distortion limits for individual harmonics Islanded mode	
Each individual	≤15%
THD %	≤30%

Table 3.2: Harmonic limits for UG connected units from UL 1741

RMS distortion limits for individual harmonics Connected mode	
Odd harmonics	**Distortion limit(%)**
3rd through 9th	4.0
11th through 15th	2.0
17th through 21st	1.5
23rd through 33rd	0.6
Above the 33rd	0.3
Even harmonics	**Distortion limit(%)**
2nd through 10th	1.0
12nd through 16th	0.5
18th through 22nd	0.375
24th through 34th	0.15
above through 36th	0.075
THD %	**≤5**

Customers' ratings also affect their harmonic injection into the network. IEEE 519 defines separate limits based on the customer sizes. These limits are tightened as the customer size increases, i.e., the ratio of I_{sc} (short circuit level on the bus) to I_L (load current) decreases. Table 3.3 indicates these limits for different customer sizes. These limits should be maintained by the inverters' vendors. That is inverters' vendors should consider appropriate filtering in their output in order to meet this regulation. However, utility companies need to control installation of units to assure operation within these boundaries.

Table 3.3: Distortion limits based on customer size from IEEE 519

Maximum Harmonic Distortion in Percent of I_L						
Individual Harmonic Orders (Odd harmonics)						
I_{sc}/ I_L	<11	11≤h<17	17≤h<23	23≤h<35	35≤h	THD%
< 20*	4.0	2.0	1.5	0.6	0.3	5.0
20<50	7.0	3.5	2.5	1.0	0.5	8.0
50<100	10.0	4.5	4.0	1.5	0.7	12.0
100<1000	12.0	5.5	5.0	2.0	1.0	15.0
>1000	15.0	7.0	6.0	2.5	1.4	20.0
Even harmonics are limited to 25% of odd harmonic limits above.						
Current distortion that results in dc offset, e.g. half wave converters, are not allowed.						
* All power generation equipment is limited to these values of current distortion regardless of I_{sc}/ I_L ratio.						
Where I_{sc} = Maximum short circuit current at PCC. I_L = Maximum demand load current (fundamental frequency component at PCC)						

1.21. Filtering effect on Harmonic

As discussed previously, the PV source's inverter harmonic spectrum starts at higher orders. Therefore, a low pass filter is the most suitable approach for reducing the harmonics. This section presents the significant impacts that harmonic filters have on harmonic reduction. In the following simulations filters have been installed in the output of each PV unit. Figure 3.42 presents the harmonic spectrum for the case with 50% PV, 30% load, and capacitor disconnected. The THD at Bus 1 is reduced from 2.52% to 0.63% as compared to Figure 3.33, i.e., the same case with 50% PV, 30% load and disconnected cap but without filters. It should be mentioned that before filtering the actual case did not meet the standards' regulations, whereas these limits are met by including the filters. A similar trend happens in other cases, too.

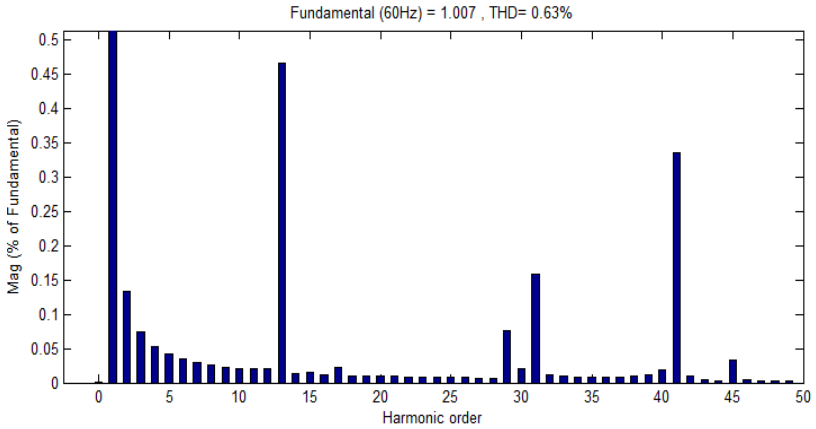

Figure 3.42: Filtered harmonics for the case in Figure 28, i.e. 50% PV, 30% load and disconnected cap

Figure 3.43 depicts the harmonic spectrum for the filtered case of Figure 3.36. This case considers 50% PV penetration, 30% load, and the capacitor bank disconnected from the network which can be considered as one of the worst cases. Adding a filter to the PV sources outputs reduces the THD from 15.15% to 2.1% at bus 3 which complies with IEEE 519. Figure 3.44 includes the harmonic spectrum resulting from adding the filters to the case used for Figure 3.37. This case consists of 50% PV capacity, 30% of load available and capacitor bank connected to the network. A dramatic decrease in individual harmonics and THD is obtained from the results of Figure 3.37 measured at bus 3. Therefore, by including filters, the harmonic issue can be resolved. These filters should be installed at each individual PV source by the customer.

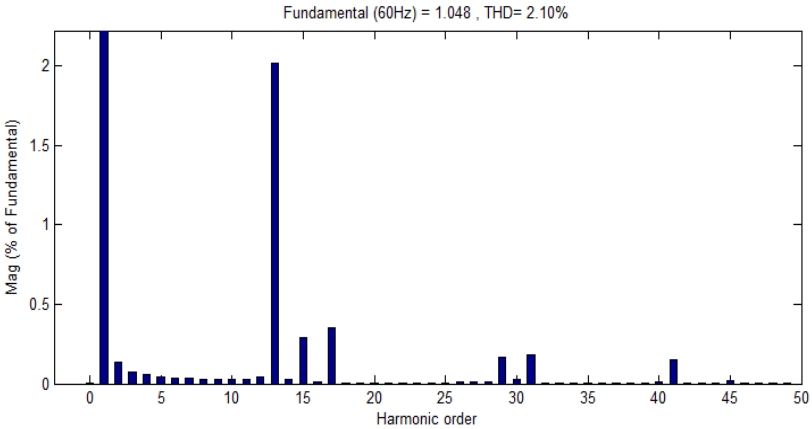

Figure 3.43: Filtered harmonics for the case in Figure 31, i.e. 50% PV, 30% load and disconnected cap

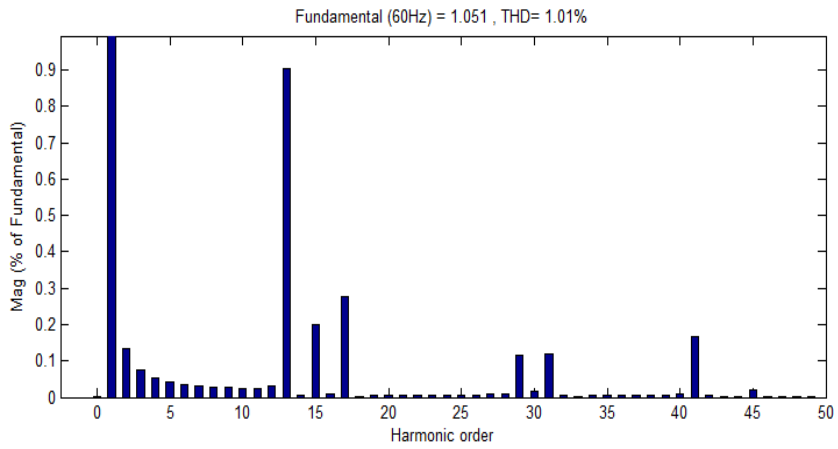

Figure 3.44: Filtered harmonics for the case in figure 32, i.e. 50% PV, 30% load and connected cap

1.22. Smart Inverter and Battery Storage

Most PVs are connecting to the grid by an inverter unit converting dc to ac and some are equipped with battery storage for better performance and reliability. Conventional inverters are designed simply to aim for maximum power output from the solar panels. Smart inverters are inverter units that have built-in capabilities for more grid support functions and better performance in various conditions. Utility companies can utilize these control strategies to reduce PV integration issues and even improve power.

International Electrotechnical Commission (IEC) technical committee 57, working group 17 has generated a standard report on smart inverter standard functions as Technical Report 61850-90-7. This is the first report and is proceeded by more revisions. The importance of smart inverter grid support functions and a widely accepted standard is beyond doubt. Based on analysis and provided tests there are scenarios where utilizing a function in a specific location and with improper consideration can result in adverse results. A brief review of available reports and literature is provided here targeting effects of smart inverter and storage units.

1.22.1.Smart Inverter Effects

One of the important questions for utility companies during PV integration is: what is the maximum PV penetration that a distribution feeder can integrate without affecting its power

quality or reliability; that is, the feeder hosting capacity determining the maximum possible PV penetration. Smart inverters' functions can improve PV integration issues if employed properly. Studies show that an improper usage of such function can result in adverse impacts. Three functions are discussed in this section which are widely accepted and the most effective for increasing distribution feeders hosting capacity. These functions include:

- Fixed Power factor
- Volt-VAR
- Volt-Watt

Function Effects: Fixed power factor

Using this function, smart inverter can absorb the excessive reactive power from the network and consequently reduce the overvoltage effect resulted by extra active power injection.

- PV units can cause overvoltage due to excessive injection of active power
- A fixed power factor improves the excess voltage level by absorbing reactive power from the network by the inverter
- Fixed PF and amount of reactive power absorption is highly dependent on the feeder X/R ratio
- In general, a set PF to 0.85 to 0.98 is common, PF equal to 0.95 to 0.98 seems effective for feeders with X/R ratio between 3 to 5,
- In general, a lower fixed PF has greater improvement effect on a feeder hosting capacity, especially for feeders that already have voltage issues
- Fixed PF function cannot fix the preexisting voltage issue on a feeder
- Depending on the overall feeder load PF, it is possible that using a low fixed PF cause under-voltage in a feeder
- Fixed power factor significantly increases the maximum hosting capacity on distribution feeders

Function Effects: Volt-VAR

The function provides more adaptive VAR control responding to the DERs PCC voltage. Utility or owner can set the function using the function curve.

- Volt-VAR control mostly results in increasing minimum and maximum hosting capacity but neutral and adverse effects are possible
- The function can have interference with voltage regulators causing adverse effect

- Volt-VAR tries to maintain voltage close to nominal causing extra reactive power flow
- The function can cause voltage drop in upstream voltage regulators
- The function without dead-band seems to have better impacts on hosting capacity
- Proper settings considering the feeder existing operational details is important
- Detailed case analysis before applying the function is advised
- Volt-VAR function provides better improvement on voltage levels in feeders with pre-existing voltage issues
- Available reactive power capacity is important in the performance of the function

Function Effects: Volt-Watt

This function also provides an adaptive mechanism where the unit's active power can be regulated based on the measured voltage.

- Volt-Watt function increases hosting capacity in most observations
- Neutral effect on hosting capacity is observed in few cases but no adverse results yet
- The function has not shown improvement in pre-existing voltage issues in feeders
- Higher settings (high voltage threshold for active power curtailment initiation) has no significant effects on hosting capacity

Parallel Operation

Smart inverter parallel operation can cause unexpected effects where possible interferences between different grid support functions are possible. Ongoing research is still working on discovering various aspects of the smart inverter parallel operation.

1.22.2. Battery Storage

Various types of storage technologies are considered and still under test and development for power storage with each having their own specifications and limitations. In general, battery storage challenges can be categorized under three main topics that are,

- Battery technology
- Storage unit control algorithm
- Project management and logistics

Technical effects and conclusions

- Voltage regulation with PV units using storage within ANSI limits is achieved both in study and practice

- Reducing the maximum voltage level and improving the minimum voltage with high PV penetration is an objective of storage units deployment
- Best results are obtained with bigger storage sizes closer to the end of the feeder
- Peak shaving and Load shifting have not shown a noticeable effect on voltage level for the studied networks, in some cases adverse effects are observed
- Storage unit proper design results in lower power losses in the network
- Using storage unit, a preferred load curve for feeder or substation is achievable
- Applications of storage can be costly, but with proper design and sizing it's a viable solution even for responding to frequency variations
- Using battery storage units with smoothing and defined load curve capabilities can reduce the number of tap changes in half for a nearby substation
- Utilizing hybrid battery storage (using different types of batteries) results in a wider variety of applications; i.e., high power battery provides voltage support and PV output smoothing whereas high energy battery enables peak shaving and time shifting
- Grid-tied battery storage unit projects focuses are shifted from technical challenges to economic optimization; algorithms for this aim are still under development
- A business model tailored for customer-owned energy storage systems is needed
- Currently available day-ahead weather models are not dependable or accurate for storage units curve determination
- Fault current changes during islanded operation requires specific protections design
- An auxiliary power should be considered for microgrids that are designed to operate in islanded mode for voltage regulation in the presence of inverters (constant voltage transformer is a solution with high expense)

1.23. References

[1] IEEE Recommended Practices and Requirements for Harmonic Control in Electrical Power Systems," IEEE Std 519-1992 , vol., no., pp.1,112, April 9 1993

[2] IEEE Recommended Practice for Utility Interface of Photovoltaic (PV) Systems," IEEE Std 929-2000 , vol., no., pp.i,, 2000

[3] IEEE Recommended Practice--Adoption of IEC 61000-4-15:2010, Electromagnetic compatibility (EMC)--Testing and measurement techniques--Flickermeter--Functional and design specifications," IEEE Std 1453-2011 , vol., no., pp.1,58, Oct. 21 2011

[4] IEEE Application Guide for IEEE Std 1547, IEEE Standard for Interconnecting Distributed Resources with Electric Power Systems," IEEE Std 1547.2-2008 , vol., no., pp.1,207, April 15 2009

[5] UL 1741 standard on Inverters, Converters, Controllers and Interconnection System Equipment for Use With Distributed Energy Resources

[6] *Common Functions for Smart Inverters, Version 3*. EPRI, Palo Alto, CA: 2013. 3002002233

[7] Grid Impacts of Distributed Generation with Advanced Inverter Functions: Hosting Capacity of Large-Scale Solar Photovoltaic Using Smart Inverters. EPRI, Palo Alto, CA: 2013. 3002001246

[8] Application Guid for Integration of Grid-Supportive Inverters: Version 1. EPRI, Palo Alto, CA: 2013. 3002001248

[9] Distribution Management Systems and Advanced Inverters: Autonomous Versus Integrated PV Control. EPRI, Palo Alto, CA: 2014. 3002003275

[10] Smart Inverter Field Experiences: A State of the Industry Overview. EPRI, Palo Alto, CA: 2013. 3002001247

[11] Recommended Smart Inverter Settings: Power Factor Control. EPRI, Palo Alto, CA: 2014. 3002003274

[12] Parallel Operation of Multiple Smart Inverters. EPRI, Palo Alto, CA: 2015. 3002005784

[13] Evaluation of Three-Phase Photovoltaic Inverters with Grid Support Functionality. EPRI, Palo Alto, CA: 2012. 1024361

[14] Modeling of a Battery Storage System for Southern Co: Application of Smart Inverter Functions for Energy Storage in OpenDSS. EPRI, Palo Alto, CA: 2016. 3002007481

[15] Analysis of Distribution System Effects of Energy Storage Through Simulation and Modelling: Energy Storage Grid Integration Analysis with OpenDSS. EPRI, Palo Alto, CA: 2012. 1024285

[16] Case Studies Evaluating Energy Storage as an Effective Grid Integration Tool: Selected Worldwide Results, Findings, and Lessons Learned. EPRI, Palo Alto, CA: 2014. 3002003271

[17] Utilizing Energy Storage as a PV Grid Integration Tool: Utility project case studies. EPRI, Palo Alto, CA: 2015. 3002005780

[18] Laboratory Evaluation of Grid-Tied Photovoltaic and Energy Storage Systems, EPRI, Palo Alto, CA: 2011. 1021987

[19] The Solar-to-Battery and Community Energy Storage Project Demonstrations at the Solar Energy Acceleration Center, 2015 Test Results and Analysis, EPRI, Palo Alto, CA: 2015.3002005786

Chapter 4
Challenges of PV Integration in Low-Voltage Secondary (Downtown) Networks

1.24. Introduction

Electric power systems have been experiencing fast and fundamental changes in recent years due to the introduction of distributed generation (DG). The smart grid, utilizing renewable energy-based distributed generation, attracts great attention due to environmental and reliability concerns [1], [2]. Government incentives, technological advances, and many other factors have resulted in a dramatic growth in photovoltaic (PV) power utilization and integration by both customers and utility companies [1]–[3]. Approximately 1.3 gigawatts of PV power were installed in the United States in the first quarter of 2015 resulting in a total of 21.3 GW of installed capacity [3]. The residential share of this installed capacity is 400 megawatts, which is a 76% rise compared to the same period in 2014 [3]. While this rapid pace of PV integration can potentially cause problems if not treated properly, both the government and utility customers have a great desire for PV integration.

Conventional urban lateral distribution networks are designed to accommodate unidirectional power flow from generation plants to the customers. This assumption is prone to violation by PV units causing reverse power flow in the case of excess power generation. The bidirectional flow of power can potentially interfere with the protective equipment. Other network operational conditions such as voltage profile, flicker, etc., can also be affected by the presence of PV power [1], [2]. Cloud effect, weather unpredictability, sun irradiance hourly changes, uncertainties in PV

operational conditions, losses due to improper integration, etc., can add additional challenges to the operation of the distribution networks [4], [5].

PV integration is more challenging in downtown underground networks than radial distribution networks due to the highly meshed circuit configuration and unidirectional power flow requirements. There exists very little research on PV power integration in low-voltage (LV) secondary networks especially when it comes to network protection [4]. Since integrated PV power generation was not considered in network designs, if costumers install PV generators with capacity higher than their consumption, the networks safety and reliability can be compromised resulting in frequent outages, excessive overloading, and inability in fault current termination [1]–[6].

One of the impacts of PV power on the secondary network is the network protection malfunction. Excess PV power can lead to loss of coordination, changes in fault ratings and source contributions [8]–[11]. In addition, solar irradiance is not fully predictable resulting in intermittent power generation on cloudy days. This may affect the network voltage profile [4] and cause voltage flicker. Also, excessive PV power generation can cause overvoltage [7]. However, the most critical effect of the integration of PV power in downtown networks is the network protector false trip and reclose issues that can lead to reactive power shortage and voltage instability which are the main focus of this research.

In [4] the effects of inverter-based, induction, and synchronous DGs on the secondary network's voltage profiles are investigated and the possibility of over and under voltage are explored by using probabilistic DG power distribution. It is also mentioned in [4] that with DG penetration in the network there is a chance of network protector tripping. However, the undesirable network protector false tripping is not elaborated on in [4]. Indeed, incidents such as

cascaded network protector trips, transformer overloads, and reclose issues are very likely in the presence of DG due to reverse power flow.

By contrast, this research focuses on the issue of reverse power flow and network protector false tripping and shows that widespread network protector trips and total secondary network voltage collapse can occur with low and moderate PV penetration levels. Much attention is paid to PV power rather than DG to address reactive power shortage, power variability, intermittence of power, and the emergence of the PV installments in downtown networks. The cascaded trips of network protectors can occur at some levels of PV penetration which may lead to shortage of reactive power from the primary feeders, and thus voltage instability. It is also shown here that the PV units can interfere with the reclose operation of the network protectors. These issues have not been fully investigated in the past literature. Subsequently, the effects of PV power on voltage profile and line overload, as well as voltage flicker as a result of cloud movement, in the secondary network are studied. It is observed that flicker in the range of "visible" can occur in the presence of PV power. Finally, a solution based on the differential current is proposed to prevent network protector false trip in the presence of PV power.

In this chapter, the terms *secondary network* and *downtown network* are interchangeably used and are the same. The remainder of this chapter is organized in the following order: Section II presents the secondary network under study and its modeling details. Microprocessor Network Protector Relay (MNPR) operation and modes are also discussed in this section along with the proposed solution to upgrade network protectors. In Section III, different PV arrangements and allocation methods are provided for simulation purposes. Simulation results regarding trip statistics, cascaded tripping, line overloading, and reclose issues are also discussed here using MNPR. The impacts of using the proposed Smart Network Protector Relay (SNPR) are discussed

in Section IV along with simulation results for cloud effects and network voltage profile in the presence of PV power. Finally, concluding remarks are made in Section V.

1.25. Low-Voltage Secondary Network

The secondary network is the portion of the distribution system between the primary feeders and customer premises where a highly meshed circuit delivers power to the customers from multiple points to increase reliability (See Figure 4.1) [18], [19]. The feeders are connected to one substation to avoid phase angle difference. The reliability and continuity of power is very important in downtown networks due to the nature of the loads and/or population located in those areas. This type of network has been used in the majority of the large cities in the United States since the early 20th century [17]. The traditional low-voltage downtown networks are designed such that the primary substation is the sole source of power. Any reverse power flow towards the primary feeders is an indicator of a fault being fed in the upstream network. Therefore, distributed generation potentially conflicts with network operation due to the possibility of bidirectional power flow.

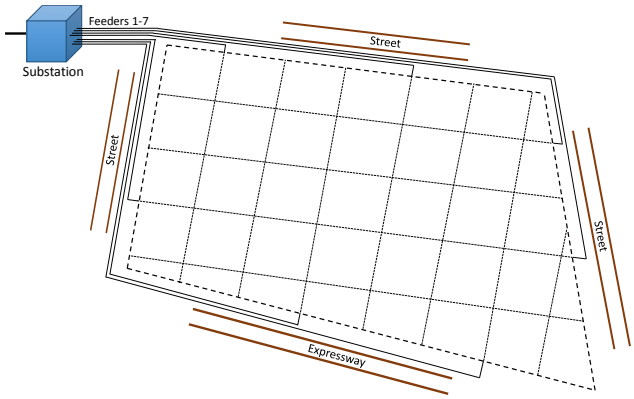

Figure 4.1: Approximate street boundaries and schematic of the network

1.25.1. Network under Study

The selected secondary network is the Warehouse District in the city of New Orleans. The network details are shown in Table 4.1. Secondary network nodes fall into two groups including

grid network (GN) and *spot* network (SN) that are both connected to the *feeder* network (FN)—also called upstream network—through the network protectors. This network is fed from seven 13.2 kV feeders all connected to the main substation. Feeders are connected to the grid and spot networks through underground grid vaults (GVs) and spot vaults (SVs) where transformers and network protector relays are located. Figure 2 depicts Grid Vault 2 connecting Feeders 1 and 6 to the grid network nodes 20 and 23. A total number of 169 transformers and their corresponding network protectors serve in the secondary network and are all located in the vaults. Out of these transformers 6, were disconnected by the utility company for maintenance and are considered open throughout this study. Each vault is fed from two or more feeders to increase network reliability. Grid network vaults with 120/208V levels serve loads up to 500 kVA (with the exception of two loads) that account for approximately 56% of the network's loads. Spot vaults with 120/208V or 277/480V levels serve high-load buildings and heavily loaded nodes up to 1500 kVA. A total of 228 loads are supplied in the selected downtown network as summarized in Table 4.2.

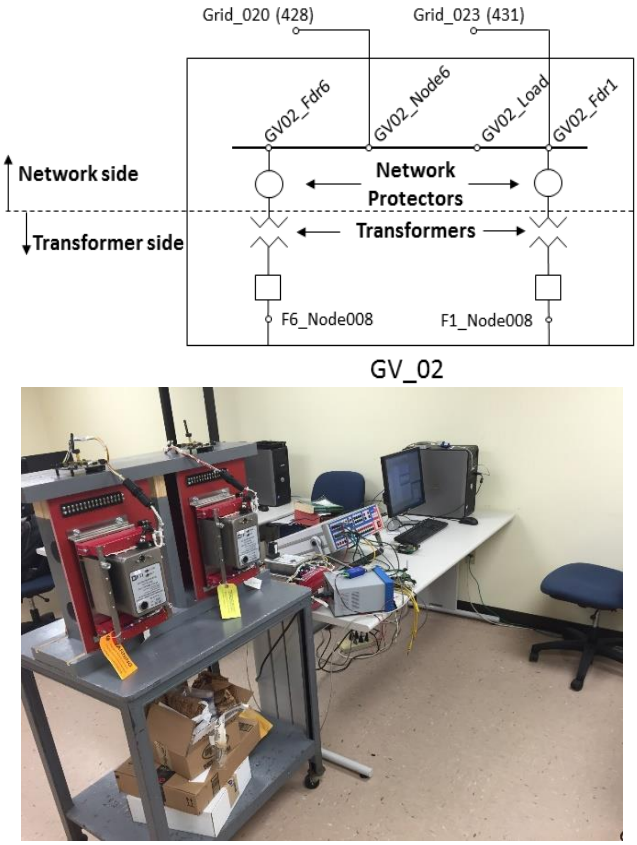

Figure 4.2: LV secondary network grid vault connected to two feeders and a lab test setup

Table 4.1: The secondary network details

Nodes			Lines			Loads amount (pu)			Trans
FN	GN	SN	FN	GN	SN	FN	GN	SN	vaults
409	648	152	408	717	118	0 0	20.48 7.18	13.21 4.62	169
1209			1243			P= 33.69MW Q= 11.79MVAr			163 in service

Table 4.2: The secondary network loads

Group	Power Range	Number of loads per network		Total
		GN	SN	
Very Large Load	Larger than 1 MVA	1	2	3
Large Load	0.2-1 MVA	31	22	53
Medium Load	50-200 KVA	80	1	81
Small Load	10-50 KVA	57	1	58
Very Small Load	0-10 KVA	33	0	33

†There is no load located on feeder nodes.

1.25.2.Network Model

The downtown network is modelled as a balanced three-phase system. Loads on all network nodes are also three-phase loads. Since the effect of excess power and the proposed solution (discussed later) are not affected by the imbalance that may exist in the network, the balanced three-phase modelling is adequate for the study. Load flow is used to solve the network for steady-state operation using the line impedance model. Nodes that are short distances apart are combined and a reduced network of 928 nodes is obtained. Power flow direction is used to determine the operation status of the network protector relays. Once reverse flow is detected, the pertinent network protector is tripped and load-flow is performed subsequently. A similar scenario is used for the relays' reclose operations. The total network full load is 33.69 MW and 11.79 MVAr while the networks minimum load is considered 16% of its full load based on the historical field data (recent minimum load is higher than 16%). Figure 4.3 depicts the model's voltage profile mismatch when compared to the data provided by the utility company. The figure shows less than 1% mismatch in voltage magnitude and 0.1% in phase angle at normal operation. These are the maximum errors among the 1209 nodes' voltage magnitudes and phase angles as compared to that provided by the utility company.

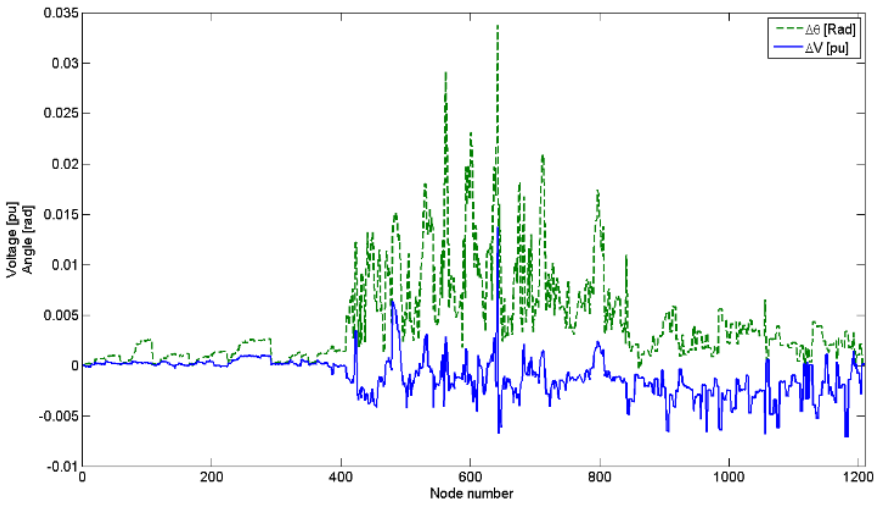

Figure 4.3: Simulated network voltage profile mismatch with field

Steady-state studies reveal potential negative impacts of PV integration in the downtown network, and thus load-flow is found sufficient for this purpose. It is anticipated that by taking the dynamic behaviour of the network into account through more detailed simulations, the observed impacts will be slightly larger. Since the objective of this chapter is to present the investigation of potential impacts and not detailed simulations necessary for implementation, steady-state simulation is chosen. The transients usually aggravate the predicted problems and detailed time-domain simulations will possibly show additional negative impacts in the study, but will not affect the proposed solution as will be explained.

1.25.3.Microprocessor Network Protector Relay (MNPR)

Network protector relays are the key elements in a secondary network protection system. The modern MNPR is a digital relay that combines the functions of a master relay and a network phasing relay. The older types of these MNPR relays (that are still in use) are electro mechanical requiring fine mechanical adjustment to operate. The MNPRs are programmable and have many built-in controls to avoid their ancestor issues such as “ratcheting” [18].

Regular MNPR has five trip and three reclose modes of operation [17]. The commonly used “Sensitive Trip” and “Reclose” modes are modelled in this study. Since the downtown network is powered from multiple points, power can flow into the secondary network from one upstream feeder and exit from it into another upstream feeder feeding a fault. In normal operation, where there are no faults in the upstream network, the power flows from upstream network to the downtown network through all feeders. The MNPRs’ primary task is to protect the network against upstream feeder faults. This is done by sensing a reverse power flow through the Sensitive Trip mode. Once a faulty feeder is disconnected from the main substation, the fault in the upstream

network is fed by the other feeders through the downtown network. Network protectors sense the reverse power flow from the downtown network to the upstream feeder and disconnect the circuit. The MNPR takes six cycles to trip and an adjustable number of cycles are required to occur for a reclose operation. A reclose time of six cycles is considered in this study. The Sensitive Trip is set to 0.15% of the rated transformer current [24]. The transformer protection will also trip overloaded transformers when the loading exceeds 100% of the transformer rating. It is important to note that the transformer rating is usually higher than the transformer nominal load. Line overload is also considered in here by adopting 105% of the line nominal current as the overload limit. It should be noted that the underground downtown distribution lines have lower overload tolerance than their overhead counterparts due to the insulation material of the cables.

The reclose characteristic of the network protector relay is shown in Figure 4.4 In the figure, reclosing voltage V_D, which is the voltage difference between the two sides of the network protector, is observed. That is, $\boldsymbol{V_D = V_T - V_N}$ where $\boldsymbol{V_T}$ is the transformer side voltage and $\boldsymbol{V_N}$ is the voltage on the network side (see Figure 4.2). If the fault exists in the upstream circuit, transformer voltage $\boldsymbol{V_T}$ lags or is smaller in magnitude than network voltage $\boldsymbol{V_N}$. The reclosing action takes place only when the voltage on the transformer side of the open network protector is slightly higher in magnitude and is in-phase with or leading the voltage on the network side of the network protector. The default setting for the reclose voltage is 1.4V (this usually ranges 0.1 to 10.0V).

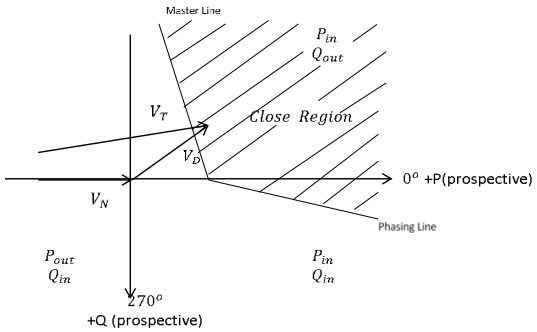

Figure 4.4: Reclosing characteristic of the MNPR

1.25.4.Smart Network Protector Relay (SNPR)

The smart network protector relay is proposed here to prevent the false trip due to reverse power flow caused by excess power inside the network and to allow isolation in the case of an upstream fault. The SNPR operation is similar to a regular network protector in all modes except for the Sensitive Trip mode. In the Sensitive Trip mode a regular MNPR detects a reverse power flow and initiates a trip assuming fault occurrence in the upstream feeder. In the presence of PV units, a regular MNPR does not differentiate between the reverse flow due to an upstream fault and that due to the excess PV power. Available solutions target the power generation from PVs (DGs in general) in order to prevent reverse power flow. These solutions either limit the power generation by PV units to the customer's minimum load consumption, or they require a large communication infrastructure that makes it possible to turn off the PV units by the utility control center when reverse power is detected [7], [23]. This can cause customer complaints and is a waste of available renewable energy, especially when network minimum load is considered. On the other hand, this is not applicable to the currently installed PV units with high capacity (e.g., PV Arrangement 1 explained in the next section). In contrast, by using the SNPR, an algorithm is proposed to detect excess power and override the Sensitive Trip in this case. The proposed protection mechanism does not limit the customers' power generation nor does it need a comprehensive communication infrastructure to communicate with the individual PV units.

Proposed excess power detection method: The proposed method is a *generalized* differential current protection method. First, a cut-set that surrounds part of the upstream feeder is obtained. This cut-set covers the protected upstream network including the network protectors that separate the feeder network from the secondary network. Two possible cut-sets are depicted as examples in Fig. 5a. These cut-sets cross the feeder lines connected to GVs and SVs as well as the feeder breaker or a feeder line. Ideally, the cut-set encompasses the entire feeder's borders with the secondary network. However, a smaller portion of the feeder can also be chosen to simplify the circuit.

Next, the summation of all measured currents in the selected cut-set is obtained. If the summation is zero, the power only travels through the cut-set; i.e., power flows in the forward or reverse direction through the cut-set with no leak inside the cut-set. If the currents' sum is not zero, power is consumed within the cut-set; i.e., a fault exists in the cut-set. It should be mentioned that the proposed approach is conducted on each phase separately. That is, each phase has a separate cut-set that examines the currents into the cut-set and out of it. Figure 5.b depicts the three-phase representation of Cut-set 2 shown in Figure 4.5.a. The signed summation of these currents must add up to zero for safe operation. Upstream load (if any) phase currents are included in the summation. Thus, three-phase current imbalance in the downtown network does not affect the detection mechanism. Selection of the cut-set is critical as it must encompass a feeder or a part of a feeder along the feeder borders that includes network protectors. Also, the interior nodes must not include loads; that is, the load branches, if there are any in the feeder network, must lie on the cut-set itself (and thus the cut-set is non-planar). In summary, both the reverse power flow and the non-zero cut-set net current signal must exist for a Sensitive Trip to be issued in the proposed SNPR as shown in Figure 4.6. The proposed SNPR aims to increase network reliability while being

simple as a feasible upgrade for available MNPRs. Communication between the cut-set current measurements are to be performed and the results are transmitted to all the cut-set SNPRs in six cycles for effective operation. Since the proposed mechanism is only applied to the upstream network, a smaller network is targeted, and thus the communications infrastructure is not large and can be as small as a feeder or a part of a feeder.

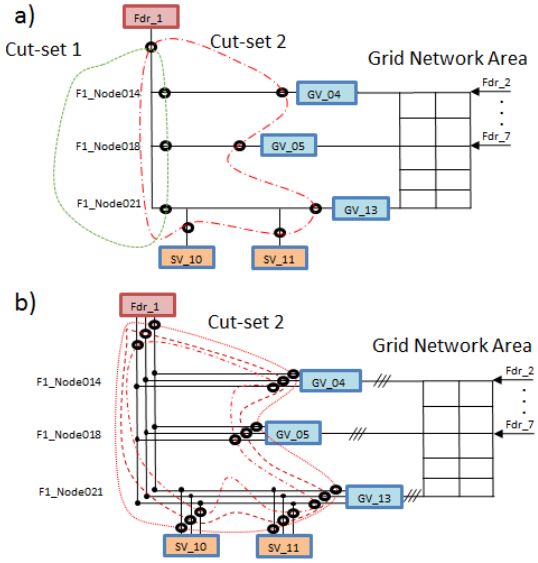

Figure 4.5: a) Two instances of closed cut-sets b) Cut-set 2 per-phase structure of the proposed SNPR

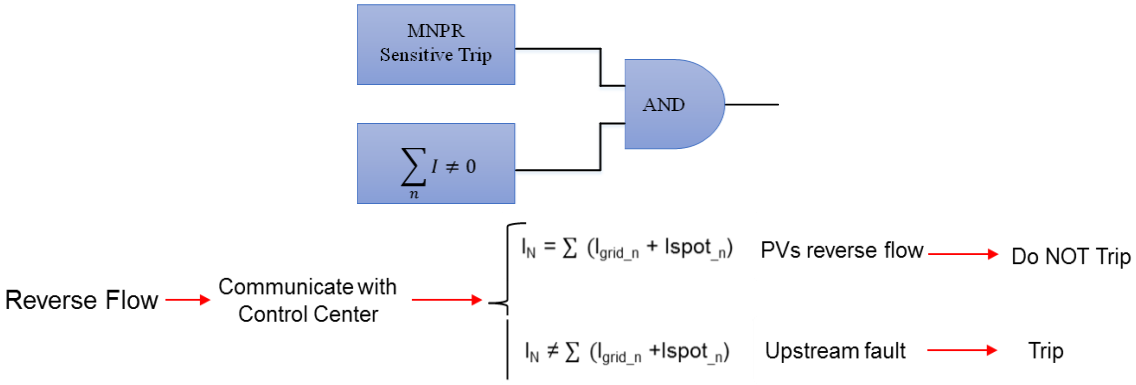

Figure 4.6: Smart Network Protector Relay (SNPR) sensitive trip logic

Many studies have proposed communications infrastructure for control and monitoring of DG units and the distribution network containing them [11]–[15]. However, in the proposed SNPR, communicating with a large number of PV units is not required. Rather, the communications system transmits a small amount of data which is the value of the measured cut-set currents to and

from the cut-set control center, that can be one of the SNPRs. Alternatively, the current transformers can be connected in parallel such that the current summation can be physically obtained.

It should also be mentioned that changing the setting of the existing network protectors to allow higher reverse power flow is challenging since high-impedance and single-phase faults, which are low power faults in nature, may be missed and cause damage to the critical downtown underground network. In addition, hourly and intermittent changes of solar power make the relay setting a difficult task.

1.26. MNPR Operation

In this section, detailed studies of MNPR operation are discussed. The solar power generated by the PV panels inside the downtown network cause changes in the feeder and line currents that can lead to network protector false trips and/or line and transformer overloads. In the following discussion different cases of solar and load powers are considered; then, voltage profile and stability as well as line and transformer overloads are studied.

One of the major consequences of the network protector trips is the change in the feeders' injected reactive and active power patterns that may lead to reactive power shortage, in the presence of unity-power factor solar power, followed by voltage instability. As the number of disconnected network protectors increases, network connectivity to the upstream feeder network decreases leading to a less stable downtown network. The effect of the downtown network connectivity on the voltage stability is studied through the lowest eigenvalue of the network Jacobian matrix. Here, all PV units are considered as constant power generations, and thus bus voltages are not controlled. As the minimum eigenvalue approaches zero, the Jacobian matrix approaches singularity and more reactive power support is required to maintain the voltage.

1.26.1.PV Arrangements

PV power allocation varies by costumers' locations and interest. It is reasonable to assume that with higher PV penetration, the chances of reverse power flow is increased. The PV power penetration can be either high-generation sites, such as large buildings or large utility-owned solar generators, or distributed PV power generation. In the latter form, one can reasonably assume that the amount of power generation at each node is proportional to the nominal load at that node. Consequently, three PV arrangements are considered in this study and are referred to as Arrangements 1, 2, and 3.

Arrangement 1 (distributed): This arrangement is comprised of distributed PV units across all the downtown network loads. In this arrangement PV units are at 228 loaded nodes. Power of the PV unit at each node in Arrangement 1 is varied from 15% to 150% of the full load of the node. That is, all the PV generators experience 5%, 15%, 30%, 45%,…, and 150% of their corresponding node's full load, simultaneously.

Arrangement 2 (lump): This arrangement consists of 56 large PV units installed on 56 Large and Very Large Loads (see Table II) in grid and spot networks. Total power of PV in Arrangement 2 is varied from 5% to 150% of the full load of the entire downtown network similar to the previous case. For instance, at 150% penetration, PV Arrangement 2 has a total capacity of 1.5 times the total downtown network full load (33.6 MW); that is, 50.4 MW is distributed among 56 PV units proportional to their corresponding node's load size.

Arrangement 3 (residential): This arrangement contains PV generation on the loads less than 200KW in the grid network, which are 172 loads in this study with a total of 10.12 MW power consumption. In this arrangement, each installed PV unit generates power varying from 5% to 150% of its corresponding node's full load similar to Arrangement 1.

1.26.2.MNPR Trip Statistics

The network protector's primary task is to protect the upstream network and transformers. The transformers connect the upstream feeders to the secondary network and are protected against reverse power flow and overload. As the PV penetration level rises, the chances of transformer disconnects due to reverse flow increase. Also, transformer overload can occur if a large share of disconnected transformers is burdened on the connected ones. If all connections to a load are disconnected, the load and its PV generator are removed from the analysis. This is usually the case when a spot network sends power to all of its connected upstream feeders, and thus all its network protectors trip.

The MNPRs are first simulated under hourly load and solar power for different seasons of the year. The solar power measured by the authors, as well as the load profiles provided by the utility company, for the full year of 2015 are utilized here. Figures 4.7.a and 4.7.c illustrate load patterns of days with typical and minimum load profile in the summer and winter. Figure 4.7.b and 4.7.d present normalized PV power of days with typical and maximum solar power generation in the summer and winter. The numbers of MNPR trips are presented in Figure 4.8 using typical load profile and typical PV power for different scenarios of PV Arrangements 1 and 2 in each season. The PV% in the figure represents the maximum power capacity of individual PV units (that occurs at summer noon time) with respect to their pertinent customer full load. In order to consider the worst case, Figure 4.9 presents similar scenarios using minimum load and maximum PV power for similar arrangements for each season. It is shown in the figures that in the cases where the solar power is greater than that of the load (mostly around noon time) excessive MNPR trips occur, leading to voltage instability in some cases.

Seasons	From	To
Spring	March 16th	May 15th
Summer	May 16th	September 7th

Fall	September 8th	November 30th
Winter	December 1st	March 15th

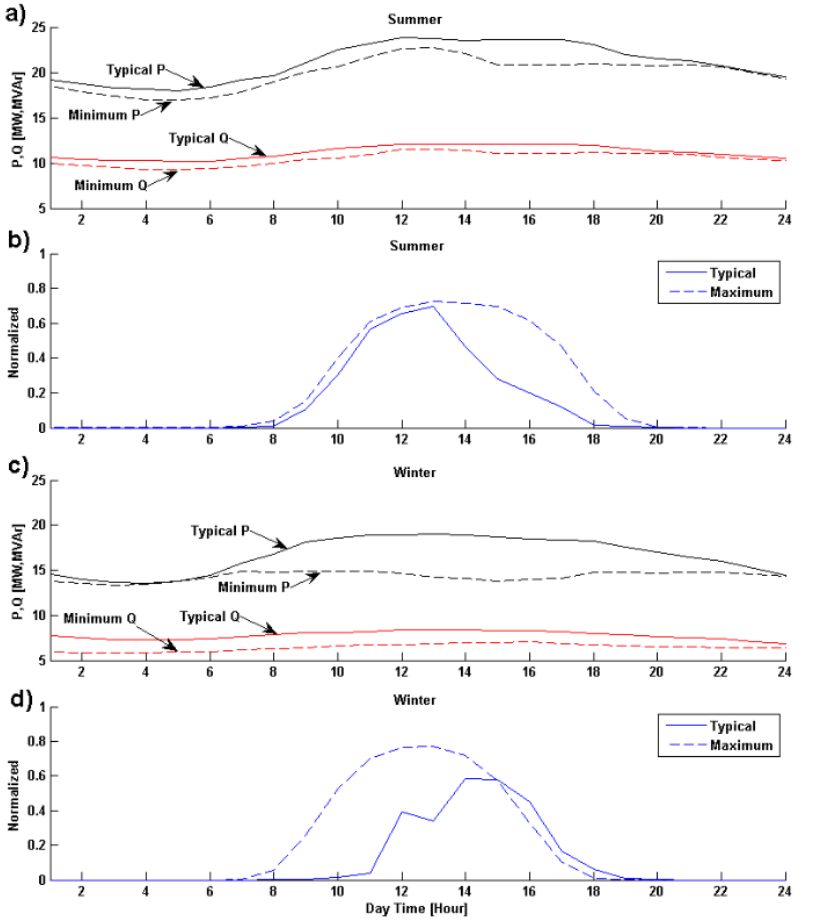

Figure 4.7: Seasons time periods and Seasons: minimum and typical load profiles, maximum and typical PV power. a) Summer days load profile b) Summer days PV power c) Winter days load profile d) Winter days PV power

In addition, Tables 4.3 through 4.5 present various solar power penetration and loads statistics independent of the time of the day. Table 4.3 shows the number of tripped network protectors (transformers) versus PV penetration levels for Arrangement 1 at the network's historical minimum and full load conditions that are 16% and 100% of the downtown network's full load, respectively. The shaded rows in the table illustrate cases where voltage instability and collapse occur due to reactive power shortage fed by upstream feeders. Recall that PV panels usually operate at unity power factor to increase efficiency, and thus are not sources of reactive power.

The emerging smart inverters that are capable of generating reactive power are now under development [25] and study, and their full deployment requires sophisticated control mechanisms along with a comprehensive communication structure. Even with the smart inverters, isolation of the downtown network protector from the upstream feeder network can occur leading to an islanded downtown network. Since all loads are equipped with PV power proportional to their full load demand, the reverse flow does not occur when the PV generation falls below the load demand as shown in Table 4.3. However, when the PV generation exceeds the load demand, both reverse flow and MNPR trips occur in large numbers leading to voltage instability. One outcome of this result is the possibility of voltage collapse around noon when all PV power reserve is in place (as suggested by Figure 4.8 and 4.9). When the system experiences minimum load, the voltage instability occurs at significantly lower PV power levels.

Table 4.3: MNPR operations in the case: PV Arrangement 1

	Full Load					Minimum Load				
		Trip Incidents			Final		Trip Incidents			Final
PV %	#	R	O	T	F	#	R	O	T	F
5	0	0	0	0	0	0	0	0	0	0
15	0	0	0	0	0	0	0	0	0	0
30	0	0	0	0	0	1	152	0	152	152
45	0	0	0	0	0	1	156	0	156	156
60	3	9	0	9	9	1	157	0	157	157
75	3	8	0	8	8	1	157	0	157	157
90	3	10	0	10	10	1	159	0	159	159
105	1	143	0	143	143	1	159	0	159	159
120	1	155	0	155	155	1	159	0	159	159
135	1	157	0	157	157	1	159	0	159	159
150	1	157	0	157	157	1	159	0	159	159

*#: rounds of cascaded trips, R: trip due to reverse flow, O: trip due to overload, T: Total number of trip incidents, F: Final open MNPRs

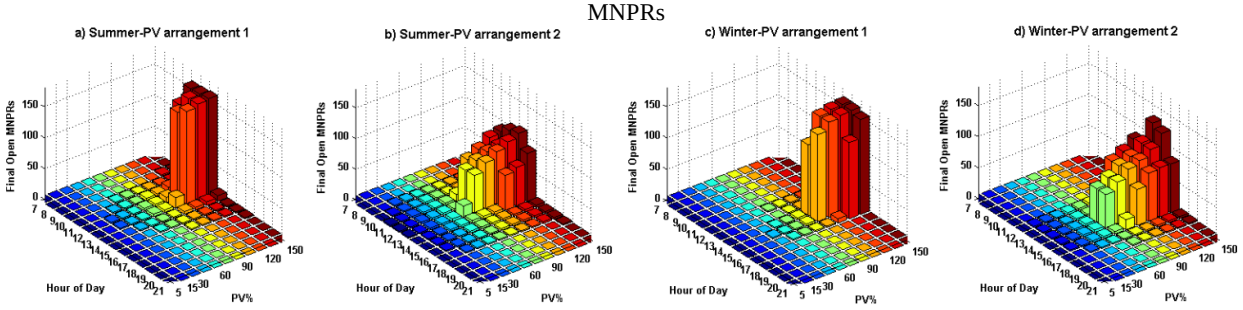

Figure 4.8: Number of tripped MNPRs with typical hourly load and typical solar power for different seasons and PV arrangements

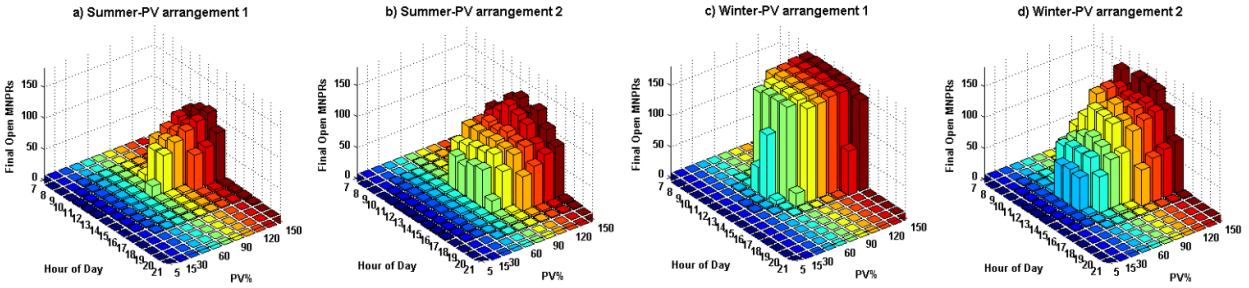

Figure 4.9: Number of tripped MNPRs with minimum hourly load and maximum solar power for different seasons and PV arrangements

Tables 4.4 and 4.5 illustrate the trip statistics when Arrangements 2 and 3 are adopted. In Table 4.4, when PV power penetration level is 150% (of full load) at network full load condition, 395 incidents of reclose occur in 15 rounds of cascaded trip incidents leading to a final 111 tripped MNPRs at which point the network voltage stability is undermined. In the cascaded trips, several rounds of trips and/or reclose operation occur before the network settles down to a steady configuration. One round of MNPR trips pushes the extra power towards other network protectors and causes a separate round of trips in other network protectors and/or causes some of the tripped MNPRs to reclose. This may repeat a few times before the network comes to a final configuration as shown in Table 4.4. This phenomenon may lead to *pumping* (which happens more severely with Arrangements 2 and 3). In addition, MNPR trip incidents leave lower paths for extra power to flow toward the upstream network or for demanded power to flow towards loads. As the excess power is guided through fewer numbers of transformers, the chance of transformer overload increases and additional trips due to overload occur.

Table 4.5: MNPR operations in the case: PV Arrangement 3

	Full Load					Minimum Load				
		Trip Incidents			Final		Trip Incidents			Final
PV %	#	R	O	T	F	#	R	O	T	F
5	0	0	0	0	0	0	0	0	0	0
15	0	0	0	0	0	0	0	0	0	0

30	0	0	0	0	0	>20	275	0	275	51
45	1	1	0	1	1	>20	460	0	460	79
60	1	1	0	1	1	>20	436	2	438	81
75	1	1	0	1	1	>20	478	6	484	76
90	1	1	0	1	1	1	94	0	94	94
105	1	1	0	1	1	1	96	0	96	96
120	2	4	0	4	4	1	96	0	96	96
135	3	10	0	10	9	1	96	0	96	96
150	>20	98	0	98	21	1	96	0	96	96

*#: rounds of cascaded trips, R: trip due to reverse flow, O: trip due to overload, T: Total number of trip incidents, F: Final open MNPRs

Table 4.4: MNPR operations in the case: PV Arrangement 2

	Full Load					Minimum Load				
		Trip Incidents					Trip Incidents			
PV %	#	R	O	T	F	#	R	O	T	F
5	0	0	0	0	0	1	1	0	1	1
15	1	1	0	1	1	6	81	0	71	71
30	1	2	0	2	2	>20	508	0	152	133
45	1	2	0	2	2	>20	584	2	157	132
60	1	3	0	3	3	1	152	0	152	152
75	3	83	0	83	58	1	154	0	154	154
90	>20	214	0	214	68	1	156	0	156	156
105	5	95	0	95	83	1	156	0	156	156
120	>20	208	1	209	81	1	156	1	157	157
135	>20	422	0	422	96	1	146	11	157	157
150	15	497	9	506	111	1	146	11	157	157

*#: rounds of cascaded trips, R: trip due to reverse flow, O: trip due to overload, T: Total number of trip incidents, F: Final open MNPRs

With Arrangement 3, the total PV power generation is lower than with the other two arrangements, and thus PV generation is never higher than the downtown network's full load. Consequently, voltage instability does not occur in the case with full load. As the network experiences the minimum load, one can expect a large number of MNPR trips and voltage instability at higher penetration levels than in Arrangement 1 as shown in Table 4.5. In several PV power levels with Arrangement 3, a number of cascaded trips occur that involve reclose actions. At the network minimum load, when PV power is between 30% and 75%, the number of trip-reclose incidents is significantly high and pumping occurs.

Next, the voltage stability metric introduced earlier is shown in Table 4.6 for Arrangement 3. One can observe that as the number of false trips increases, the feeder network's average reactive power injection through the remaining connected transformers increases and the smallest eigenvalue approaches zero. The negative eigenvalue occurs where network voltage collapse is predicted by Table 4.5 for this arrangement. The other Arrangements show similar behavior but are not shown here due to lack of space.

Table 4.6: Voltage stability metrics for cases with PV Arrangement 3

	Full Load		Minimum Load	
PV%	Minimum Eigenvalue	Average Q per NPs [pu]	Minimum Eigenvalue	Average Q per NPs [pu]
5	0.21	0.0683	0.22	0.010
15	0.21	0.0679	0.22	0.010
30	0.21	0.0672	0.09	0.013
45	0.21	0.0669	4.2e-15	0.017
60	0.21	0.0664	5.0e-15	0.018
75	0.21	0.0660	0.08	0.019
90	0.21	0.0656	-8.9	0.020
105	0.21	0.0653	-21.45	0.021
120	0.10	0.0662	-163.3	0.022
135	0.10	0.0678	-20.52	0.023
150	0.16	0.0731	-2.1	0.024

1.26.3.Distribution Line Overload Statistics

The PV generation inside the downtown network may affect the distribution lines' loading and cause them to overload. The number of overloaded lines in the network increases with the PV power. Table 4.7 summarizes the distribution line overload incidents as a function of PV power level for Arrangements 1, 2, and 3 at full and minimum loads. As predicted, with distributed PV power generation the likelihood of line overload is lower. Here, the overload level is considered as 105% of the underground line current at the downtown network full load condition when no PV generation exists in the network. This result is conservative in the sense that the actual overload capability of the distribution lines may be higher in the actual network. However, this data was not

available. Also, no line disconnect is assumed due to overload since the loadability of individual lines were not known.

Table 4.7: Overloaded network lines in different cases

	PV Arrangement 1		PV Arrangement 2		PV Arrangement 3	
PV%	Full load	Min load	Full load	Min load	Full load	Min load
5	0	0	8	0	16	0
15	0	0	44	35	38	5
30	0	n/a	72	96	48	34
45	0	n/a	89	188	60	118
60	0	n/a	99	n/a	70	121
75	0	n/a	132	n/a	75	185
90	0	n/a	139	n/a	81	n/a
105	n/a	n/a	221	n/a	90	n/a
120	n/a	n/a	239	n/a	109	n/a
135	n/a	n/a	301	n/a	115	n/a
150	n/a	n/a	n/a	n/a	151	n/a

1.26.4.MNPR Reclose operation

The default reclose voltage setting of the relay simulated in this study is 1.4V (V_D=1.4V) [24]. The relay reclose voltage setting establishes the minimum difference voltage required to issue a reclose command when the feeder voltage and network voltage are in phase. With the default reclose setting, a number of network protectors that are tripped due to reverse power flow will reclose after the reclose cycle has passed. A solar power penetration scenario is arranged to show the pumping effect. At the MNPR in Grid Vault 29 fed by Feeder 4, the voltage difference is $\mathbf{V_D = 1.87V} > 1.4V$; and at the MNPR in Grid Vault 44 fed by Feeder 7, $\mathbf{V_D = 1.62V} > 1.4V$ after the trip due to reverse power flow. Thus, the two network protectors in the vaults are ready to reclose. However, after MNPRs reclosed, both transformers see reverse power again and subsequently trip. This process will continue leading to excessive relay operations which is known as *pumping* [20]. Allowing the network protector to close with a small difference voltage magnitude can lead to pumping in certain arrangements and penetration levels as observed. However, it can be seen that when the threshold is increased to 2V, pumping does not occur when the MNPR is used. As

expected, pumping due to reverse power does not occur when SNPR is utilized in either reclose setting case illustrated.

1.27. Case Studies for SNPR

The results obtained in previous sections indicate network protector false operations in the presence of PV power generation inside the network. Currently, the network protectors can't differentiate between PV excess power flow and an upstream fault. That is, the network protectors trip the circuit once they sense a reverse flow regardless of its cause. The MNPR false trip can destabilize the network as discussed in the previous section.

The idea of a smart network protector was explained earlier in Section II. Here, the smart network protector is applied by upgrading regular network protectors with an overriding logic. This overriding logic prevents false tripping when reverse flow is originated from PV excess power generation in downstream branches. Thus, in the case where there is no fault in the upstream feeder with reverse flow, the smart network protector avoids circuit disconnection. Consequently, it is expected that no trips occur unless transformer overload limits are reached. Here, the PV Arrangement 2 with 120% PV penetration is considered (from Table 4.4) and Feeder 1 is selected to show the operation of the SNPR in differentiating between an upstream fault and PV excess power. Figure 4.10 presents the topology of feeder 1 where a cut-set similar to that of Figure 4.5 crosses all of the upstream boarder nodes (nodes depicted in red). Under normal operation, the summation of the currents from all the vaults is equal to that of the main breaker considering no line losses. These values are given in Table 4.8 where positive currents represent current directions into the cut-set. It is shown that the sum of the signed currents equals 0.0053+j0.0105 under the PV excess power; a small value that indicates excess power only. Next, a three-phase high-impedance fault of 0.1 p.u (power) is introduced in the upstream Feeder 1 on node F1_Node036

as depicted in Figure 4.10. This time the currents of the feeder cut-set sum up to 0.0213+j0.0105. This larger current summation is an indicator of an upstream fault. Thus, the SNPRs observing reverse power (all Feeder 1 SNPRs according to Table 4.8) are allowed to trip.

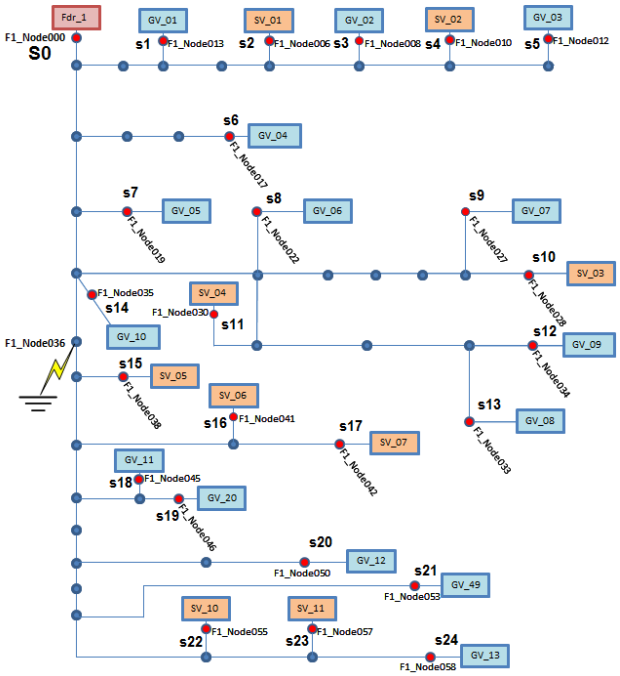

Figure 4.10: Node 562 voltage variations due to cloud

Table 4.8: SNPR operation for the case with 120% PV penetration and minimum load in PV arrangement 2

Without fault [pu]×10^{-2}		With fault [pu]×10^{-2}	
S1: +17.16-j1.28	**S2: +0.70+j0.31**	**S1: +17.22-j1.29**	**S2: +0.7+j0.31**
S3: +5.92-j2.13	**S4: +73.60-j5.25**	**S3: +5.92-j2.14**	**S4: +73.84-j5.27**
S5: +10.30-j1.61	**S6: +18.87-j1.69**	**S5: +10.33-j1.62**	**S6: +18.90-j1.71**
S7: +6.41-j2.44	**S8: +4.90-j2.35**	**S7: +6.41-j2.45**	**S8: +4.89-j2.36**
S9: +3.88-j1.28	**S10: +24.00-j1.00**	**S9: +3.89-j1.28**	**S10: +24.08-j1.00**
S11: +45.77-j3.35	**S12: +5.49-j1.62**	**S11: +45.92-j3.36**	**S12: +5.55-j1.62**
S13: +11.92-j2.33	**S14: +43.12-j2.87**	**S13: +11.91-j2.36**	**S14: +43.25-j2.88**
S15: +31.09-j1.33	**S16: +48.07-j3.54**	**S15: +31.17-j1.34**	**S16: +48.18-j3.56**
S17: +53.78-j3.21	**S18: +11.45-j1.79**	**S17: +53.89-j3.24**	**S18: +11.48-j1.80**
S19: +1.30-j0.61	**S20: +7.00-j1.10**	**S19: +1.30-j0.61**	**S20: +7.00-j1.11**
S21: +38.39-j0.68	**S22: +25.62-j0.62**	**S21: +38.50-j0.68**	**S22: +25.70-j0.62**
S23: +26.48-j0.73	**S24: +8.32-j2.17**	**S23: +26.58-j0.73**	**S24: +8.34-j2.18**
S0: -522.99+j45.73		**S0: -522.78+j45.94**	
Sum: +0.53+j1.05		Sum: +2.13+j1.05	

1.28. Cloud Effect

The intermittent nature of PV power causes injected power variations at downtown network nodes. In this research scattered cloud is considered by randomly assigning power drop at PV generation locations throughout the secondary network at high PV power levels. Satellite data for sun irradiance has been purchased and is being recorded for two sites, one in Baton Rouge, LSU location and the other one in New Orleans, French Quarter. Figure 4.11 presents the exact locations for these sites. Satellite data provides knowledge of solar radiation and effects of wind, cloud or any other natural element on the received solar energy on the earth. The satellite data will be recorded for a complete year starting Dec 1, 2014. However, the satellite data is recorder every minute. Also, the accuracy of the received solar power on earth via the satellite data in unknown. Thus, an experimental setup is prepared and installed at LSU to record the received solar power on the earth with higher time resolution.

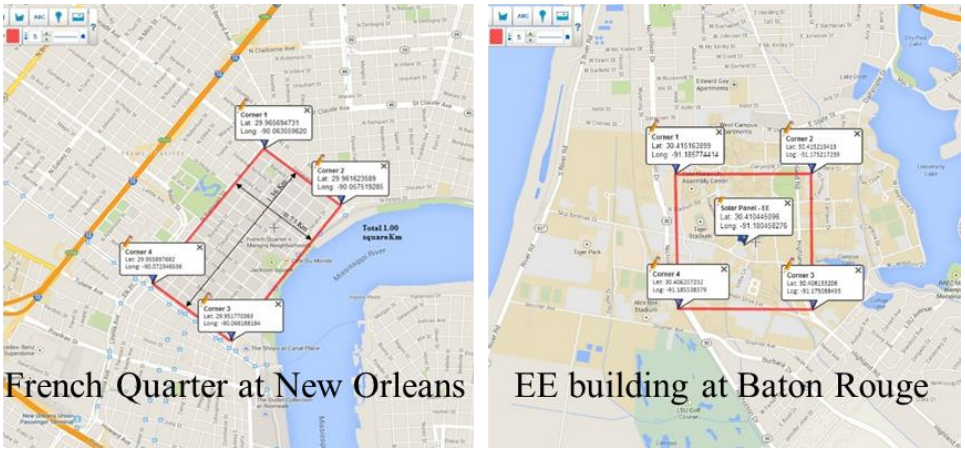

Figure 4.11: The two sites in New Orleans and Baton Rouge for Solar Satellite data acquisition

In order to generate the random power, first solar power is measured over a course of three months in winter 2015 (where solar power variation is significant) at the Louisiana State University. The PV power is measured through a 140-Watt solar panel connected to a resistive

load. The Fluke-43B data acquisition system is used along with LabVIEW software to capture the voltage every four seconds. The solar power measurement setup is shown in Figure 4.2. Next, one of the days in winter with most PV power variation is chosen and maximum power level fall and duration are obtained. Then, cloud assignment is conducted by considering $Tup = -a \times lnU_1$ and $Tdown = -b \times lnU_2$ where U_1 and U_2 are uniformly distributed random numbers in the range [0,1] and a and b are average up and down times in the solar irradiation. The power drop is also generated through uniformly distributed random number in the range of zero to 60% solar irradiance drop. Subsequently, 228 random variable powers are generated using the random distribution functions explained above and are applied to all load nodes in Arrangement 1 at 100% (of full load) penetration level. At this level no reverse power is observed by MNPRs and thus no MNPR trips occur. It is observed that at some nodes, voltage flicker in the range of "irritative" occurs as shown in Figure 4.14 based on IEEE 519 definitions [21]. Also, some nodes experience visible flicker [21]. With SNPR and higher PV power levels voltage flicker increases.

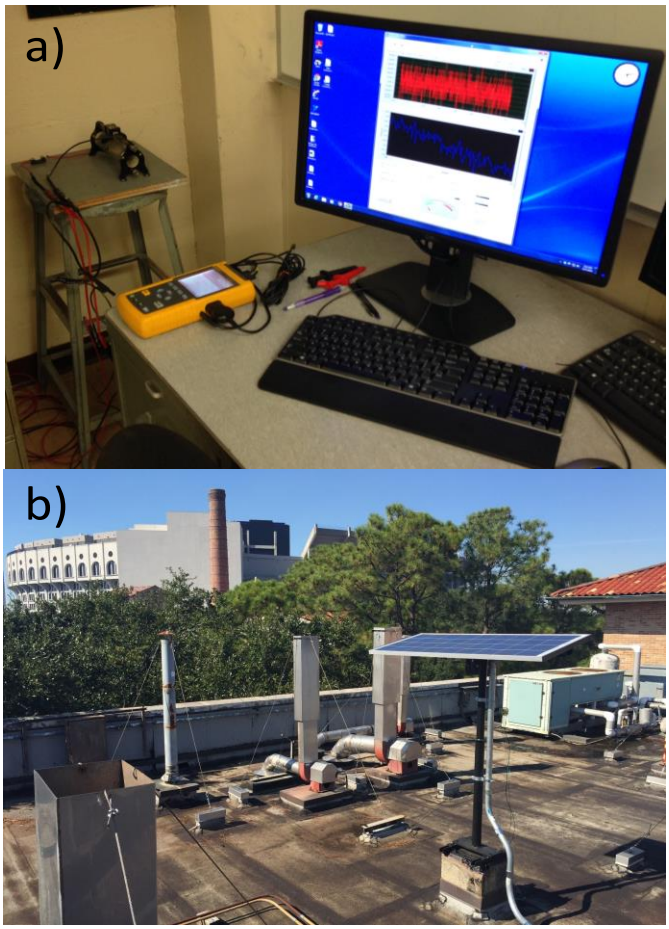

Figure 4.12: Solar power measurement
a) Record setup using Fluke-43B b) Installed solar panel

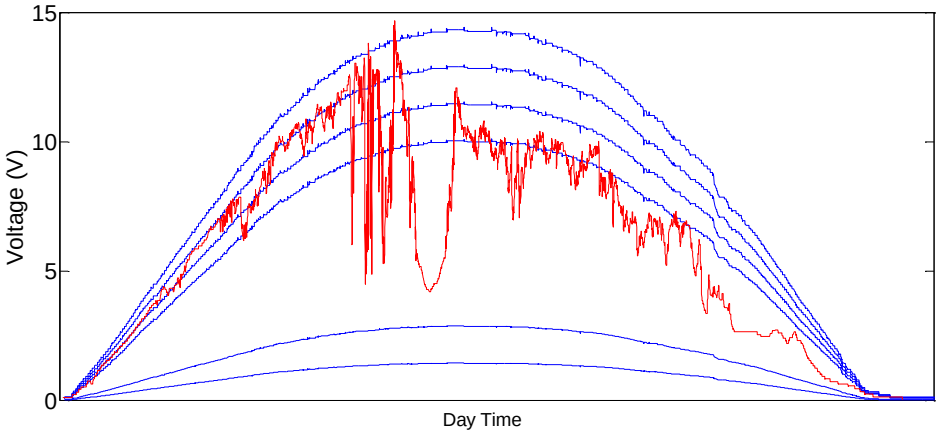

Figure 4.13: A measured cloudy day in red along with typical sunny day with various penetration levels

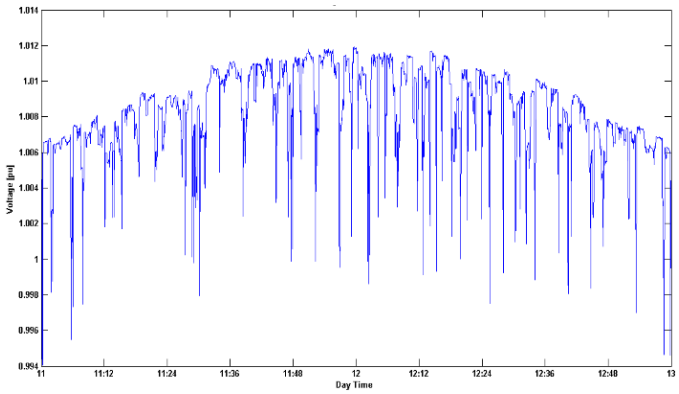

Figure 4.14: Node 562 voltage variations due to cloud

1.29. Voltage Profile

DG has been shown to affect the voltage profile in secondary networks [4], [9], [22]. Voltage analysis of the selected downtown network under full and minimum loading in the presence of different PV generation is discussed in this section for Arrangement 1. Different penetration levels of PV power are considered at loaded nodes that range from 15% to 150% of the nodes' full load. The networks voltage profiles are presented in Figure 4.15 and 4.16. It is shown in the figures that the chances of overvoltage are high in the minimum load condition under high penetration levels. The voltage profiles are obtained by considering SNPRs to allow higher penetration levels. With the MNPR, the voltage profiles are very similar up to the point of voltage collapse where no voltage is established.

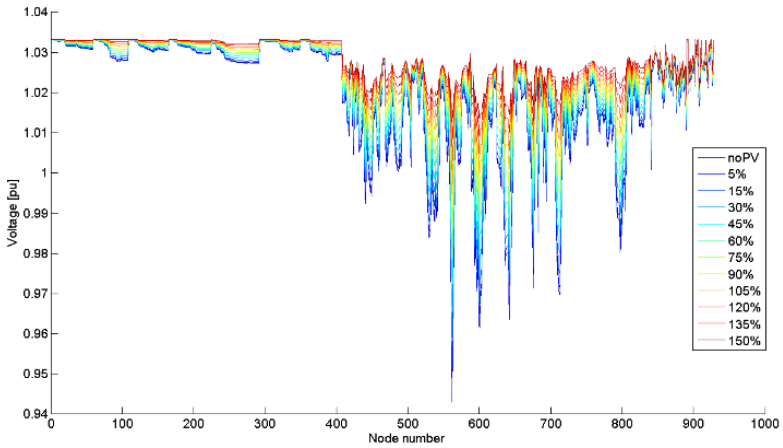

Figure 4.15: Network's voltage profile during full load

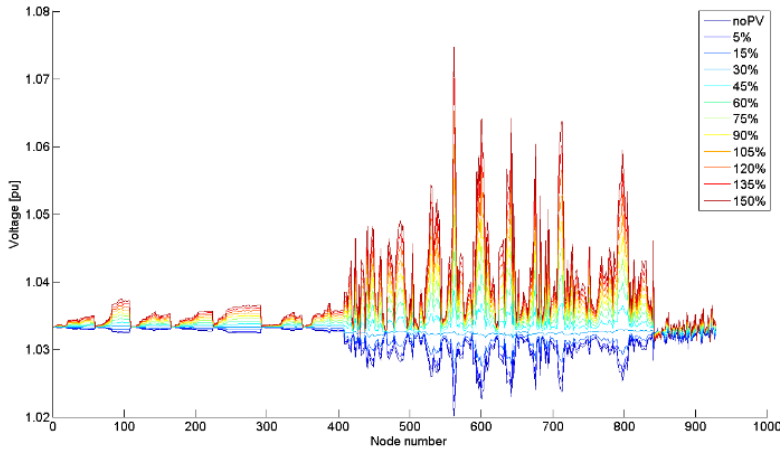

Figure 4.16: Network's voltage profile during minimum load

1.30. A Random PV Allocation Approach Simulation

PV units may have different locations and power capacities. In addition, available PV units are not guaranteed to stay connected to the network at all times. In order to investigate the mentioned problems as well as the impacts of new PV installations to the downtown network a series of scenarios are designed based on random allocation of PV power and existing solar arrays. In these scenarios all the loaded buses have PV units installed on them. PV units' power capacities are randomly chosen from a minimum penetration (existing capacity) to a maximum capacity. The maximum penetration is chosen at 110% of the node's full load. For example, by using 0% as the minimum capacity, it is indicated that no PV unit exists at the bus prior to the study and that new installation can be any value from 0% to 110% of the full load of that bus. It is reminded that in all of these scenarios the total installed PV units' power penetration never exceeds 110% of the total network's power consumption. In summary, this study considers:

- All loaded nodes have PV installed (228 nodes)
- PV penetration is chosen randomly from a minimum to the maximum of the node's full load
- Total installed PV power does not exceed 110% of the network full load

Scenarios are simulated out of 10000 simulations and result are provided. Network stability, network protector trip, and lines overload are investigated and results are provided.

Figure 4.17 depicts a chart presenting the stability of the network. One can see that only 16% of the simulations led to stable cases. Also, in almost 7% of the cases the stability of network is jeopardized.

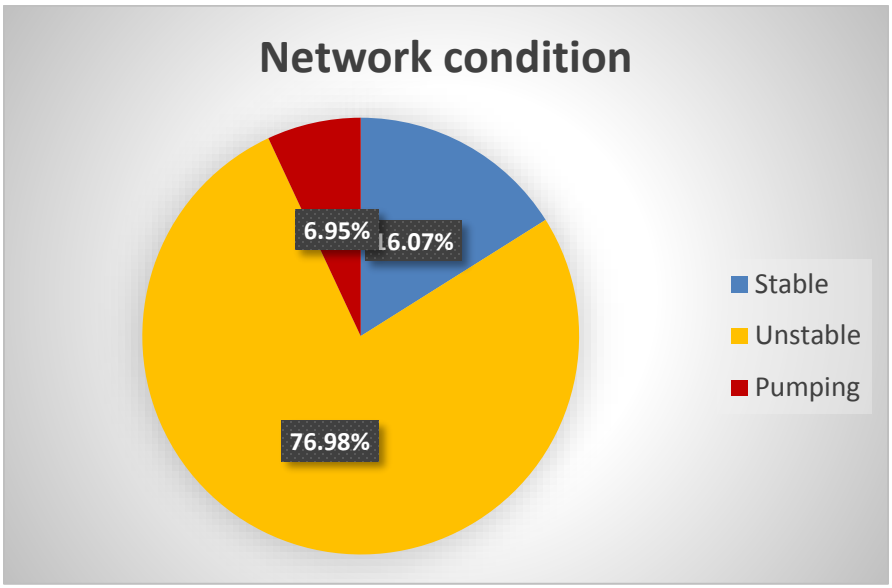

Figure 4.17: Pie chart for network's stability within 10,000 simulations

Figure 4.18 illustrates the probability of the number of network protector trips within the stable cases of all simulations. In most stable cases the number of trips are less than 4. In addition, the likelihood of the network to stay stable is low if there are more than 7 trips.

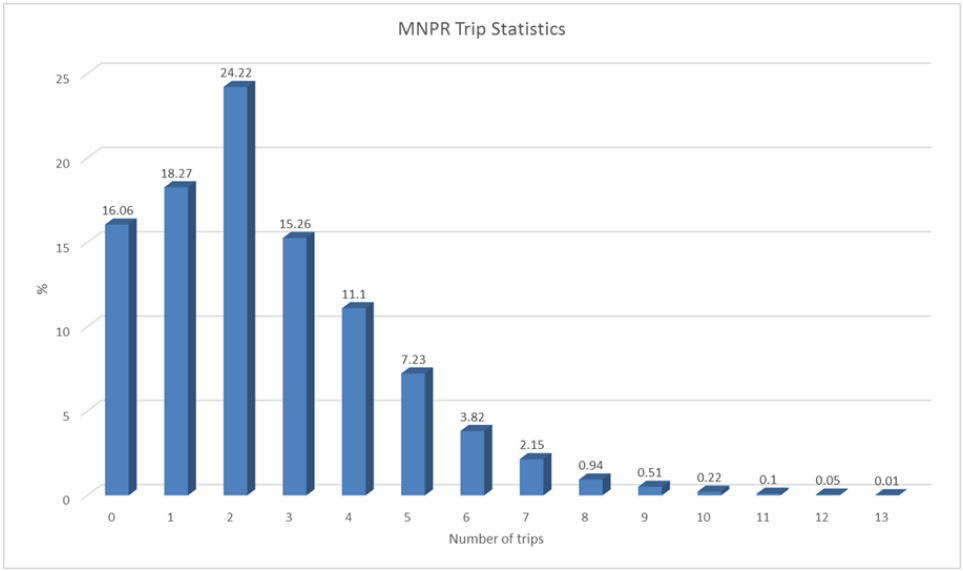

Figure 4.18: Network protectors' number of trips within the stable cases

Figure 4.19 presents the MNPRs that have tripped the most and shows the percentage that a specific network protector has tripped in 10,000 simulations. This result shows that the certain network protectors are more likely to trip than the others. That is, these network protectors are the most vulnerable relays to sense reverse flow and initiate a trip in the case of PV integration.

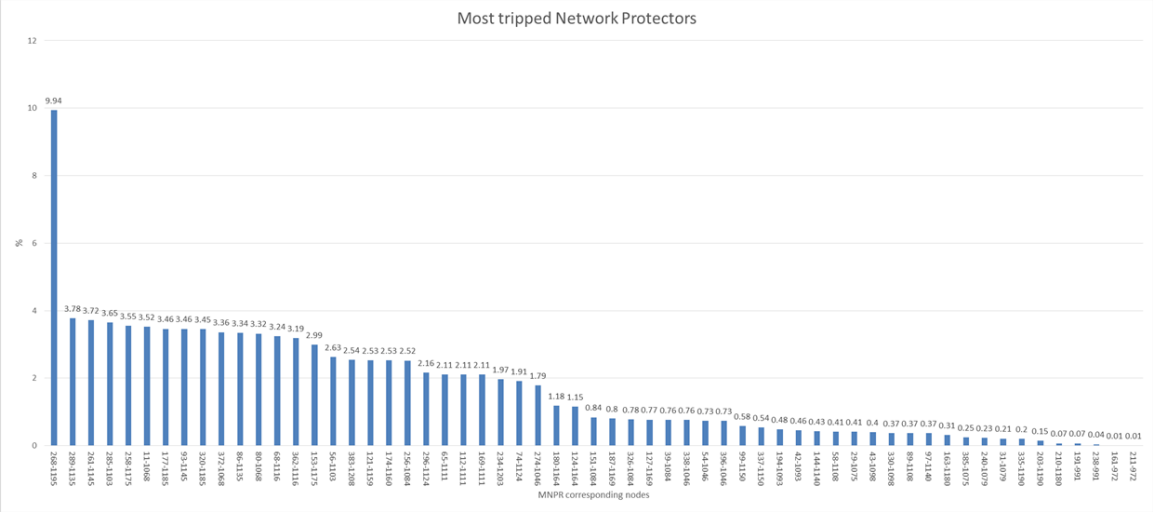

Figure 4.19: Network protectors' trip statistics within 10,000 simulations

Table 4.9 provides all network protector relays that have tripped in this scenario ranked based on their tripping percentages.

Table 4.9: Tripped network protectors ranked based on percentages in 10,000 simulations

Rank	From node	To node	%	Rank	node	node	%
1	268	1195	9.94	31	187	1169	0.8
2	289	1135	3.78	32	326	1084	0.78
3	261	1145	3.72	33	127	1169	0.77
4	285	1103	3.65	34	39	1084	0.76
5	258	1175	3.55	35	338	1046	0.76
6	11	1068	3.52	36	54	1046	0.73
7	177	1185	3.46	37	396	1046	0.73
8	93	1145	3.46	38	99	1150	0.58
9	320	1185	3.45	39	337	1150	0.54
10	372	1068	3.36	40	194	1093	0.48
11	86	1135	3.34	41	42	1093	0.46
12	80	1068	3.32	42	144	1140	0.43
13	68	1116	3.24	43	58	1108	0.41
14	362	1116	3.19	44	29	1075	0.41
15	153	1175	2.99	45	43	1098	0.4
16	56	1103	2.63	46	330	1098	0.37

17	383	1208	2.54	47	89	1108	0.37
18	121	1159	2.53	48	97	1140	0.37
19	174	1160	2.53	49	163	1180	0.31
20	256	1084	2.52	50	385	1075	0.25
21	296	1124	2.16	51	240	1079	0.23
22	65	1111	2.11	52	31	1079	0.21
23	112	1111	2.11	53	335	1190	0.2
24	169	1111	2.11	54	203	1190	0.15
25	234	1203	1.97	55	210	1180	0.07
26	74	1124	1.91	56	191	991	0.07
27	274	1046	1.79	57	238	991	0.04
28	180	1164	1.18	58	161	972	0.01
29	124	1164	1.15	59	211	972	0.01
30	151	1084	0.84				

Figure 4.20: presents the ranges for number of overloaded lines and their percentages of happening in 10,000 simulations. One can see that the possibility of having more than 25 overloaded lines in this scenario is significantly high.

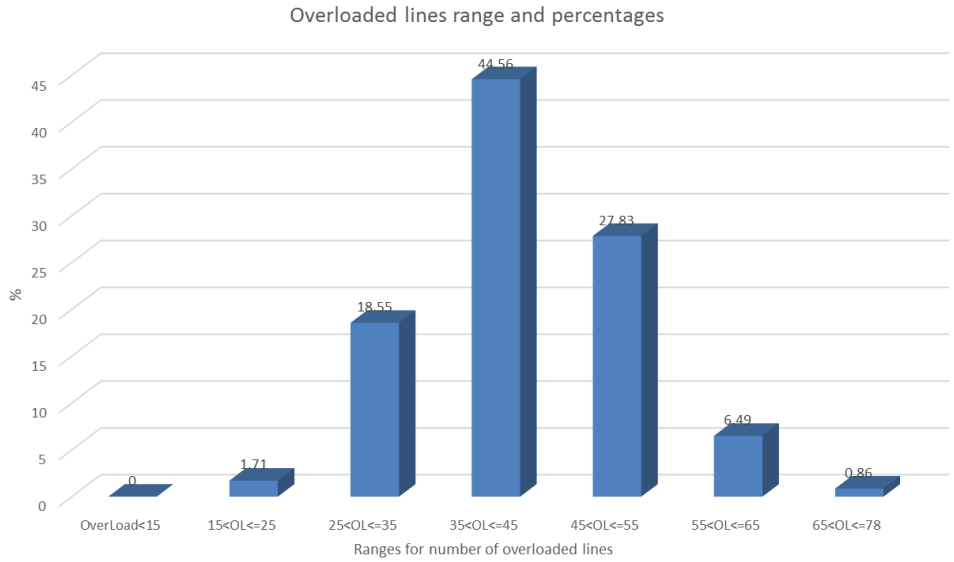

Figure 4.20: Probability of the number of overloaded lines and their percentages in 10,000 simulations

Figure 4.21 depicts the overloaded lines with their line numbers along with their percentages of happening in 10,000 simulations. Using this graph one can detect the most vulnerable lines in the case of solar power integration. For instance, line number 736 experiences overload in more than

85% of simulations. Figure 4.22 illustrates the first 40 lines of this plot in a zoomed graph. Basically, these lines are highly prone to overload in case of similar PV integration.

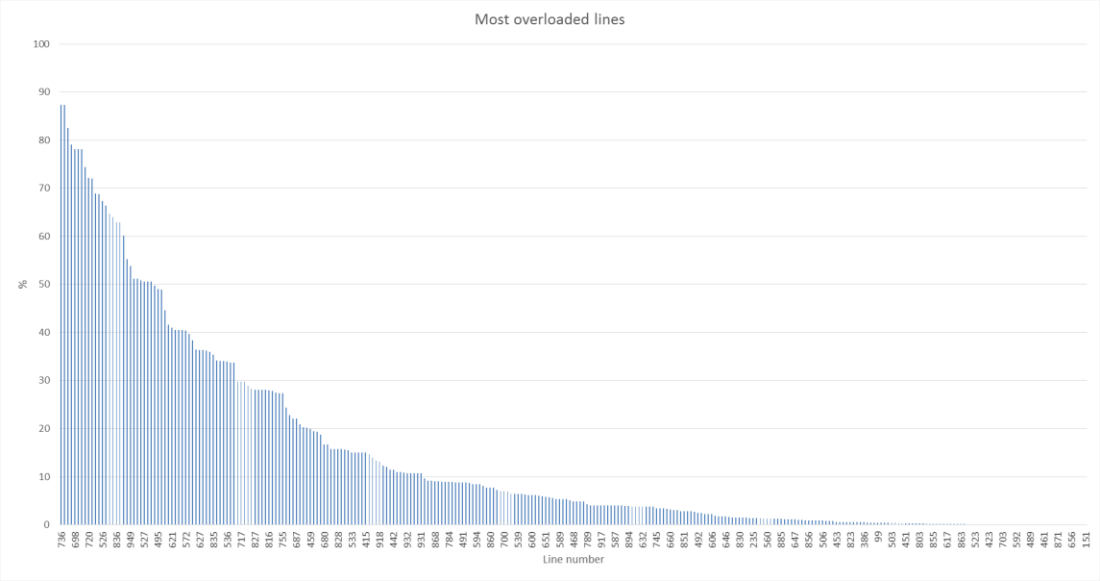

Figure 4.21: Overloaded lines statistics within 10,000 simulations

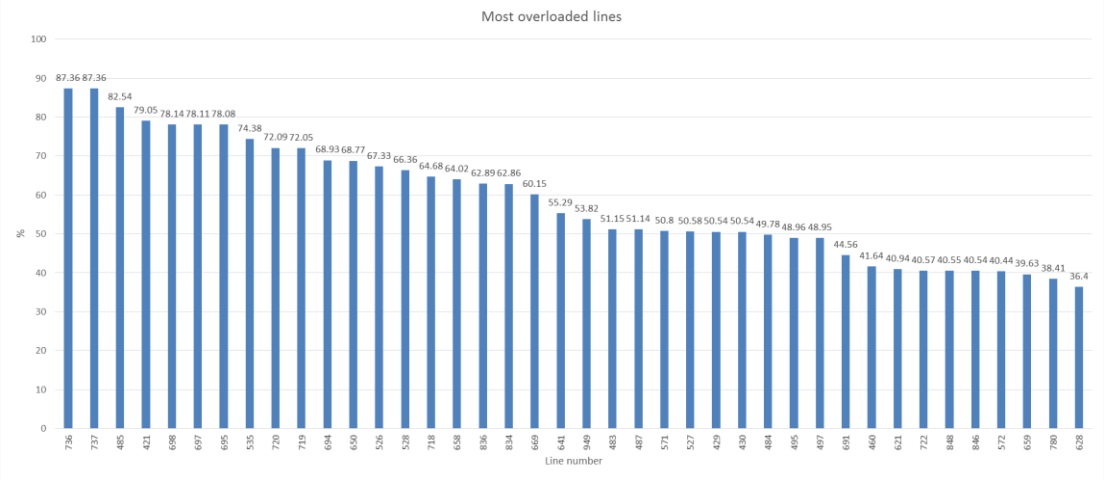

Figure 4.22: First 40 overloaded lines statistics within 10,000 simulations

Table 4.10 presents a ranking of the first 10 overloaded lines based on their percentage of occurrence in the simulations. Overloaded lines active powers, reactive powers, and total powers are provided in pu for more details.

Table 4.10: Overloaded lines ranked based on their percentages out of 10,000 simulations

Ranking	Line number	Active Power P	Reactive Power Q	Total power S	%	Ranking	Line number	Active Power P	Reactive Power Q	Total power S	%
1	736	-0.05568	0.002547	0.055737	87.36	31	691	0.087093	0.00222	0.087121	44.56

2	737	0.055679	-0.00255	0.055737	87.36	32	460	-0.03873	-0.00107	0.010742	41.64
3	485	0.032518	-0.0118	0.034593	82.54	33	621	-0.04983	-0.01728	0.05274	40.94
4	421	0.090851	-0.01719	0.092463	79.05	34	722	-0.01841	0.006567	0.076884	40.57
5	698	0.021834	-0.00247	0.015929	78.14	35	848	0.018427	-0.00653	0.019548	40.55
6	697	0.021847	-0.00244	0.021983	78.11	36	846	0.018414	-0.00655	0.019546	40.54
7	695	0.021865	-0.0024	0.021997	78.08	37	572	-0.04342	-0.00468	0.043672	40.44
8	535	-0.03804	0.01173	0.039812	74.38	38	659	0.030584	-0.0011	0.030604	39.63
9	720	0.044605	-0.0194	0.048643	72.09	39	780	0.049934	0.007222	0.050453	38.41
10	719	0.044563	-0.0195	0.048642	72.05	40	628	-0.01969	-0.00863	0.021492	36.4

1.31. Communication Requirements for Smart Network Protector (SNPR)

Regular network protectors are the key elements assuring downtown networks safety. These devices' primary goal is to protect the transformers. In a case of fault occurs on one of the primary feeders, network protectors isolate that specific feeder from the downtown network to prevent feeding the fault. Power generation in downstream branches result in reverse power flow from downtown network to the upstream feeders. Thus, PV generator can change the power flow direction in a normal operation which mislead network protectors resulting in falsely trips.

Conventional network protectors can't differentiate between PV injected power and an upstream fault. That is, network protectors trip once they sense a reverse flow regardless of its cause. Network protector falsely tripping can jeopardize network stability. Considering a maximum PV penetration can be a solution; however, it prevents the full exploitation of the installed PV capacity. Some the currently available approaches for solving the PV reverse power are summarized in Table 4.11.

Table 4.11: Solutions for PV integration caused reverse flow

Approach	Description	Advantage	Disadvantage
Flat maximum power generation	Defining a maximum power generation for PV units considering network maximum load	Simple No communication No further equipment	Waste of renewable energy Customer complaint
Unit-based maximum power	Defining maximum power for each PV unit based on the customer consumption	Higher PV penetration for customers with high steady consumption	Mostly applies for big customers Limits the PV penetration

		Economical	
Displaceable units	Disconnecting PV units once they exceed exporting power using communication	Adaptable approach Higher PV penetration level Provides monitoring	Requires network-wide communication infrastructure Limits the PV penetration
Smart Network Protector Relays (SNPR)	SNPR differentiates between PV reverse power and upstream fault	Relatively simple to implement Adaptable approach Exploits maximum possible PV penetration Provides monitoring	Requires fast but limited upstream communication

1.31.1. Smart Network Protector Relay (SNPR)

Network protector relays sensitive mode observes current angles with respect to voltage phase angles. This is how the current direction can be identified. The directions of power and current are considered based on the active power direction. Figure 4.23 presents network protector's sensitive mode characteristics along with the active power direction. From Figure 4.23, network protector relays should trip once the current and power fall in to the 2nd and 3rd quarters in the left hand side of the solid line.

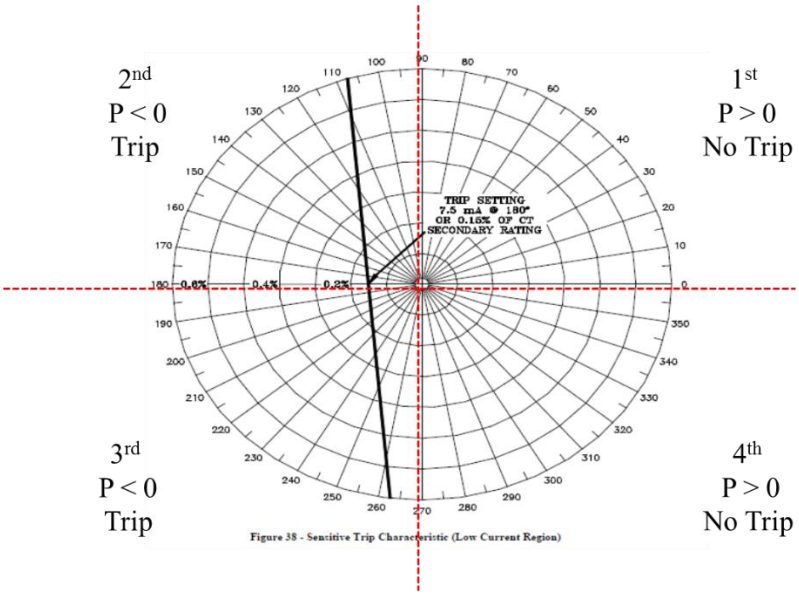

Figure 4.23: Network protector sensitive mode characteristics

The idea pf smart network protector is applicable by upgrading regular network protectors with an overriding logic. This overriding logic prevents false tripping when reverse flow is originated from the PV excessive power generation in the downtown network. This upgrading logic is

presented in Figure 4.24: The proposed method requires obtaining all currents, injected and absorbed, by the network protectors and loads on the feeder. This requires a data acquisition system using hard-wire connections or a data transmission infrastructure. Processing the measured currents can provide the signal that overrides the trip command of all the network protectors inside the feeder. The proposed method must be applied to all the individual feeders, and individual phases, separately.

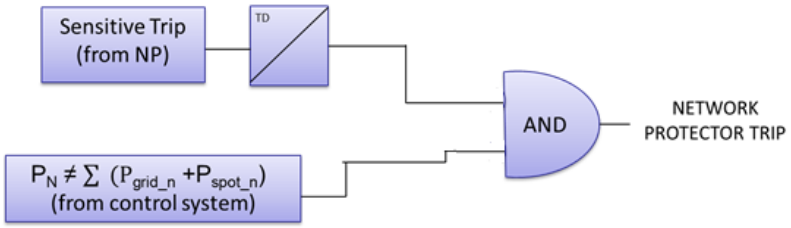

Figure 4.24: Upgrading logic of smart network protector

1.31.2. Communication

Communication is a key element in the operation of the proposed smart network protector relay. In order to reach a decision all of the measured currents in the protected zone must be collected by the zone's control center, the summation calculated, and the result sent to the individual network protectors in the zone. Hardwire, LAN, Ethernet, SCADA, wireless communication or any other means of communication can be used to perform this process. The current summation can also be performed by physically connecting the network protector CT in parallel and sending the resultant measured value to the relevant control center. Figures 4.25 and 4.26 show smart network protectors communicating with their control center. Data will be sent if reverse flow is detected in any of the relays. Then relays wait for a limited time to see if trip overriding command is received from the control center. The entire process must be performed within six cycles which is the time the network protector waits to issue a trip command. The protected zone is a single phase circuit and

can be part of a feeder. Thus, unbalanced circuits and multi feeder topology do not cause any barriers in the upstream feeder fault detection.

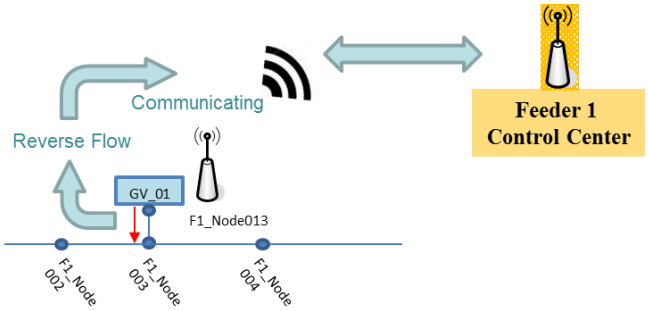

Figure 4.25: Smart network protector sensitive tripping criteria

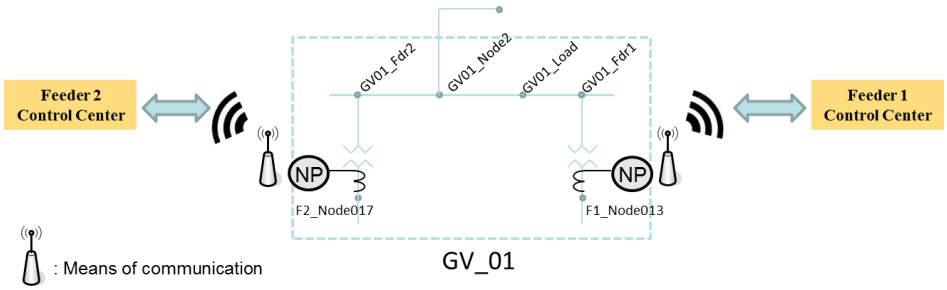

Figure 4.26: Smart NP communicating with its own upstream feeder control center

1.31.3.Industrial Communication Protocols

One of the advantages of the proposed solution is its flexibility and adaptability to different designs. That is, various prototypes can be implemented with different covering zones and specifications as well as choices on the communication infrastructure. Figures 4.27 to 4.28 present possible prototypes for smart network protectors. Zones and means of communications are shown in these prototypes.

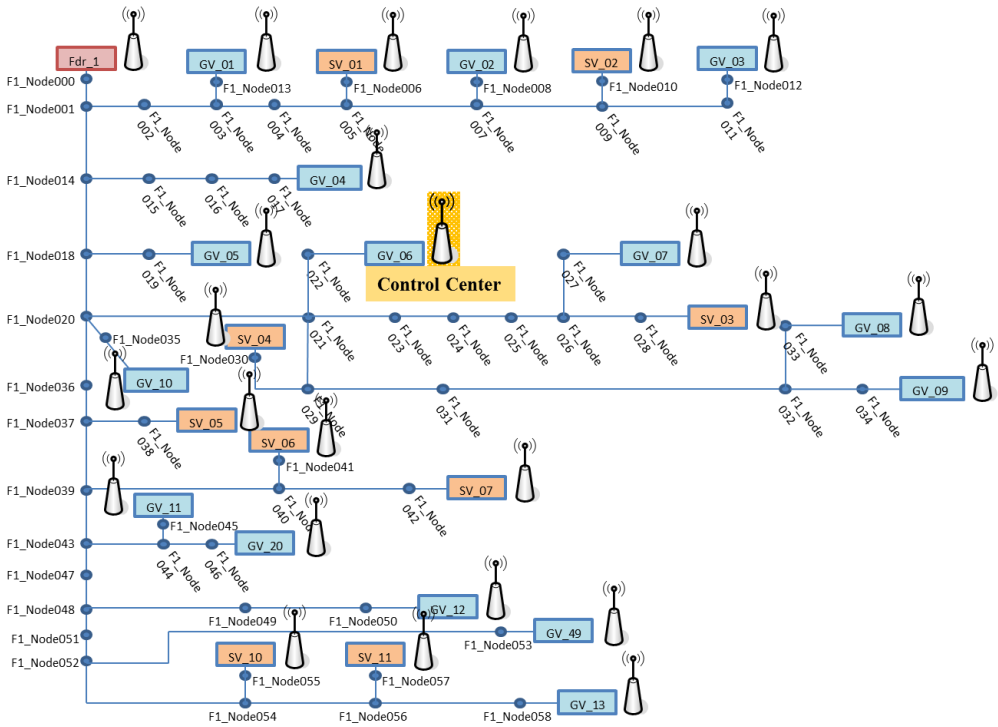

Figure 4.27: Prototype 1 The protected upstream zone includes the entire feeder

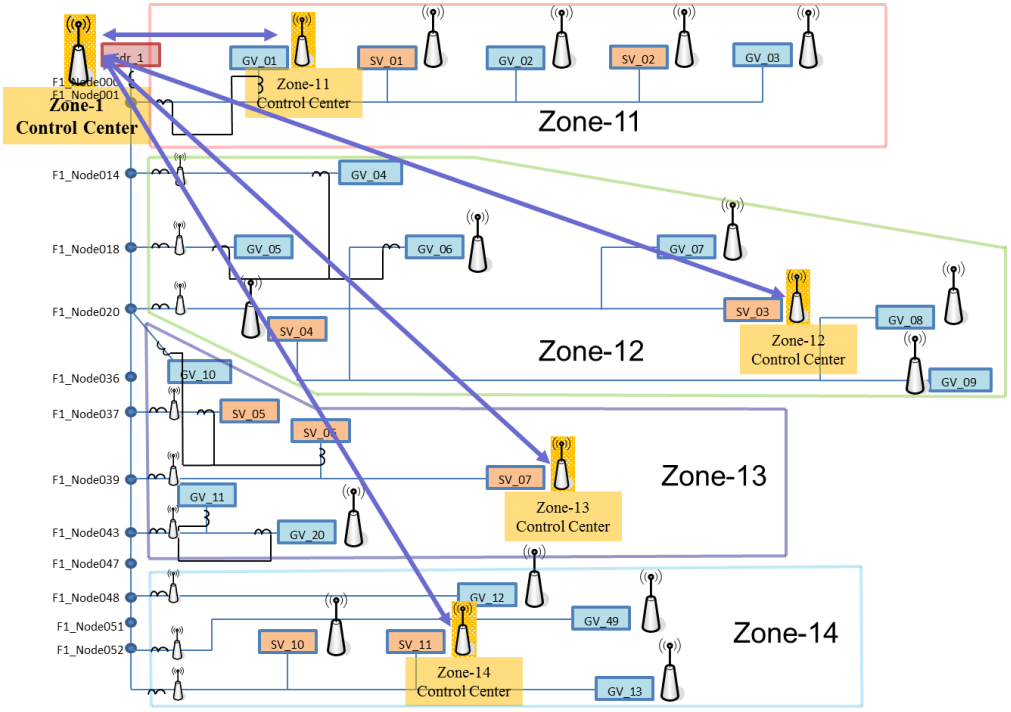

Figure 4.28: Prototype 2 The upstream feeder is split into smaller zones

Different industrial communication protocols can be chosen. Each protocol can be implemented through various means of communication such as hard wire, coaxial cables, twisted pairs, LAN,

Ethernet, and wireless communication. For instance, for vaults locating close to one another hard wire communication may be preferred. A list of popular and applicable communication protocols includes Industrial Ethernet, DNP3, Modbus, CanOpen, DeviceNet, Profibus, Fieldbus, etc. Also, some proprietary protocols can also be chosen, including SPA (ABB), VDEW (Siemens), and K-BUS (Alstom).

Table 4.12 provides a list of most common and applicable industrial protocols. An estimation of speed is provided for each of these protocols along with possible means of communication.

Table 4.12: Industrial communication protocols and estimated design specification

Protocol	Implementation	Bit rate	Max Distance	Max
Industrial Ethernet	Coax, twisted pair, fiber	10, 100 Mbps	100 m up to Km	1024
Modbus RTU/ASCII	Twisted pair	300 bps-38.4Kbps	350 m (for RS-485)	250
DNP3	Twisted pair, fiber, wireless, Ethernet	300-1200 bps	Long	Multiple
CANopen	Twisted pair	10K-1Mbps	25-1000 m	127
DeviceNet	Twisted pair	125-500Kbps	500m-6Km	64
PROFIBUS	Twisted pair, fiber	9.6K-12Mbps	100m	127
Fieldbus	Twisted pair, fiber	31.25K-5Mbps	500-1700m	127

Ethernet is the most updated and promising capabilities as required for SNPR implementation. Some of the advantages of Ethernet include:

- Abundant hardware availability (vast number of suppliers)
- Security and Reliability by IP addressing
- Scalability and flexibility (easy to expand)
- Easy design and programming with user interface enabled
- Can transfer power by PoE technology as well as any form of data
- Record and monitoring features.

Ethernet design is simple as long as nodes are located within 1000 meter from one another. This will mandate zoning in any design and prototype chosen for SNPR implementation. The

communication delay can be reduced by choosing fast microprocessor units. Processing will not be a preventive factor due to the simple math and algorithm involved. Current measurement and handshaking signals of a large number of nodes can be accommodated in the Ethernet through 1500 Bytes. These data are required to be transmitted from all nodes in a selected zone through Ethernet. Considering an Ethernet with 10 Mbps bit rate, one can calculate the communication delay time as: (1500×8)/10,000,000 = 0.0012 sec or 1.2 msec.

One can see that by using 10Mbps, the SNPR can scan the measured data several times within the six cycle time span. Using the same procedure, the final delay time can be calculated for Ethernet with 50 and 100 Mbps as:

- Ethernet 50 Mbps speed: 0.48 ms
- Ethernet 100 Mbps speed: 0.24 ms

Hence, using a higher Ethernet speed results in higher speed. This can avoid possible false decisions due to transients which are common in downtown networks.

1.32. Conclusion

Operational challenges of network protectors in downtown networks in the presence of PV power integration are discussed in this chapter. A model is developed for the downtown network based on line impedance models, and load flow is performed to simulate the network operation. Distributed PV unit arrangements are utilized and the results are compared. It is demonstrated that large network protector trips can occur in the presence of PV power leading to potential network voltage collapse. Smart network protectors that distinguish between upstream faults and PV excess power are proposed, and network operation is compared with and without the smart network protectors. Finally, voltage profile and flicker are shown to be affected by the PV power installed in the downtown network.

1.33. References

[1] Katiraei, F.; Agüero, J.R., "Solar PV Integration Challenges," *Power and Energy Magazine, IEEE* , vol.9, no.3, pp.62,71, May-June 2011.

[2] Walling, R.A. ; Saint, R.; Dugan, R.C.; Burke, J.; Kojovic, L.A., "Summary of Distributed Resources Impact on Power Delivery Systems," *Power Delivery, IEEE Transactions on* , vol.23, no.3, pp.1636,1644, July 2008.

[3] U.S. Solar Market Insight Report, Q1 2015, executive summary. [Online] Available: http://www.seia.org/research-resources/solar-market-insight-report-2015-q1

[4] Po-Chen Chen; Salcedo, R.; Qingcheng Zhu; de Leon, F.; Czarkowski, D.; Zhong-Ping Jiang; Spitsa, V.; Zabar, Z.; Uosef, R.E., "Analysis of Voltage Profile Problems Due to the Penetration of Distributed Generation in Low-Voltage Secondary Distribution Networks," *Power Delivery, IEEE Transactions on* , vol.27, no.4, pp.2020,2028, Oct. 2012.

[5] Ochoa, L.F.; Harrison, G.P., "Minimizing Energy Losses: Optimal Accommodation and Smart Operation of Renewable Distributed Generation," *Power Systems, IEEE Transactions on* , vol.26, no.1, pp.198,205, Feb. 2011.

[6] Brown, T., "Transmission network loading in Europe with high shares of renewables," *Renewable Power Generation, IET* , vol.9, no.1, pp.57,65, 1 2015.

[7] Tonkoski, R.; Lopes, L.A.C.; El-Fouly, T.H.M., "Coordinated Active Power Curtailment of Grid Connected PV Inverters for Overvoltage Prevention," *Sustainable Energy, IEEE Transactions on* , vol.2, no.2, pp.139,147, April 2011.

[8] Hooshyar, H.; Baran, M.E., "Fault Analysis on Distribution Feeders With High Penetration of PV Systems," *Power Systems, IEEE Transactions on* , vol.28, no.3, pp.2890,2896, Aug. 2013.

[9] Baran, M.E.; Hooshyar, H.; Zhan Shen; Huang, A., "Accommodating High PV Penetration on Distribution Feeders," *Smart Grid, IEEE Transactions on* , vol.3, no.2, pp.1039,1046, June 2012.

[10] Cheung, H.; Hamlyn, A.; Lin Wang; Cungang Yang; Cheung, R., "Investigations of impacts of distributed generations on feeder protections," *Power & Energy Society General Meeting, 2009. PES '09. IEEE* , vol., no., pp.1,7, 26-30 July 2009.

[11] Yazdanpanahi, H.; Yun Wei Li; Wilsun Xu, "A New Control Strategy to Mitigate the Impact of Inverter-Based DGs on Protection System," *Smart Grid, IEEE Transactions on* , vol.3, no.3, pp.1427,1436, Sept. 2012.

[12] Alam, M.J.E.; Muttaqi, K.M.; Sutanto, D., "Mitigation of Rooftop Solar PV Impacts and Evening Peak Support by Managing Available Capacity of Distributed Energy Storage Systems," *Power Systems, IEEE Transactions on* , vol.28, no.4, pp.3874,3884, Nov. 2013.

[13] Alam, M.J.E.; Muttaqi, K.M.; Sutanto, D., "An Approach for Online Assessment of Rooftop Solar PV Impacts on Low-Voltage Distribution Networks," *Sustainable Energy, IEEE Transactions on* , vol.5, no.2, pp.663,672, April 2014.

[14] Zamani, M.A.; Yazdani, A.; Sidhu, T.S., "A Communication-Assisted Protection Strategy for Inverter-Based Medium-Voltage Microgrids," *Smart Grid, IEEE Transactions on* , vol.3, no.4, pp.2088,2099, Dec. 2012.

[15] Schweitzer, E.O.; Finney, D.; Mynam, M.V., "Applying radio communication in distribution generation teleprotection schemes," *Protective Relay Engineers, 2012 65th Annual Conference for* , vol., no., pp.310,320, 2-5 April 2012.

[16] Li Yu; Czarkowski, D.; De Leon, F.; Bury, W., "A time sequence load-flow method for steady-state analysis in heavily meshed distribution network with DG," *Compatibility and Power Electronics (CPE), 2013 8th International Conference on* , vol., no., pp.25,30, 5-7 June 2013.

[17] Wei-Jen Lee; Cultrera, J.; Maffetone, T., "Application and testing of a microcomputer-based network protector," *Industry Applications, IEEE Transactions on* , vol.36, no.2, pp.691,696, Mar/Apr 2000.

[18] IEEE Application Guide for IEEE Std 1547(TM), IEEE Standard for Interconnecting Distributed Resources with Electric Power Systems," *IEEE Std 1547.2-2008* , vol., no., pp.1,217, April 15 2009.

[19] IEEE Recommended Practice for Protection and Coordination of Industrial and Commercial Power Systems (IEEE Buff Book)," *IEEE Std 242-2001 (Revision of IEEE Std 242-1986) [IEEE Buff Book]* , vol., no., pp.1,710, Dec. 17 2001.

[20] IEEE Standard Requirements for Secondary Network Protectors," *IEEE Std C57.12.44-2014 (Revision of IEEE Std C57.12.44-2005)* , vol., no., pp.1,65, June 13 2014.

[21] IEEE Recommended Practices and Requirements for Harmonic Control in Electrical Power Systems," *IEEE Std 519-1992* , vol., no., pp.1-112, April 9 1993.

[22] Salcedo, R.; Xuanchang Ran; De Leon, F.; Czarkowski, D.; Spitsa, V., "Long Duration Overvoltages due to Current Backfeeding in Secondary Networks," *Power Delivery, IEEE Transactions on* , vol.28, no.4, pp.2500,2508, Oct. 2013.

[23] NREL Technical Report, "Interconnecting PV on New York City's Secondary Network Distribution System", NREL/TP-7A2-46902, November 2009. Available:

[24] www.energy.gov/eere/sunshot/downloads/interconnecting-pv-nycs-secondary-network-distribution-system

[25] ETI MNPR FieldPro Manual.

[26] Available: http://www.eti-nj.com/support.html

[27] EPRI report, "Modeling High-Penetration PV for Distribution Interconnection Studies"

[28] http://www.renewableenergyworld.com/rea/news/article/2014/02/the-interconnection-nightmare-in-hawaii-and-why-it-matters-to-the-u-s-residential-pv-industry?cmpid=SolarNL-Thursday-February13-2014

Conclusive Remarks and Future Works

1.34. Conclusion

The issue of DERs integration and its various consequences are explained in each chapter based on the network under study. The first chapter tackles the problem from a large power system perspective. Phasor Measurement Units (PMUs) are used in this chapter to achieve a robust fault location algorithm. However, there are two fundamental concern in utilizing PMUs for power system fault location. That is where to install PMU devices and how to achieve system fault observability. It is shown in chapter 2 that by considering the proposed idea of multi estimation and preventing it when allocating PMUs on system buses, the proposed method can achieve system fault observability. This also can be deduced from the Artificial Neural Network (ANN) high rate of fault detection within the defined accuracy. On the other hand, power system sensitivity indices are developed to qualify the bus locations capability to observe system fault states. Using these sensitivity indices, system buses are evaluated to reach the best set of locations achieving system fault observability. A search algorithm is proposed and developed to check the system buses with their corresponding sensitivity indices and find the optimized PMU locations. Later, a specific ANN is developed to test the proposed methodology with test systems where numerous faults are applied within the expected target precisions. The developed ANN creates a unique function mapping between a PMU set measurements and all possible faults in the system. It is worth mentioning that available current and voltage transformers measurements accuracy is also incorporated in the methodology (sensitivity criteria) for the first time.

The customers in distribution networks have shown high interest in DERs integration. This results in significant number of DERs integration in such area which is also reported by various

utility companies. An overhead distribution network is considered in Chapter 3 to investigate various effects of DERs integration. It is shown in this chapter that integrating DGs in such networks can easily accompany with various issues. PV units are used as the extreme case for output intermittency in various time scales. Cloud effects can have significant impacts on PV integrated network area from both customer and utility perspectives. Results are provided for cloud effects causing irritative and noticeable voltage flickers based on applicable standards. Harmonics can easily be an issue with such DERs integration while can be avoided by employing filters as a short term solution. From a long term perspective, various standards are defining different criteria for inverter and power electronic vendors to limit their harmonic outputs. Reactive power compensation is also a feasible solution for both harmonic issue as well as lack of reactive power in downstream. Results show significant improvement in network operation by employing multiple steps capacitor banks while adverse effects with a design application without prior study.

Smart inverter and battery storage applications and are also briefly discussed. It is mentioned that smart inverter functions can significantly change the effects of DERs integration as well as raise the networks hosting capacity. Various power system software and applications such as Energy Management Systems (EMS) and Distribution Management Systems (DMS) employ such functionality by communication infrastructure. Three of the most effective functions are explained. Volt-VAR has showed the most impact on various aspects of DERs integration which can be considered as an advanced reactive compensation. Fixed power factor and Volt-Watt are other functions which have showed the most effectiveness. Provided discussions showed that there are multiple details need to be considered in smart inverter functionality and battery storage applications. Some highlighted points are mentioned along with lessons taken form field applications.

Meshed network structure effect by DERs integration is discussed in chapter 4. It is shown that PV integration in downtown networks can easily cause network collapse and significant outage due to network protector malfunction. Network protectors cannot distinguish between and upstream fault and a PV (or any other DER type) originated reverse power export. There are various scenarios for this phenomenon causing different level of issues such as: overload, reverse flow, relays pumping, and network collapse. An efficient and economical algorithm and upgrade is developed and proposed for traditional network protectors. The new Smart Network Protectors Relays (SNPR) solves the MNPR false trips and significantly increase network hosting capacity. This also improves the network operation and prevents collapse due to MNPR trips. It is shown that lines and transformer ratings issues can still exist since these are rated based on the original network structure. While the SNPR releases the maximum possible PV penetration in terms of reverse flow issues and MNPR trips. Since SNPR uses communication infrastructure, various communication methods are discussed showing different possible schemes to apply SNPR for meshed network protection. It's shown that it is feasible to have a SNPR tripping time equal to the traditional MNPR when using a proper communication method.

1.35. Future Works

The following recommendations are made for possible future research:

- Optimization algorithm to be used for the proposed sensitivity indices methodology
- Consideration of price, contingency, and cyber security for the proposed OPP algorithm
- Detailed investigation for communication infrastructure required for SNPR application
- Evaluation of smart inverter functions possible mutual effects
- Smart inverter capabilities to achieve fully operating smart grid with adaptive protection

Appendix

IEEE test cases used in this dissertation.

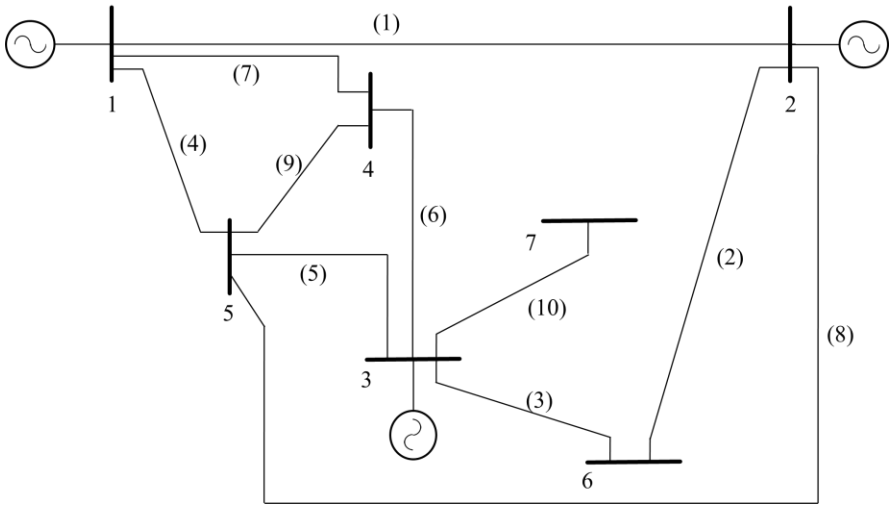

IEEE 7-bus benchmark

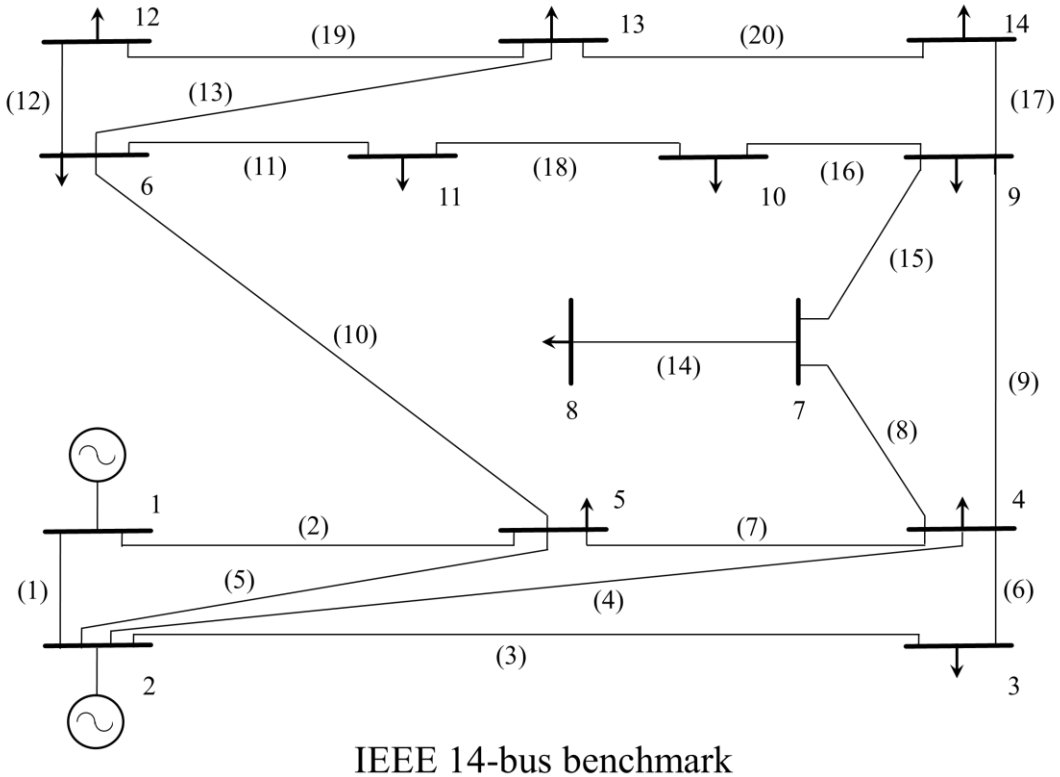

IEEE 14-bus benchmark

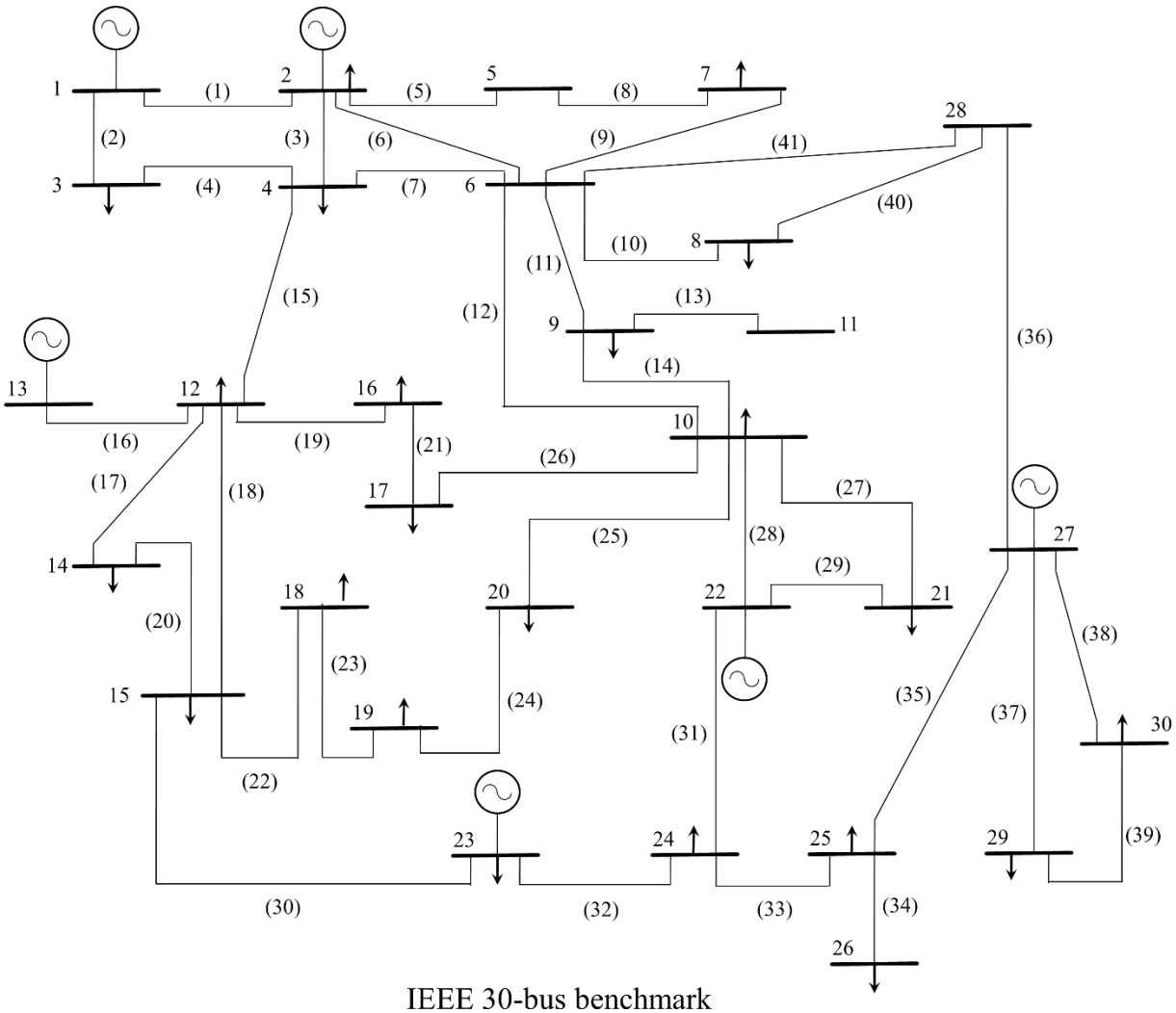

IEEE 30-bus benchmark

Vita

Pooria Mohammadi received his B.S. degree in electrical engineering from Iran University of Science and Technology (IUST), Tehran, Iran, in 2010 and his M.S. degree focused in power system and protection from University of Texas at Tyler, Texas, in 2013.

Currently, he is a Ph.D. candidate at the ECE department, Louisiana State University (LSU). His current research includes power system protection, Optimal PMU Placement (OPP), observability and state estimation, and Distributed Generations (DGs) integration. He has conducted several projects for utility companies during his education and holds three patents. His research interests also include smart grid, renewable energies, PMU applications, intelligent and adaptive methods in power systems, and storage devices.